Mechanisms of Direct and Indirect (Photo)Electrochemical Alcohol Oxidation Reactions

by

Bradley D. Terry

A dissertation submitted in partial fulfillment
of the requirements for the degree of
Doctor of Philosophy
(Chemistry)
in the University of Michigan
2022

Doctoral Committee:

Professor Bart M. Bartlett
Assistant Professor Andrej Lenert
Professor Stephen Maldonado
Professor Corey R. J. Stephenson

Bradley D. Terry

bdterry@umich.edu

ORCID iD: 0000-0002-6771-7482

"The ultimate, hidden truth of the world is that it is something that we make, and could just as easily make differently." –David Graeber

Acknowledgements

Kathryn, you are my inspiration. Growing alongside you over the past five years has been delightful. You always challenge me in constructive ways and offer unique perspectives that help me reconcile the person I am with the person I want to be. I can't believe I deserve such a selfless and caring partner like you; thank you for working tirelessly to convince me that I do. To my family, I owe you more than I could ever express in a paragraph or two. Mom, you gave me every opportunity to achieve my goals and encouraged me to make sure I did what *I* wanted. Knowing I always had your unwavering love and support gave me the confidence to persevere in moments of doubt. Thank you for making my friends feel as if they're part of the family, we all love you. Dad, you are the most intelligent person I have ever met. Seeing you (successfully) troubleshoot any problem always leaves me in awe. You taught me so much about personal responsibility and relayed the importance of hard work; so much of who I am today comes from your perspectives, and I am extremely grateful. Ash, you are a phenomenal sister. I am so lucky to have you to support me and defend me at all moments. Your openness is admirable, thank you so much for always being there.

Bart, I owe you a monumental debt of gratitude. I'll never forget emailing you—before applying to UM—and receiving a thoughtful and encouraging response; inquires sent to just about all other faculty were lost in the ether. Your reply meant the world to me and gave me confidence when applying to graduate programs. Thank you for offering me a spot in your lab and keeping the social element vivacious. I am a much better scientist from your rigorous but fair mentorship, and I really appreciate all the interactions we've had over the years. I'll sincerely miss the conversations at B-dubs. To my thesis committee—Stephen Maldonado, Corey Stephenson, and Andrej Lenert—thank you for monitoring my progress throughout the years and providing challenging outside perspectives. Your feedback helped eliminate project myopia and ensured the vision/targets remained interesting to the larger scientific community. To my undergraduate advisor, Dr. Greg Felton, I really attribute much of my success to your guidance. Until I joined

your lab, I never knew my moral outlook could be matched so harmoniously with my work environment. Thank you for spending so much time on my professional development.

John DiMeglio, thank you so much for working with me over the years. I always felt like I had a second advisor in you. Your open-mindedness and passion for science is extraordinary. You are truly one of the best people I've ever met; thank you for grooming me into a person I'm proud to be. The Bartlett group has changed so much over the years, but Bart ensured a supportive and friendly environment remained. This feature may have been the most important to me during my Ph.D. Aaron, as my visitation weekend host, you were the first person to introduce me to the UM community and Bartlett group. Over the years, you always talked me up and made me feel like such a useful member to the group, especially early on when I felt like I was struggling. Thank you for always being there to talk to. Adam, I always appreciate how tough you were on me. Sometimes our interactions were maddening, but I am so much more capable as a scientist because of them. Andy, we have such an interesting past with living together while working together. You're such an intelligent guy, your widespread talents never cease to amaze me. Kori, I had a ton of fun working with you over the years. Your ability to keep a cool head in tough times is impressive. I really appreciate you being there to chat and always being understanding/supportive.

Christian, you were always good at establishing a good work-life balance and always encouraged the group to enjoy each other outside of the lab; I'm grateful for your unifying presence. Li, having you after John D's departure was crucial for my success in the lab. Just like John, you're supremely intelligent yet open to discussing all things science. I really enjoyed working with you; you have such a bright future. To my undergraduate (and now master's student) John Cousineau, thank you for always trusting me. I was so lucky to have such a hardworking and creative individual to work with for the past few years. I'm excited to see where you end up.

To my buddies—Lucas, Nikolov, Valencia, Reed, Poz, Jack, and Kyle—I am so fortunate to have such an eclectic group of intelligent and crazy buds who all get along so well. Most of my happiest moments are with you guys. The confidence and agency you all have constantly encourages me to challenge my fears and press on to meet my goals. I sincerely hope we end up in Mega House or Mega Cul-De-Sac one day. Cheers! Finally, Devon, we've become such good friends in short order. Rethinking conventions and challenging scientific or policy paradigms with

you is always a great time. Your thoughtful approach in problem solving has always impressed me.

Table of Contents

List of Tables

List of Figures

List of Appendices

Abstract

Selective alcohol oxidation to carbonyl compounds is a crucial oxidative transformation in academic and industrial settings. When derived from renewable (inedible) biomass resources, this commodity-forming platform has the potential to offset—or eliminate completely—current petrochemical oxidation routes in polymer production and fine chemical synthesis. During (photo)electrochemical alcohol oxidation, protons are eliminated from the alcohol substrate that can be used for cathodic H_2 generation at a cathode, representing an additional petroleum offset for chemical fuel production. Renewable solar energy can be used directly through photo(electro)chemical (PC/PEC) or indirectly with electrochemical (EC) control to drive these high value commodity- and fuel-forming redox reactions. In this thesis, catalytic and cocatalytic selective alcohol oxidation platforms are explored in acetonitrile and aqueous brine solutions.

Motivated by the discovery that nitrate anions can mediate photochemical alcohol oxidation in acetonitrile, bismuth vanadate ($BiVO_4$) photoelectrodes were used in place of cadmium sulfide (CdS) powder to test the codependency of nitrate on the light-absorbing surface for indirect alcohol oxidation. Moving from photochemical control to photoelectrochemical control separates the light-driven redox half reactions onto two separate (photo)electrode materials, allowing for a more detailed investigation on nitrate's exclusive role(s) in this mediated process. Under photoelectrochemical control, nitrate improved the rate of benzaldehyde on $BiVO_4$ in the presence of blue LED light (100 mW cm^{-2}, λ_{max} = 448 nm) but surprisingly nitrate was consumed in the process, serving as stoichiometric oxidant rather than a solution phase cocatalyst.

Platinum electrodes were used to further explore the technique-dependent behavior of nitrate in acetonitrile toward indirect alcohol oxidation. Electrochemical nitrate oxidation led to faster rates of benzyl alcohol oxidation yet displayed a similar nitrate consumption to the PEC work on $BiVO_4$ photoelectrodes. Rotating ring disk experiments confirm a latent role of collocal O_2 reduction, where reduced oxygen species (ROS) generated near nitrate anion oxidation (during PC alcohol oxidation on CdS) can serve as an *in-situ* generated base; ROS deprotonate HNO_3 after nitrate radical reacts with the alcohol substrate, leading to a catalytic behavior of nitrate not

observed under (photo)electrochemical conditions. Unfortunately, alcohol oxidation in acetonitrile always occurred with undesired oxygen reduction at the cathode.

To encourage proton reduction to form H_2 product during alcohol oxidation, aqueous systems were used to explore alcohol oxidation on manganese oxide electrocatalysts. Here, we discovered a dependence on the presence of O 1s (531 eV) feature, attributed to oxygen vacancies, for observed current increase as a response to 5-HMF introduction in brine. Films with the largest relative signal intensity (a-MnO_x) showed the highest current with 5-HMF present and were able to sustain > 1 mA cm^{-2} for 4 hours during CPC. Through MnO_x surface XPS analysis and solution ICP-MS, we identify a spontaneous chemical process in which 5-HMF dissolves the Mn film. The applied bias in this solution leads to much smaller alterations to Mn AOS, solution Mn concentration and film discoloration/removal, suggesting the 1.65 V vs RHE applied introduces a new reactive pathway that protects MnO_x in this electrolyte.

Chapter 1

Introduction

1.1. Impacts of our Energy Infrastructure on the Planet

1.1.1. The Warming of Earth's Atmosphere

Anthropogenic greenhouse gas (GHG) emissions are the primary driver of climate change, producing several environmentally destabilizing effects, including ocean acidification, rising sea levels and increasingly severe weather.[1,2] The Intergovernmental Panel on Climate Change (IPCC) has reported that human-induced warming has already increased the combined global surface air

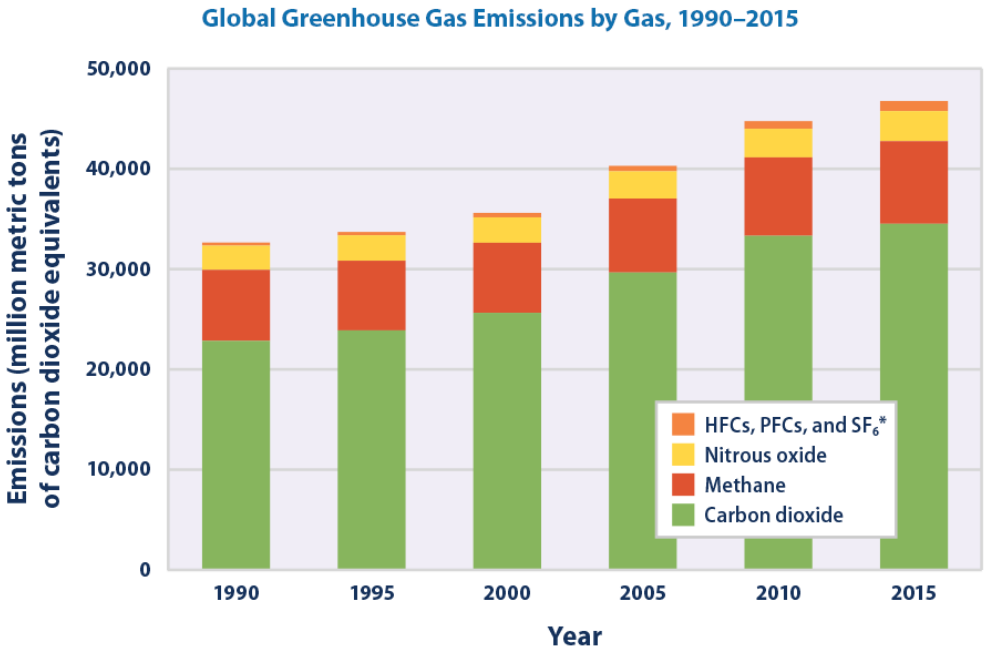

Figure 1.1. Worldwide raw GHG emissions over time for the most significant contributors. Adapted from Ref. 3.

and sea surface average temperature by 1 ºC (2017) since preindustrial levels (1850–1900).[3] Between 1990 and 2015, worldwide emission of GHGs increased by 43% with carbon dioxide (CO_2) representing between 70%–80% of total emissions (Figure 1.1).[4] This rapid atmospheric carbonization will lead to a predicted 0.2 ºC decade^{-1} increase under current fossil fuel consumption trends. At temperatures exceeding 2.0 ºC above preindustrial levels—expected

before 2100—experts indicate a significant portion of the human population will experience severe drought, heat waves, water scarcity, food insecurity and health risks, with impoverished communities experiencing the harshest effects.[5]

Understanding the end-use of fossil fuels by different economic sectors allows for the development of replacement strategies. In 2020, the transportation sector produced the most CO_2 emissions (35.7%) followed by the industrial sector (28.7%) despite representing 26.2% and 33.5% of energy consumption, respectively.[6] Transportation is a particularly pollution-rich sector due nearly exclusive reliance on fossil fuel inputs. Other sectors—industrial, residential, commercial, etc.—have abated some emissions by incorporating electric power. Electric power has a significant fraction (43%, U.S.) that is formed with non-fossil inputs, such as nuclear and renewable energy. These non-fossil inputs substantially reduce CO_2 emissions relative to fossil fuels, demonstrating their potential for carbon-free energy production (Figure 1.2). The reliance on buried carbon reserves is unequivocally warming the planet; switching to low-carbon or carbon-free energy sources is imperative to slow or halt the temperature increase.

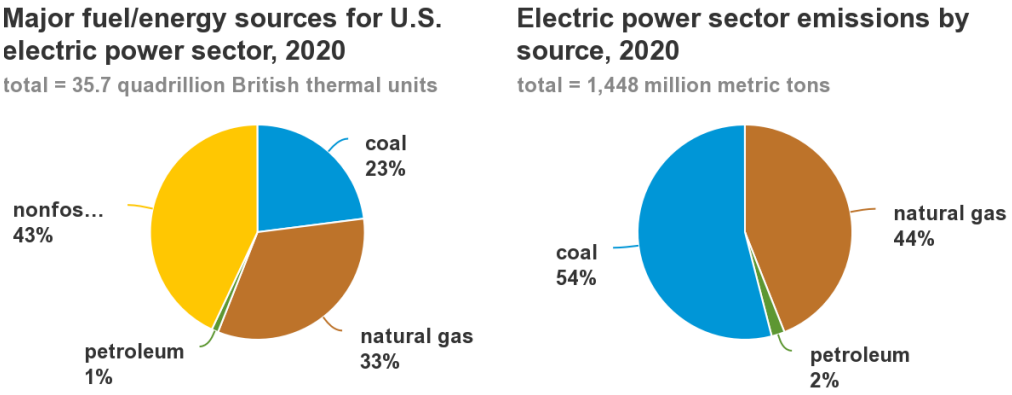

Figure 1.2. Contribution by energy source for electric power generation (left); CO_2 emissions produced from each energy source used in electric power generation. Adapted from Ref. 4.

1.1.2. Striving for Something Better

Global primary energy consumption in 2050 is expected to increase by ~50% relative to the ~600 x 10^{15} BTU used in 2018.[7] Given this dynamic energy challenge, the need for a rapid and sustainable pivot to clean energy alternatives is clear. Current non-fossil fuel primary energy sources can be divided into two categories: nuclear and renewable. While nuclear power may play a role in the transition to net-zero carbon emissions for electricity generation, its exploitation of finite resources, significant time and land commitments, as well as prohibitive costs limit the viability of this resource.[8,9]

Renewable energy sources come in many forms and offer several key advantages over nuclear. Sunlight constantly bombards the Earth's surface and naturally replenishes renewable resource fountains—biomass, hydropower, and wind—in flow-limited yet seemingly infinite fashion.[10,11] The sun delivers a collective 1.2 x 10^5 TW to the Earth each year, dwarfing the expected rates of global energy consumption in 2050 (27.6 TW) and 2100 (43.0 TW) by 4 orders of magnitude.[12] Despite the high abundance of solar irradiation, intermittency and location-dependent availability render direct solar energy use an incomplete strategy for decarbonizing our global energy infrastructure. To resolve these limitations, scientists have considered storing a fraction of incident solar photons in chemical bonds—mimicking photosynthesis—for later use.[13] Chemical fuels possess much greater energy storage capability than current solid-state batteries making storage in chemical bonds key for future grid storage applications.[14,15]

Hydrogen (H_2) makes for a suitable grid storage platform with its exceptional gravimetric energy density but is a poor choice for combustion-based transportation fuel due to storage difficulties (low volumetric energy density, **Table 1.1.**).[16] Instead, transportation fuels can be developed within a hydrogen infrastructure through hydrogenation of carbon dioxide/monoxide inputs followed by carbon chain upgrading through Fischer-Tropsch synthesis.[17,18]

Table 1.1. Energy density values for common liquid fuels and state-of-the-art batteries. Adapted from Ref. 16.

Source	Gravimetric energy density (W h kg^{-1})	Volumetric energy density (W h L^{-1})
Fuels		
Gasoline	12330	9060
Diesel	12700	10700
Propane	12870	7490
Methanol	5620	4470
Ethanol	7490	5890
Liquid Hydrogen	33570	2200
Batteries		
Li-Ion Battery	150–210	450
Ni-Metal hydride	70	220
Zn-Air battery	300	240

Hydrogen is predominately formed via steam-methane reforming (Equation 1.1) and the water-gas shift reaction (Equation 1.2) to convert methane—obtained from natural gas—to CO_2 and H_2.[19]

$$CH_4 + H_2O + \text{Heat} \longrightarrow CO + 3H_2 \quad (1.1)$$

$$CO + H_2O \longrightarrow CO_2 + H_2 + \text{Heat} \quad (1.2)$$

As the hydrogen economy matures, renewable inputs such as water and biomass are expected to supplant the exploitation of fossil fuels for this high value fuel/commodity.

1.2. Coupling Anodic Reactions to Hydrogen Fuel Generation

1.2.1. The Water Splitting Reaction

Water electrolysis—first demonstrated in 1789—represents a fossil fuel-free route to sustainable hydrogen generation.[20] Energy is required to drive this thermodynamically disfavored (electrolytic) reaction, requiring a minimum threshold energy (ΔG) of 237.2 kJ mol^{-1}.[21] The thermodynamic threshold energy spent to split water into molecular oxygen (O_2) and H_2 is stored as chemical potential energy, outlining the energy storing function of the hydrogen platform; combustion of hydrogen gas in the presence of oxygen releases the minimum threshold energy (ΔG) for each mole of H_2O formed. Water splitting (Equation 1.5) consists of an oxidation half reaction—the oxygen evolution reaction (OER)—at the anode, forming O_2 (Equation 1.3) and a reduction half reaction—the hydrogen evolution reaction (HER)—at the cathode, where protons are reduced to H_2 (Equation 1.4) using electrons provided from OER.

$$\text{Anode:} \quad H_2O(l) \xrightarrow{-2e^-} 0.5O_2(g) + 2H^+ \quad E° = 1.23 \text{ V vs NHE} \quad (1.3)$$

$$\text{Cathode:} \quad 2H^+(aq) \xrightarrow{+2e^-} 2H_2(g) \quad E° = 0.00 \text{ V vs NHE} \quad (1.4)$$

$$\text{Net:} \quad H_2O(l) \longrightarrow 0.5O_2(g) + 2H_2(g) \quad E_{cell} = -1.23 \text{ V} \quad (1.5)$$

Typically, the *actual* energy required to drive water splitting (or burn hydrogen) exceeds the threshold energy due to the path (or mechanism) used to bridge these thermodynamic states. The oxygen evolution half reaction (Equation 1.3) limits the rate of overall water splitting due to severely sluggish kinetics involved; this energy penalty ($\Delta G^{\ddagger}$) significantly reduces the efficiency

of this energy storage platform, motivating the design and preparation of catalysts, or species able to lower path-dependent energy barriers ($\Delta G^{\ddagger}_{cat} \leq \Delta G^{\ddagger}$) between states without undergoing a permanent change.[22]

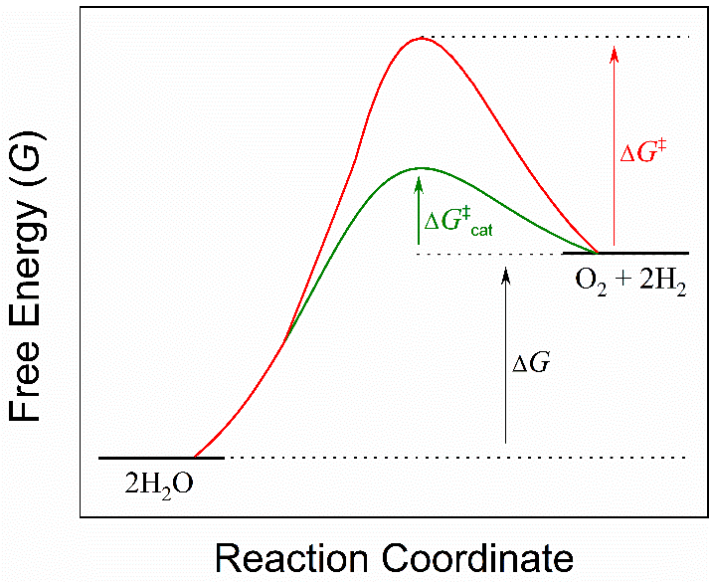

Figure 1.3. Reaction coordinate diagram for catalyzed (green) and uncatalyzed (red) path energies for water splitting.

Fujishima and Honda were the first to demonstrate light-driven water splitting on titanium(IV) oxide (TiO_2) electrodes, providing the link for direct conversion of solar photons into hydrogen.[23] Water splitting provides a clean and renewable means of generating hydrogen for solar energy storage, yet the energy cost of driving complementary OER limits practical implementation.[24] To address this issue, alternative anodic processes yielding protons for HER and more economically fruitful oxidation products have been considered.

1.2.2. Valorization of Inedible Biomass as a Water Splitting Alternative

Carbonyl compounds—formed from selective alcohol oxidation—remain key reagents in organic synthesis, making this fundamental transformation of high interest in academic and industrial settings.[25] Partial alcohol oxidation (Equation 1.6) affords one mole of oxidized aldehyde/ketone product and two moles of protons for each mole of alcohol oxidized. This process replaces low value O_2 formation—from water splitting—with desirable carbonyl generation while providing the requisite protons for HER. Alcohol substrates typically have less positive

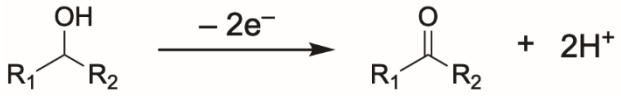

(1.6)

thermodynamic potentials than the 1.23 V vs NHE required for OER, reducing the energy cost for coupled H_2 production;[26,27] Replacing water with ethanol in state-of-the-art proton exchange membrane (PEM) electrolyzers afforded a 28.68 kW h reduction for each kilogram of H_2 produced.[28] Coupling hydrogen production with facile value-added organic oxidations represents a three-fold improvement over water splitting platforms, provided the alcohol substrates are renewable.

Inedible biomass—lignin, cellulose, and hemicellulose—is a rich renewable resource capable of supplanting many chemical industries currently relying on petrochemical feedstocks.[29] Bio-derived alcohols are readily obtained from biomass processing—such as ethanol through ABE fermentation,[30] and glycerol through transesterification of triglycerides[31]— providing a unique opportunity to couple fuel-forming reactions with commodity synthesis.[32] A carbon neutral replacement to polyethylene terephthalate, a downstream petrochemical, comes from the selective oxidation of 5-hydroxymethylfurfural (5-HMF), readily obtained from the dehydration of monosaccharides. Selective oxidation of 5-HMF to 2,5-diformylfuran (DFF) by two electrons and two protons, or 2,5-furandicarboxylic acid (FDCA) by six (total) electrons produces two distinct bio-derived comonomers (Equation 1.7).

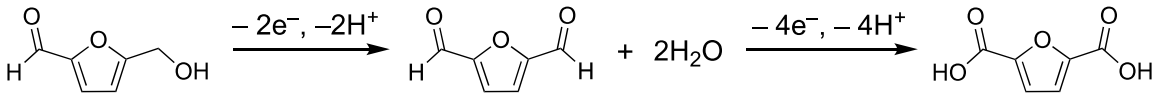

(1.7)

Both products offer enticing options, as DFF is ripe for Schiff base polymerization with diamines,[33] and FDCA represents a structural analog to terephthalic acid, replacing terephthalic acid in condensation polymerization.[34] Given the economic and environmental motivators for performing these chemical transformations, similar considerations must be afforded to catalyst development.

1.3. Solar Photons for Photo(electro)chemical Transformations

1.3.1. The Role of Semiconductors in Photo(electro)chemistry

Photocatalysis functions through the light-driven promotion of ground state electrons to higher energy excited states, creating reactive and transient species capable of performing redox reactions. For single molecules, the energy between the highest occupied molecular orbital (HOMO) and lowest unoccupied molecular orbital (LUMO), called the HOMO–LUMO gap,

defines the threshold photon energy; only light of energy equal to the HOMO–LUMO gap or greater may induce a photoexcitation event. For extended solids, an array of many overlapping

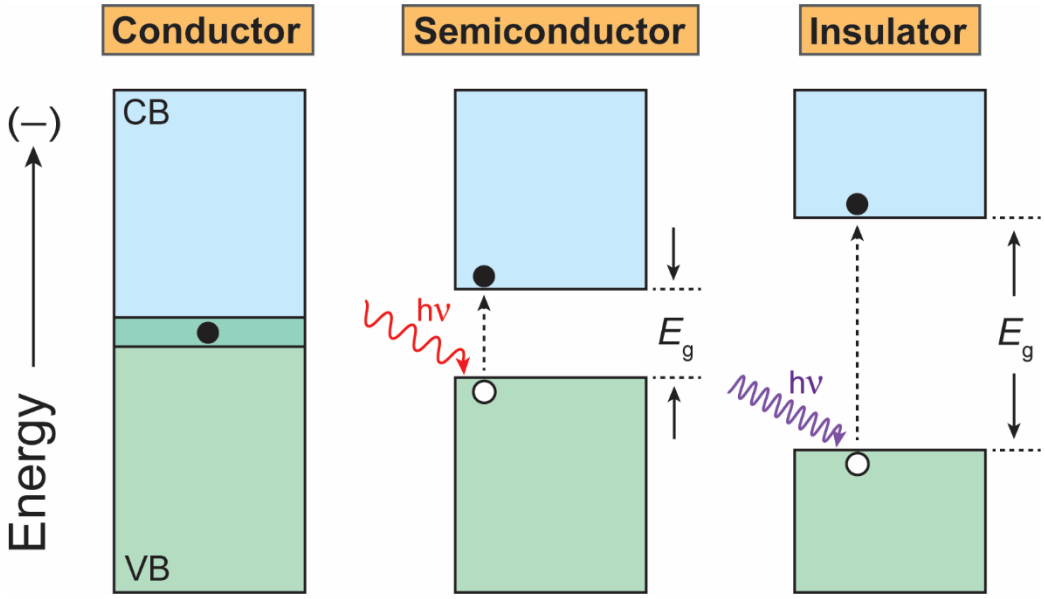

Figure 1.4. Energy band diagram depicting valence band (VB) and conduction band (CB) arrangements in solids.

HOMO and LUMO orbitals ($\geq 10^{23}$) gives rise to continuous bands of discrete states called the valence band (from HOMO orbitals) and conduction band (from LUMO orbitals). Depending on the HOMO-LUMO gap of constituent molecular orbitals, the extended solid will have fundamentally different electronic properties. For simplicity, the band edges are displayed with a curvature of 0 (flat), but real semiconductor bands have curved potential energy surfaces due to the wave nature electrons in the lattice.

Semiconductors have a region between the valence and conduction bands called the forbidden region, as it possesses no available states for electron population. This characteristic energy difference, called the band gap (E_g), defines the type of light (photon energy, hν) required to photoexcite an electron. When an incident photon promotes an electron to the conduction band, an electron vacancy—called a hole (h^+)—is left behind in the valence band. The electron and hole formed from a light absorption event can be used in reduction and oxidation reactions, respectively, provided the electron–hole pair doesn't undergo radiative recombination. The light-driven creation of electron-hole pairs and their separation for redox reactions is the foundational process in direct solar energy storage. For the photogenerated e^-–h^+ pairs to perform their corresponding redox half reactions in photocatalysis, the thermodynamic potentials for those half reactions must fall within the band gap of the semiconductor; the thermodynamic potential for the

reduction half reaction must be less negative than the conduction band minimum (CBM), and the potential for the oxidation half reaction must be more negative than the valence band maximum (VBM) (Figure 1.5). Thermodynamic exclusion of either half reaction precludes the full light-driven redox cycle, but depending on the composition of the semiconductor, different band positions—and band gaps—can be utilized to perform the desired redox processes.

1.3.2. Metal Oxides as Photoelectrodes

The list of necessary features a photocatalyst must have—strong light absorption (small band gap, low e^-–h^+ recombination), band gap–redox potential alignment and redox stability during catalysis—makes identification of a single material to satisfy all criteria exceedingly difficult. To address thermodynamic harmony (band gap–redox potential alignment) and redox stability, many experts have shifted to photoelectrochemical applications, where semiconductors are only required to perform one light-driven half reaction while maintaining their catalytic activity.[35] Implementation of a photoelectrochemical cell allows for each semiconductor material to be fine-

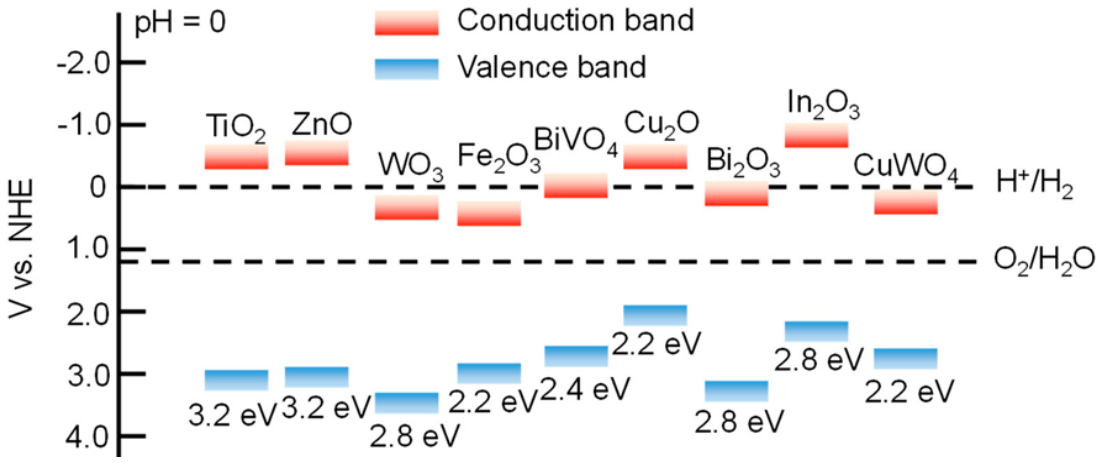

Figure 1.5. Band positions for common metal oxide semiconductors scaled against the normal hydrogen electrode. Dotted lines indicate redox potentials for the given reactions. Adapted from Ref. 38.

tuned for a single redox half reaction, which is strategically important when one half reaction limits the overall rate of the reaction (OER in H_2O splitting).[36] Metal oxide semiconductors often have sufficiently oxidizing valence bands but possess conduction band minima that are too positive to reduce protons, making them excellent candidates for photoanodes to perform oxidation half reactions (Figure 1.5).[37,38] These light-absorbers tend to possess high (oxidative) stability under photoelectrochemical stress, resulting from the strength of the oxide bond found commonly in nature.[39]

Due to the presence of crystallographic defects commonly formed during synthesis—oxygen or metal atom vacancies, interstitially-displaced atoms—metal oxides can have higher electronic conductivity than defect-free intrinsic semiconductors due to the introduction of states into the forbidden region.[40] When donor states are introduced in the band gap, electrons become the majority charge carrier and the material is classified as *n*-type; acceptor states in the band gap lead to electron-deficient materials, with holes serving as the majority charge carrier (*p*-type). The Fermi level (E_F)—used to describe the average electrochemical potential of electrons in a system—is influenced by the introduction of new states in the band gap and subsequently shifts in the direction of the added states (more negative for *n*-type; more positive for *p*-type) (Figure 1.6).

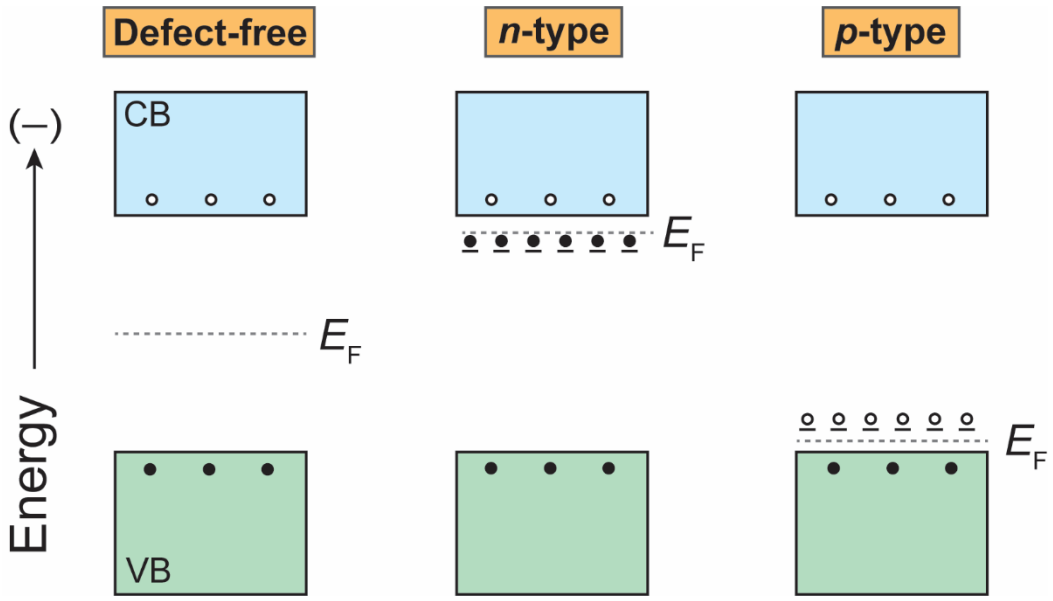

Figure 1.6. Location of the Fermi level (E_F) within the intrinsic semiconductor band gap and influence of added donor (*n*-type) and acceptor (*p*-type) states at 0 K. Electrons are depicted as filled black dots and holes as hollow dots.

This adjustment in the Fermi level position has important (photoelectrochemical) implications in the behavior of semiconductors at a junction. Placing a semiconductor electrode into an electrolyte solution induces an equilibration event driven by the difference in electron potential energy (Fermi levels) between the species forming the junction. Electrons will flow from the substance possessing higher (more negative) electrochemical potential to the substance with a lower (less negative) potential until the Fermi level is equal on both sides of the junction. When the semiconductor equilibrates, its band gap is preserved, but the position of the bands in the bulk material are displaced relative to the surface band positions in a process called band bending (Figure 1.7).

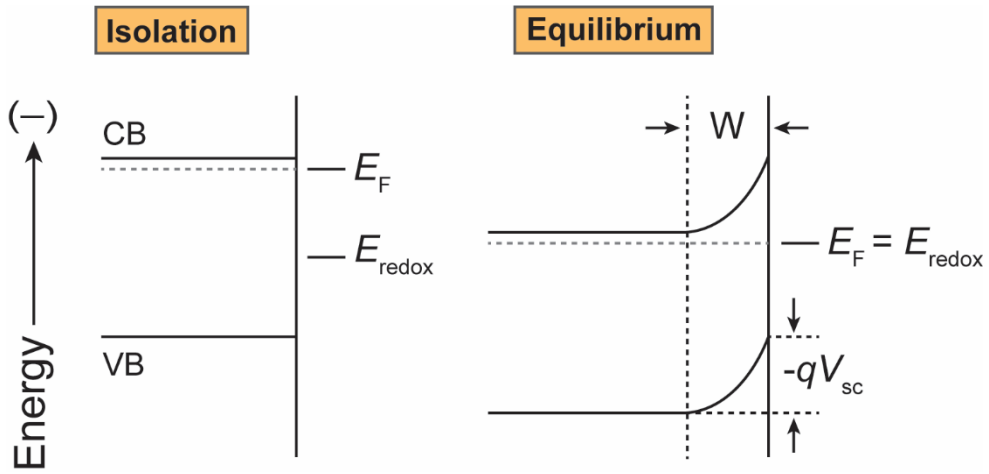

Figure 1.7. Demonstration of the band bending phenomenon following Fermi level equilibration.

For *n*-type semiconductors, the E_F is generally more negative than that of the electrolyte solution, leading to bands bending to more positive potentials as electrons are pushed into solution. Band bending generates an electric field between the surface and bulk of a semiconductor—called the space charge layer (W)—that aids charge separation for photogenerated e^-–h^+ pairs; larger band bending introduces greater built-in voltages (V_{sc}). For *n*-type materials, the built-in voltage serves to drive holes to the surface (and electrons toward the back contact) where oxidations are performed, making these materials suitable for photoanodes. *P*-type materials, suitable as photocathodes, undergo upward band bending (more negative in the bulk than the surface) providing an electric field for electrons to move to the surface. In the presence of light, the extent of band bending is reduced due to the promotion of electrons to the conduction band but can be adjusted by the application of an external electric field (applied bias) to assist with charge separation. The application of a positive external bias (used in photo*electro*chemistry) acts to drive holes to the semiconductor surface, assisting the built-in voltage in tunable fashion. The difference in potential between the valence band maximum (E_{VBM}) of the *n*-type semiconductor and the redox potential of the oxidation half reaction provides the driving force—overpotential, η—for a photoelectrochemical reaction to occur. Unlike metallic electrodes, where applied bias can

influence the overpotential (continuum of available states), the applied bias on a semiconductor only serves to facilitate photogenerated charge pairs by exacerbating band bending (Figure 1.8).[41]

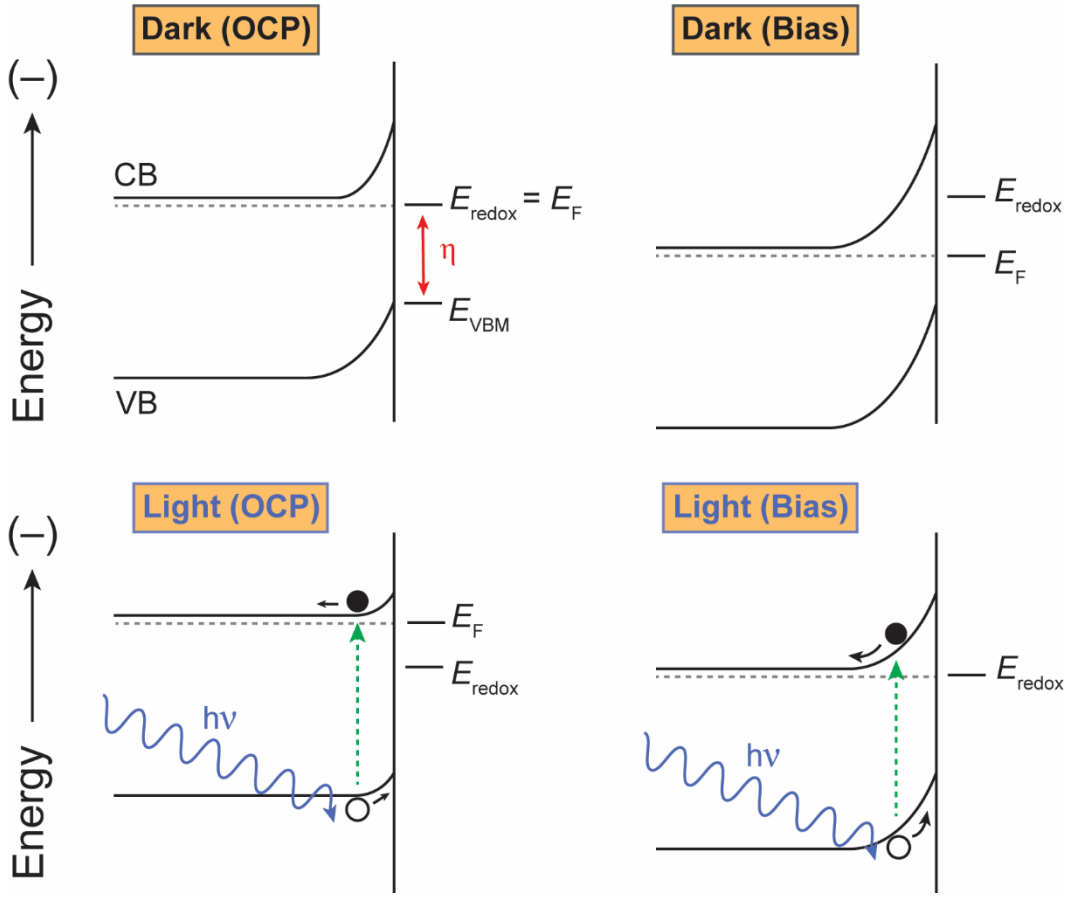

Figure 1.8. Band diagrams displaying influences of illumination (hν) and applied potential on band bending.

Due to the large overpotential provided by metal oxide valence bands for oxidation reactions, selectivity in organic oxidation reactions can be difficult to ensure. Photo(electro)chemical alcohol oxidation has been performed on metal oxides in aqueous and nonaqueous media, but often require homogenous and heterogenous strategies to modulate reactivity.[42–44]

1.4. Strategies for Chemical Control of the Photoelectrode-Solution Interface

1.4.1. Redox Mediators for Indirect Oxidations

Redox active species capable of facilitating an indirect redox event as solution-phase catalysts can impart unique chemical control between the light absorber and reactant. These species often improve poor rates of heterogenous charge transfer, reducing deleterious surface carrier recombination (SCR) events and mitigating deleterious auto-oxidation (AO) processes (Figure 1.11).[45,46] As a general approach, mediator activation from an otherwise inert species in

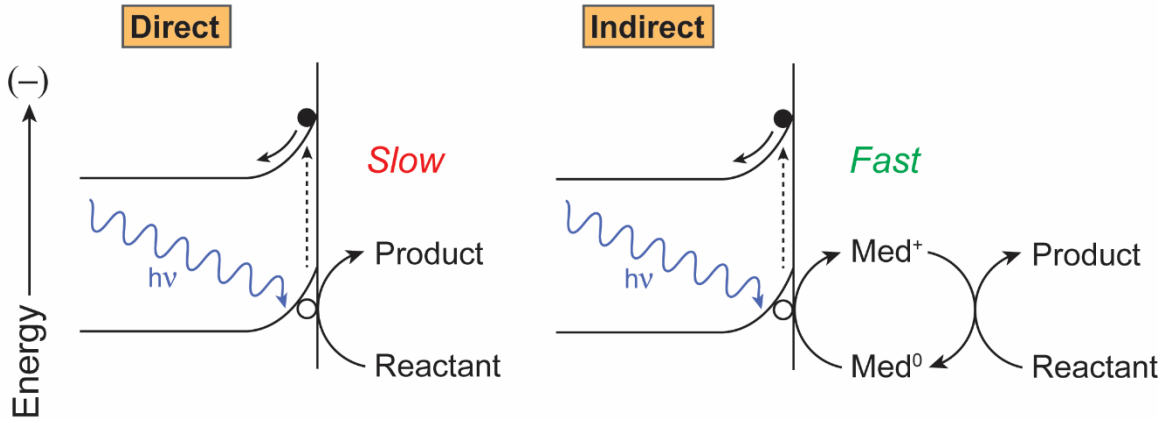

Figure 1.9. Depiction of direct heterogenous catalysis (left) compared to heterogenous activation of solution-phase co-catalyst.

the electrolyte represents a much safer route than traditional stoichiometric reactions and offers superior atom economy. For alcohol oxidation, nitroxyl-based mediators have been extensively explored due to the ease in forming an oxoammonium intermediate, which has unique selectivity toward primary and secondary alcohol substrates in aqueous and nonaqueous conditions.[47,48] While this mediator has demonstrated cooperativity with other catalysts, its suitability as a cocatalyst is not absolute; on bismuth vanadate photoelectrodes, TEMPO/TEMPO$^+$ nitroxyl mediator functioned as a recombination center and required an additional interfacial layer (cobalt phosphate) to behave as the desired mediator for 5-HMF oxidation. The inherent limitation provides the necessary impetus to develop other classes of redox mediators for co-catalyzed alcohol oxidation reactions.

Recently, the Bartlett group achieved selective primary alcohol oxidation on visible light absorbing cadmium sulfide photocatalysts and revealed a cooperative electrolyte activation event (nitrate anion oxidation) that rapidly increased the rate of conversion.[49] Nitrate behaved as a catalyst in this system, representing an underexplored redox mediator for alcohol oxidation.

Chapters 2 & 3 in this thesis offer a novel understanding of nitrate-mediated alcohol oxidation in acetonitrile and provide critical guidance in addressing the newfound limitations within.

1.4.2. Material Defect Engineering to Tailor Surface Reactivity

Altering the type of reactive site on a material surface—or distribution of sites—can have profound impacts on the electrochemical behavior toward redox reactions. The chemical nature of a material surface can also be manipulated through the presence of crystallographic defects, which to this point, has only been considered for altering the conductivity of semiconductors. According to Sabatier's principle, catalyst activity is optimized when the interactions between the (heterogeneous) catalyst and substrate are of intermediate strength;[50] intermediate strength interactions offer favorable binding energies for substrates that are not too strong as to trap intermediate(s) on the surface. Depending on substrate/intermediate size, the active site during heterogenous catalysis can include an "ensemble" or grouping of surface atoms; when surface defects exist, they can alter the binding affinity of substrates or intermediates at the ensemble, manifesting as stark changes in preferential reactivity and reaction rates.[51] Defect engineering was recently used to tune selectivity for OER in brine ($[NaCl]_{aq}$ = 0.5 M – 0.6M)—where CER typically dominates—by introducing oxygen vacancies as a new reactive site in MnO_2 electrocatalysts.[52] The exploitation of material defects for selective alcohol oxidation in aqueous media represents a rich opportunity to reduce catalyst—or co-catalyst—complexity in biomass valorization platforms; the development of this platform will be discussed with preliminary detail presented at the end of this thesis to provide a suitable anodic half reaction to couple with H_2 generation.

1.5. Thesis Scope

Exploration into water oxidation alternatives for coupled (photo)electrochemical H_2 generation is a consistent theme developed in the chapters of this thesis. In Chapter 1.2, we discuss the numerous benefits of replacing water oxidation with bio-renewable alcohol oxidation as a proton source for HER. Aldehydes, ketones, and carboxylic acids are common industrial feedstocks readily obtained from selective alcohol oxidation. Importantly, developing platforms using bio-renewable alcohols (ethanol, butanol, 5-hydroxymethylfurfural, glycerol, etc.) reduces our reliance on petrochemically-derived alcoholic feedstocks for chemical manufacture. In Chapter 1.4, we motivate the use of light-absorbing semiconductors as photo(electro)catalysts in the pursuit of sustainable reactor conditions for alcohol oxidation; we end Chapter 1.4 with consideration of state-of-the-art material defects and their role in preferential reactivity during

electrocatalysis. The cumulative work of this thesis details important material and solution conditions that promote selective alcohol oxidation.

Chapter 2 explores the cooperativity of solution-phase nitrate and light absorbing bismuth vanadate photoelectrodes for photoelectrochemical benzyl alcohol oxidation in acetonitrile solvent. Tetrabutylammonium nitrate is a viable nitrate source able to increase the rate of benzyl alcohol oxidation by introducing an indirect oxidation pathway. The mode of reactivity observed here is fundamentally different than the photochemical work that motivated this investigation by two key distinctions: (1) a metal nitrate salt was not required to activate nitrate toward benzyl alcohol oxidation and (2) nitrate facilitates alcohol oxidation in stoichiometric fashion under photoelectrochemical control. This work expands the understanding of nitrate-facilitated alcohol oxidation in acetonitrile but presented system-dependent discrepancies that required further exploration.

Chapter 3 delivers a general depiction of nitrate-mediated alcohol oxidation in acetonitrile resolving the discrepancies revealed in Chapter 2. Using platinum electrodes, we showed that nitrate is also consumed in stochiometric fashion—under electrochemical control—associated with the buildup of inert nitric acid; introducing a suitable base (2,6-lutidine) promoted a reintroduction of nitrate to the catalytic cycle. Rotating ring-disk electrochemistry revealed a proton-coupled oxygen reduction event during nitrate oxidation due to HNO_3 formation. These results support a previously unknown role of reduced oxygen species, serving as an in-situ generated base during photochemical nitrate-mediated alcohol oxidation. This work provides a description for general nitrate behavior in acetonitrile and reveals the importance of light-driven half reaction spatial separation.

Continuing with alcohol oxidation as a target, Chapters 4 and 5 develop electrocatalytic alcohol oxidation in brine or near-brine conditions motivated by the ubiquity of seawater. $Ni(OH)_2$ electrodes were used to alkalized brine to promote the formation of NiOOH electrocatalyst, requiring pH ≥ 12. 1-Butanol oxidation (to butyric acid) occurs before the ~1.58 V vs RHE takeoff observed for the background current (OER or CER), demonstrating the preferential reactivity of this electrode material in conditions were CER often dominates (kinetically). Chapter 5 addresses the reliance on alkalized brine for electrocatalytic activity by exploring oxygen vacancy-rich $A_xMnO_{2-\delta}$ films, shown previously enable selective OER in neutral brine.

References

[1] Ripple, W. J.; Wolf, C.; Newsome, T. M.; Banard, P.; Moomaw, W. R. World's scientists' warning of a climate emergency *Bioscience* **2019**, *5*, 969.

[2] Papadis, E.; Tsatsaronis, G. Challenges in the decarbonization of the energy sector. *Energy* **2020**, *205*, 118025.

[3] IPCC. https://www.ipcc.ch/sr15/ (Accessed August 18, 2021)

[4] Indicators. https://www.epa.gov/climate-indicators/climate-change-indicators-global-greenhouse-gas-emissions (Accessed August 17, 2021)

[5] 2.0 °C NASA. https://climate.nasa.gov/news/2865/a-degree-of-concern-why-global-temperatures-matter/ (Accessed August 18, 2021)

[6] GHG Emissions. https://www.eia.gov/energyexplained/energy-and-the-environment/where-greenhouse-gases-come-from.php (Accessed August 17, 2021)

[7] Energy Demand vs. Time. https://www.eia.gov/todayinenergy/detail.php?id=41433 (Accessed August 18, 2021)

[8] Muellner, N.; Arnold, N.; Gufler, K.; Kromp, W.; Renneberg, W.; Liebert, W. Nuclear energy – The solution to climate change? *Energy Policy* **2021**, *155*, 112363.

[9] Buongiorno, J.; Corradini, M.; Parsons, J.; Petti, D. Nuclear Energy in a Carbon-Constrained World: Big Challenges and Big Opportunities. *IEEE Power and Energy Magazine* **2019**, *17*, 69–77.

[10] Renewables. https://www.eia.gov/energyexplained/renewable-sources/ (Accessed August 18, 2021)

[11] Qazi, A.; Hussain, F.; Rahim, N. ABD.; Hardaker, G.; Alghazzai, D.; Shaban, K.; Haruna, K. Towards Sustainable Energy: A Systematic Review of Renewable Energy Sources, Technologies, and Public Opinions. *IEEE Access* **2020**, *7*, 63837–63851.

[12] Lewis, N.S.; Nocera, D. G. Powering the Planet: Chemical Challenges in Solar Energy Utilization *Proc. Natl. Acad. Sci. U. S. A.* **2006**, *103*, 15729–15735.

[13] Zhang, B.; Sun, L. Artificial photosynthesis: opportunities and challenges of molecular catalysts. *Chem. Soc. Rev.*, **2019**, *48*, 2216–2264.

[14] Hammarström, L. Catalyst: Chemistry's Role in Providing Clean and Affordable Energy for All. *Chem*, **2016**, *1*, 515–518.

[15] Winter, M.; Brodd, R. J. What Are Batteries, Fuel Cells, and Supercapacitors? *Chem. Rev.* **2004**, *104*, 4245–4270.

[16] Gür, T. M. Review of electrical energy storage technologies, materials and systems: challenges and prospects for large-scale grid storage. *Energy Environ. Sci.* **2018**, *11*, 2696.

[17] Gong, J.; English, N. J.; Pant, D.; Patzke, G. R.; Protti, S.; Zhang, T. Power-to-X: Lighting the Path to a Net-Zero-Emission Future. *ACS Sustainable Chem. Eng.* **2021**, *9*, 7179–7181.

[18] Chen, Y.; Wei, J.; Duyar, M. S.; Ordomsky, V. V.; Khodakov, A. Y.; Liu, J. Carbon-based catalysts for Fischer-Tropsch synthesis. *Chem. Soc. Rev.* **2021**, *50*, 2337–2366.

[19] H_2 Production. https://www.energy.gov/eere/fuelcells/hydrogen-production-natural-gas-reforming (Accessed August 23, 2021)

[20] Chisholm, G.; Cronin, L. Chapter 16 – Hydrogen from Water Electrolysis. In Storing Energy: with special reference to renewable energy sources. Elsevier Inc., 2016; pp 318.

[21] Moniz, S. J. A.; Shevlin, S. A.; Martin, D. J.; Guo, Z.-X.; Tang, J. Visible-light driven heterojunction photocatalysts for water splitting – a critical review. *Energy Environ. Sci.* **2015**, *8*, 731–759.

[22] Wang, S.; Lu, A.; Zhong, C.-J. Hydrogen production from water electrolysis: role of catalysts. *Nano Convergence* **2021**, *8*.

[23] Fujishima, A.; Honda, K. Electrochemical Photolysis of Water at a Semiconductor Electrode. *Nature* **1972**, *238*, 37–38.

[24] Wang, Q.; Domen, K. Particulate Photocatalysts for Light-Driven Water Splitting: Mechanisms, Challenges, and Design Strategies. *Chem. Rev.* **2020**, *120*, 919–985.

[25] Wang, D.; Wang, P.; Wang, S.; Chen, Y.-H.; Zhang, H.; Lei, A. Direct electrochemical oxidation of alcohols with hydrogen evolution in continuous-flow reactor. *Nat. Commun.* **2019**, *10*, 2796.

[26] Lhermitte, C. R.; Sivula, K. Alternative Oxidation Reactions for Solar-Driven Fuel Production. *ACS Catal*. **2019**, *9*, 2007–2017.

[27] Daas, B. M.; Ghosh, S. Fuel cell applications of chemically synthesized zeolite modified electrode (ZME) as catalyst for alcohol electrooxidation – A review. *J. Electroanal. Chem.* **2016**, *783*, 308–315.

[28] Reid, L. M.; Li, T.; Cao, Y.; Berlinguette, C. P. Organic chemistry at anodes and photoanodes. *Sustainable Energy Fuels* **2018**, *2*, 1905.

[29] Tuck, C. O.; Pérez, E.; Horváth, I. T.; Sheldon, R. A.; Poliakoff, M. Valorization of Biomass: Deriving More Value from Waste. *Science* **2012**, *337*, 695–699.

[30] Karimi, K.; Tabatabaei, M.; Horváth, I. S.; Kumar, R. Recent trends in acetone, butanol, and ethanol (ABE) production. *Biofuel Res. J.* **2015**, *8*, 301–308.

[31] Gebremariam, S. N.; Marchetti, J. M. Economics of biodiesel production: Review. *Energy Convers. Manage.* **2018**, *168*, 74–84.

[32] Mariscal, R.; Maireles-Torres, P.; Ojeda, M.; Sádaba, I.; Granados, M. L. Furfural: a renewable and versatile platform molecule for the synthesis of chemicals and fuels. *Energy Environ. Sci.* **2016**, *9*, 1144–1189.

[33] Xiang, T.; Liu, X.; Yi, P.; Guo, M.; Chen, Y.; Wesdemiotis, C.; Xu, J. Pang, Y. Schiff base polymers derived from 2,5-diformylfuran. *Polym. Int.* **2013**, *62*, 1517–1523.

[34] van Putten, R.-J.; van der Waal, J. C.; de Jong, E.; Rasrendra, C. B.; Heeres, H. J.; de Vries, J. G. Hydroxymethylfurfural, A Versatile Platform Chemical Made from Renewable Resources. *Chem. Rev.* **2013**, *113*, 1499– 1597

[35] Li, J.; Wu, N. Semiconductor-based photocatalysts and photoelectrochemical cells for solar fuel generation: a review. *Catal. Sci. Technol.* **2015**, *5*, 1360–1384.

[36] Bediako, D. K.; Surendranath, Y.; Nocera, D. G. Mechanistic Studies of the Oxygen Evolution Reaction Mediated by a Nickel-Borate Thin Film Electrocatalyst. *J. Am. Chem. Soc.* **2013**, *135*, 3662.

[37] Sivula, K.; van de Krol, R. Semiconducting materials for photoelectrochemical energy conversion. *Nat. Rev. Mater.* **2016**, *1*, 15010.

[38] Chen, Y.; Feng, X.; Liu, Y.; Guan, X.; Burda, C.; Guo, L. Metal Oxide-Based Tandem Cells for Self-Biased Photoelectrochemical Water Splitting. *ACS Energy Lett.* **2020**, *5*, 844–866.

[39] Yang, Y.; Niu, S.; Han, D.; Liu, T.; Wang, G.; Li, Y. Progress in Developing Metal Oxide Nanomaterials for Photoelectrochemical Water Splitting. *Adv. Energy Mater.* **2017**, *7*, 1700555.

[40] Wang, C.; Sun, J.; Gou, H.; Wang, S.; Zhang, J.; Tao, X. Intrinsic defects and their effects on the optical properties in the nonlinear optical crystal $CdSiP_2$: a first-principles study. *Phys. Chem. Chem. Phys.* **2017**, *19*, 9558.

[41] Cha, H. G.; Choi, K.-S. Combined biomass valorization and hydrogen production in a photoelectrochemical cell. *Nat. Chem.* **2015**, *7*, 328–333.

[42] Tateno, H.; Miseki, Y.; Sayama, K. Photoelectrochemical Oxidation of Benzylic Alcohol Derivatives on $BiVO_4/WO_3$ under Visible Light Irradiation. *ChemElectroChem* **2017**, *4*, 3283–3287.

[43] Li, T.; Kasahara, T.; He, J.; Dettelbach, K. E.; Sammis, G. M.; Berlinguette, C. P. Photoelectrochemical oxidation of organic substrates in organic media. *Nat. Commun.* **2017**, *8*, 390.

[44] Luo, L.; Wang, Z.-j.; Xiang, X.; Yan, D.; Ye, J. Selective Activation of Benzyl Alcohol Coupled with Photoelectrochemical Water Oxidation via a Radical Relay Strategy. *ACS Catal.* **2020**, *10*, 4906–4913.

[45] Wang, Y. L.; Li, Y. H.; Wang, X. L.; Hou, Y.; Chen, A. P.; Yang, H. G. Effects of redox mediators on α-Fe_2O_3 exposed by {012} and {104} facets for photocatalytic water oxidation. *Appl. Catal., B* **2017**, *206*, 216–220.

[46] Breuhaus-Alvarez, A. G.; Cheek, Q.; Cooper, J. J.; Maldonado, S.; Bartlett, B. M. Chloride Oxidation as an Alternative to the Oxygen-Evolution Reaction on H_xWO_3 Photoelectrodes. *J. Phys. Chem. C* **2021**, *125*, 8543–8550.

[47] Anelli, P. L.; Biffi, C.; Montanari, F.; Quici, S. Fast and selective oxidation of primary alcohols to aldehydes or to carboxylic acids and of secondary alcohols to ketones mediated by oxoammonium salts under two-phase conditions. *J. Org. Chem.* **1987**, *52*, 2559–2562.

[48] Nutting, J. E.; Mao, K.; Stahl, S. S. Iron(III) Nitrate/TEMPO-catalyzed Aerobic Alcohol Oxidation: Distinguishing between Serial versus Integrated Cooperativity. *J. Am. Chem. Soc.* **2021**, *143*, 10565–10570.

[49] DiMeglio, J. L.; Breuhaus-Alvarez, A. G.; Li, S.; Bartlett, B. M. Nitrate-Mediated Alcohol Oxidation on Cadmium Sulfide Photocatalysts. *ACS Catal*. **2019**, *9*, 5732–5741.

[50] Kari, J.; Olsen, J. P.; Jensen, K.; Badino, S. F.; Krogh, K. B. R. M.; Borch, K.; Westh, P. Sabatier Principle for Interfacial (Hetergenous) Enzyme Catalysis. *ACS Catal*. **2018**, *8*, 11966–11972.

[51] Védrine, J. Heterogeneous Catalysis on Metal Oxides. *Catalysts* **2017**, *7*, 341.

[52] Abe, H.; Murakami, A.; Tsunekawa, S.; Okada, T.; Wakabayashi, T.; Yoshida, M.; Nakayama, M. Selective Catalyst for Oxygen Evolution in Neutral Brine Electrolysis: An Oxygen-Deficient Manganese Oxide Film. *ACS Catal.* **2021**, *11*, 6390–6387.

Chapter 2

Nitrate Radical Facilitates Indirect Benzyl Alcohol Oxidation on Bismuth (III) Vanadate Photoelectrodes

Portions of this chapter have been published:

Terry, B. D.; DiMeglio, J. L.; Cousineau, J. C.; Bartlett, B. M. *ChemElectroChem* **2020**, *7*, 3776–3782.

2.1. Introduction

Selective alcohol oxidation has been traditionally performed with toxic stoichiometric oxidants, including high valent chromium species.[1] Generating chemical oxidant *in-situ* through activation of otherwise inert reagents in solution can provides a safer route to produce carbonyl compounds from alcohol substrates.[2] Within this paradigm, redox mediators are viable candidates, where an (easily) accessible activation step generates reactive radical or ionic intermediates capable of performing solution-based chemical redox processes, such alcohol oxidation.[3] Redox mediators are used varied settings—spanning catalysis to energy storage—for their ability to improve heterogenous charge transfer rates.[4–7] This facilitation of charge transfer has been utilized on earth-abundant and environmentally friendly metal-oxide light absorbers, where rates alcohol oxidation surpass those of the mediator-free system.[8,9] Indirect alcohol oxidation using a mediator has been associated with unique and often desirable product selectivity.[10,11] For selective alcohol and aldehyde oxidation, N-oxyl mediators (such as TEMPO) dominate the field with easily accessible (and reversible) redox states.[12–14]

Nitrate-mediated alcohol oxidation was first demonstrated in the early 1980s, where electrochemically generated nitrate radicals (NO_3•) react with alcohol substrates through a proposed hydrogen atom transfer (HAT) mechanism.[15] This underexplored mediator received renewed attention decades later, utilized in a biphasic system with an aqueous layer for NO_3• generation and an organic layer to maximize alcohol substrate solubility; as a result, aldehyde and ketone products were formed with high selectivity at the biphasic interface.[16,17] Nitrate anion oxidation with visible light-absorbing Acr^+-Mes dye was reported recently as the first

demonstration of nitrate radical formation with visible light inputs. NO_3• generated in this system served as a chemical oxidant for alcohols and alkynes.[18] Building on this example, the Bartlett group demonstrated cooperativity between photogenerated valence band holes on CdS nanowires and NO_3^- toward indirect alcohol oxidation in acetonitrile; this photocatalytic system oxidizes benzyl alcohol ($PhCH_2OH$) to benzaldehyde (PhCHO) with > 99 % selectivity.[19]

In this chapter, new semiconductor-nitrate systems for indirect benzyl alcohol oxidation are identified. To study the light-driven nitrate oxidation half reaction, $BiVO_4$ films were prepared and used in a photoelectrochemical cell; royal blue LEDs (λ_{max} = 448 nm) provided the requisite photons (100 mW cm^{-2}) to match the 2.4 eV band-gap absorption in $BiVO_4$.[20] Acetonitrile (MeCN) solvent was used to prepare all electrolytes and $PhCH_2OH$ was used as a model substrate to probe the cooperative features of $BiVO_4$ and nitrate.

2.2. Experimental

2.2.1. Chemicals and Materials

Solvents (acetonitrile, ethanol, benzyl alcohol) were purchased from Sigma Aldrich and used without additional purification. P-benzoquinone was purchased from Fisher and sublimed to remove impurities. Bismuth nitrate pentahydrate, vanadyl acetylacetonate, deuterated benzyl alcohol, potassium iodide and lactic acid solution (≥ 85%) were obtained from Sigma Aldrich and used without further purification. All aqueous solutions were made using Millipore water (18.2 Ω cm^{-1}). Nylon syringe filters (25 mm, 0.2 mm membrane) were purchased from VWR. Fluorine-doped tin oxide glass (NSG TEC 15) was purchased from Pilkington North America.

2.2.2. $BiVO_4$ Electrode Preparation

Fluorine-doped tin oxide (FTO) was cleaned by sonication in acetone, followed by Millipore water with detergent, then ethanol for 20 minutes each before rinsing with Millipore water and drying under N_2. The deposition solution for BiOI was made using previously reported methods, with the final pH set to 3.41 – 3.43 for the most consistent results between batches.13 Due to solid formation in the Vycor frit of Ag/AgCl reference electrodes, the open-circuit potential was measured between a platinum disk working and the Ag/AgCl reference, showing a stable potential near 0.314 V vs RE; the Pt disk was then used as a stable reference electrode for BiOI growth on FTO and showed a static open-circuit potential. The same two-step electrochemical deposition was used (–0.35 V vs Ag/AgCl for 20 s, followed by –0.1 V vs Ag/AgCl until 370 mC cm^{-2} passed)

with the open circuit between Pt disk working and Ag/AgCl reference electrodes accounted for (–0.664 V and –0.414 V vs Pt disk reference respectively). Films were rinsed with ethanol and dried gently under a stream of N_2. The BiOI was converted to $BiVO_4$ using a thermal treatment process, where 50 μL cm^{-2} of 0.2 M $VO(acac)_2$ in DMSO were drop-casted onto BiOI films before heating at 2 °C min^{-1} to 450 °C, holding for 2 hours, and cooling back to room temperature over 45 minutes. Excess V_2O_5 was dissolved off by gentle stirring in a dish of 1 M NaOH(aq) for 40 minutes. These films were rinsed with Millipore water and dried with air.

2.2.3. Characterization Procedures

UV-vis spectra of BiVO4 films were gathered using a Cary 5000 UV-vis spectrophotometer (Figure A.1). Powder X-ray diffraction data were collected on a Panalytical Empyrean diffractometer with a power of 1.8 kW (40 mA, 45 kV) using a Cu Kα radiation source (λ = 0.15418 nm). A position-sensitive 1D diffractometer (X'Celerator Scientific) equipped with a with Bragg-Brentano^{HD} X-ray optic that ensured delivery of only Kα radiation was used (Figure A.2). Surface images were obtained on an EMAL JEOL JSM-7800FLV field-emission scanning electron microscope (SEM) instrument with an accelerating voltage of 10 kV and a working distance of 10 mm in The Robert B. Mitchell Electron Microbeam Analysis Lab. Additional surface analysis was performed with X-ray photoelectron spectroscopy (XPS) with data collected on a Kratos Axis Ultra X-ray photoelectron spectrometer. Monochromatic Al Kα X-rays (1486.7 eV) were used inside an analysis chamber with a pressure of 1×10^{-9} Torr. Charging effects on semiconductor substrates were mitigated through compensation with an electron flood gun. A step size of 0.1 eV and pass energy of 20 were used to collect high-resolution spectra. Adventitious carbon (248.8 eV) was used to calibrate peak positioning for Bi 4f and V 2p peaks.

2.2.4. Photoelectrocatalysis

The light source was a single Royal Blue (λ_{max} = 447.5 nm) High Power LED from Mouser Electronics (Lumileds LXML-PR02-A900) powered by XP-603 Elenco Precision 0 – 30 V Variable Benchtop Power Supply. The light fixture was kept cool with an Arctic Alpine M1 low speed fan. A custom 2-compartment cell was constructed in-house supporting a quartz window and a 1 μm polypropylene frit to separate compartments. The compartment with the quartz window was fitted with a glass side arm to contain the Ag reference electrode at a fixed distance from the central column where a $BiVO_4$ film was supported. A Pt coil counter electrode was used in all

electrochemical measurements. A 15 mL aliquot of solution was placed in the working/reference electrode compartment along with 6.7 mL in the counter to match solution levels and prevent solution transfer due to gravity. A Teflon stir bar was placed in the working electrode side to ensure solution mixing during electrolysis. Light intensity was applied at a constant 100 mW cm^{-2} for all light-based experiments and the reaction vessel was sealed by compression with *O*-rings with screw caps. A Metrohm Autolab electrochemical station and a CH Instruments Electrochemical Workstation 660C were used for all electrochemical measurements.

2.2.5. Detection of Metal Leaching

A Perkin-Elmer Nexion 2000 Inductively-Coupled Plasma Mass Spectrometer was used to detect concentrations of bismuth and vanadium in pre- and post-photoelectrolysis conditions. A rotary evaporator was used to remove volatile organics (acetonitrile) yielding a crude. Washes with Millipore water (3 × 2 mL) were used to extract the metals in the crude to create stock samples from which serial dilutions were prepared for analysis on the ICP-MS. Diluted samples were referenced to a Pt external standard and concentrations of Bi and V were determined via calibration curves containing equimolar concentrations of Bi and V from independent 1000 μg mL^{-1} sources (GFS Chemicals and Fisher respectively).

2.2.6. Density Functional Theory

Ground-state energy calculations were performed with B3LYP functionals with the 6-31G* basis set in polar solvent using Spartan'18 software, Wavefunction, Inc. Irvine CA.[21]

2.3. Results

$BiVO_4$ electrodes were prepared by a BiOI electrodeposition on FTO followed by thermal conversion to $BiVO_4$ using a method reported by the Choi group.[22] Diffuse reflectance spectroscopy (Figure A.1) was performed to identify absorption characteristics—using the Kubelka Munk transformation—of the as made films; Tauc analysis of the transformed absorption data was applied to determine the indirect band gap, which yielded 2.43 eV. $BiVO_4$ films were further characterized with powder X-ray diffraction, displaying only peaks for the desired monoclinic phase (Figure A.2).

To determine appropriate conditions for photoelectrochemistry on $BiVO_4$, its native activity for direct $PhCH_2OH$ oxidation was assessed using linear sweep voltammetry (LSV). Figure 2.1 shows LSV traces collected by sweeping from open-circuit potential (−0.8 V to −0.2 V) to +1 V vs ferrocenium/ferrocene ($Fc^{+/0}$) in MeCN solutions of varying $PhCH_2OH$ concentration. The

LSV data show that as the concentration of $PhCH_2OH$ increases, the photocurrent density also increases. A control LSV experiment in the dark (dashed trace) supports that this current is indeed derived from photogenerated charge carriers in $BiVO_4$. To confirm that this anodic current corresponds to $PhCH_2OH$ oxidation, we performed controlled potential coulometry (CPC) at 0.75 V vs $Fc^{+/0}$ for 4 hours while stirring the solution to generate enough product for GC-FID analysis. A two-compartment cell with a 1 μm porous glass frit was used to separate the $BiVO_4$ working electrode and reference electrode (Ag wire with Vycor frit) from the Pt coil auxiliary electrode. Figure A.3 shows that during the reaction, the current density steadily decreases from 4 mA cm^{-2} to 1 mA cm^{-2}, indicating that $BiVO_4$ is unstable during catalysis (*vide infra*).

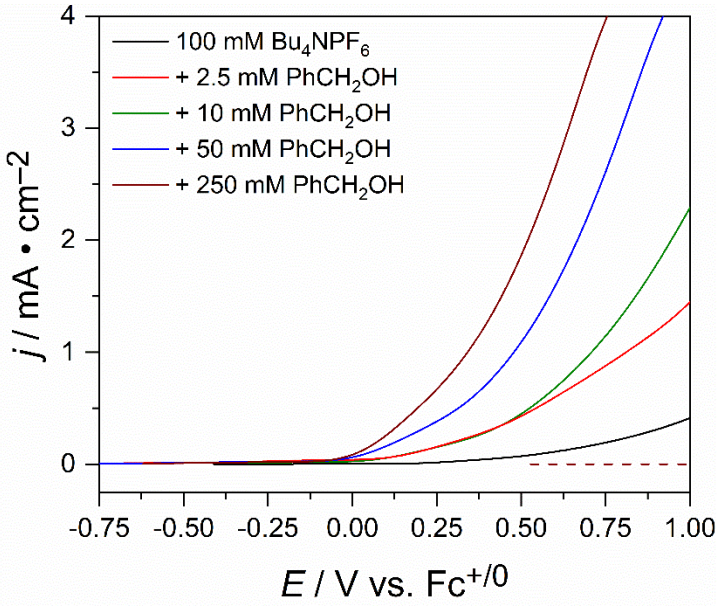

Figure 2.1. LSV traces on $BiVO_4$ photoelectrodes (1.3 cm^2) collected in acetonitrile solutions containing varying concentrations of $PhCH_2OH$ with 100 mM Bu_4NPF_6 supporting electrolyte. The scan rate is 10 mV s^{-1}. Dashed trace indicates a dark scan.

Nevertheless, PhCHO forms with 88 ± 3 % FE, revealing the native ability for direct $PhCH_2OH$ oxidation on $BiVO_4$. With the baseline established, any improvements afforded by indirect oxidation through NO_3• generation could be resolved. Cooperativity between nitrate and $BiVO_4$ was preliminarily detected by LSV. Figure 2.2 shows that adding 100 mM Bu_4NNO_3 shifts the photocurrent onset potential negatively by 500 mV. CPC was used to track PhCHO formation in these solutions after a constant 0 V vs $Fc^{+/0}$ potential was applied (Figure A.4); direct alcohol oxidation without Bu_4NNO_3 is exceedingly slow under these conditions (j_{ph} < 0.05 mA cm^{-2}). With Bu_4NNO_3, the corresponding GC-FID product analysis shows high selectivity for PhCHO (FE = 91 ± 11%) along with a substantial increase in the amount of PhCHO produced. Although

having nitrate in solution leads to faster rates of $PhCH_2OH$ oxidation, the photocurrent density steadily decreases over the course of the CPC experiment. Inductively coupled plasma mass spectrometry (ICP-MS) was used to track $BiVO_4$ dissolution. Table 2.1 shows metal-ion leaching data for several CPC experiments. For the same quantity of charge passed, when more positive potentials were applied—to effect direct $PhCH_2OH$ oxidation—higher concentrations of bismuth and vanadium leach into solution.

When indirect $PhCH_2OH$ oxidation occurs, enabled by the presence of nitrate, the concentration

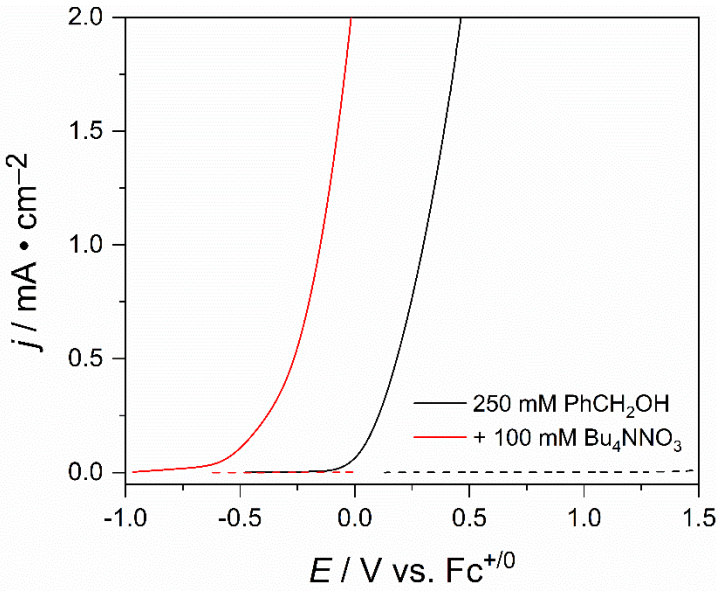

Figure 2.2. Linear sweep voltammograms performed on $BiVO_4$ at 10 mV s^{-1} in acetonitrile solutions containing 100 mM Bu_4NPF_6 supporting electrolyte with 250 mM $PhCH_2OH$. The effect of adding 100 mM Bu_4NNO_3 (red trace) is shown. Dashed traces are the dark scans.

of dissolved metal ions is lower. Illumination-only and bias-only control reactions demonstrate that metal-ion dissolution is linked to catalysis rather than any inherent chemical incompatibility between the supporting electrolyte solution and $BiVO_4$.

Table 2.1. Changes in metal-ion solution concentration after CPC experiments.

CPC Reaction Conditions	Δ[Bi] / μM	Δ[V] / μM
448 nm illumination +0.75 V vs. $Fc^{+/0}$, 4 h without Bu_4NNO_3	13.8	14.2
448 nm illumination +0 V vs. $Fc^{+/0}$, 20 h with Bu_4NNO_3	1.1	2.3

448 nm illumination only, 72 h	0.7	1.2
0.75 V $Fc^{+/0}$ applied bias only, 4 h	0	0

Top-down scanning electron microscopy (SEM) images in Figure 2.3 link the metal-ion leaching to surface roughening on $BiVO_4$ films. Films show significant roughening for direct $PhCH_2OH$ oxidation by valence-band holes, where large positive bias is required without nitrate. The morphology change on $BiVO_4$ is dampened when a less positive bias is employed to oxidize $PhCH_2OH$ indirectly, enabled by the NO_3^-/NO_3• couple. These SEM images compare changes in

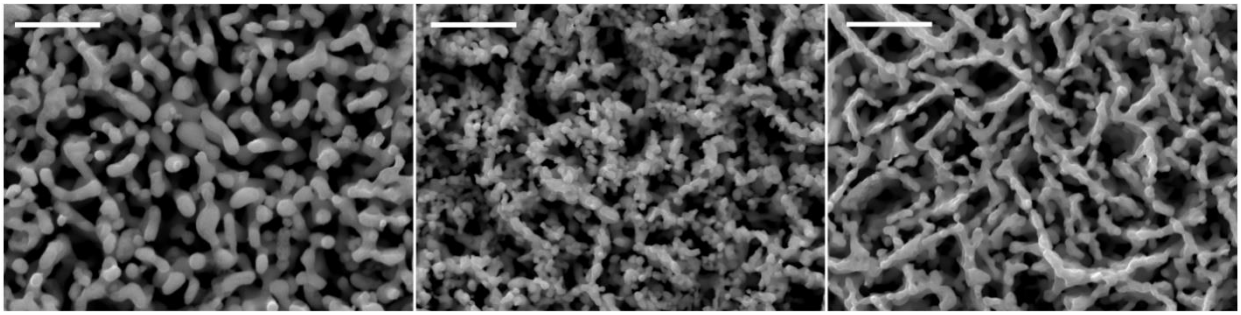

Figure 2.3. SEM images of a synthesized $BiVO_4$ film (left); film after direct $PhCH_2OH$ oxidation (middle); and after indirect $PhCH_2OH$ oxidation enabled by the NO_3^-/NO_3• couple (right). The scale bar represents 1 μm.

$BiVO_4$ for the same quantity of charge passed. XPS analysis reveals a shift in the Bi $4f_{7/2}$ and V $2p_{3/2}$ doublet peaks of prepared $BiVO_4$ (158.9 eV and 516.5 eV respectively) to higher binding energies after CPC (159.2 eV and 516.7 eV), indicating a change in surface composition (Figure A.5). Although $BiVO_4$ photoanodes show an apparent compositional sensitivity to applied bias, other factors may explain this trend. Alcohol oxidation requires deprotonation, and, like many metal oxides, $BiVO_4$ shows sensitivity to high proton activity.[23] We postulate that NO_3^-, a weak base in acetonitrile (pK_a ~9),[24] may reduce the extent of photocorrosion.

To understand how added nitrate participates in this indirect cooperative process, we studied the photocurrent dependence on [Bu_4NNO_3] concentration through LSV in MeCN. Figure 2.4a displays a plateau current that increases in magnitude and shifts to more positive potentials with increasing nitrate concentration. The plateau corresponds to NO_3^- oxidation, and the concentration-dependent plateau potential shift results from the quasi-reversibility in the $NO_3^-/NO_3\bullet$ couple. Next, we introduced varying quantities of $PhCH_2OH$ to solutions containing 10 mM Bu_4NNO_3. Figure 2.4b shows that the peak current for NO_3^- oxidation is constant (~1.7 mA cm^{-2}), but the plateau onset potential shifts to more negative potentials as the $PhCH_2OH$

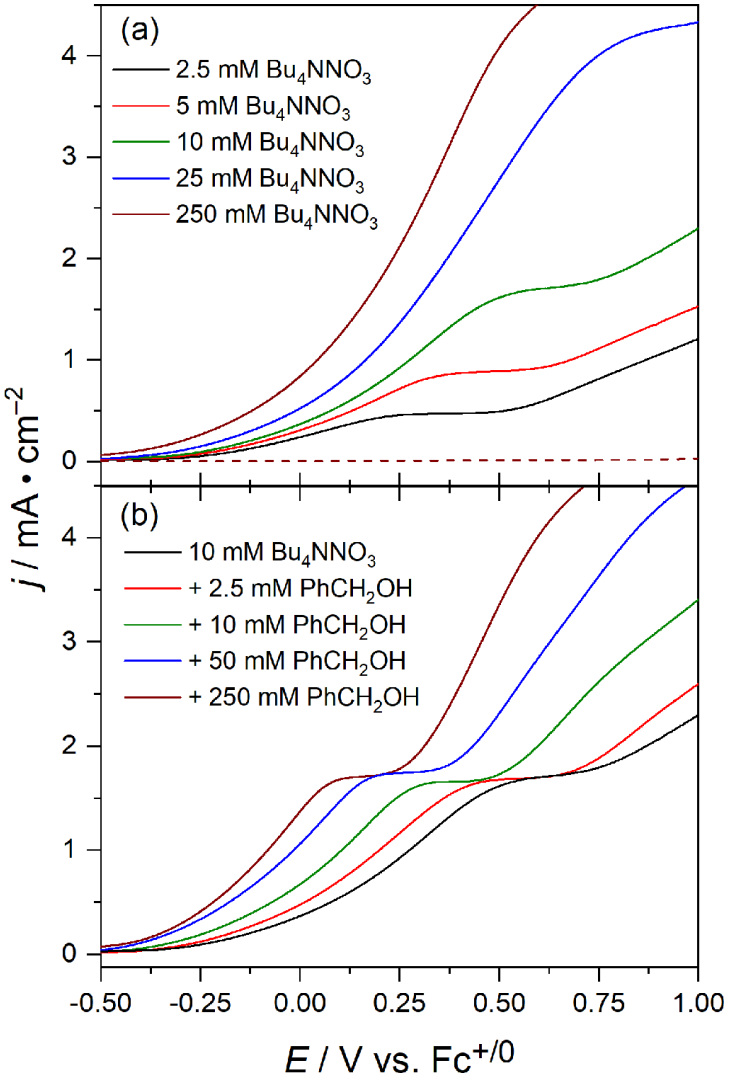

Figure 2.4. LSV traces collected on $BiVO_4$ in MeCN solutions containing 100 mM Bu_4NPF_6 supporting electrolyte with varying concentrations of Bu_4NNO_3. Dashed lines represent the dark scans (a). LSV traces of varying $PhCH_2OH$ concentrations in a 10 mM Bu_4NNO_3 solution with supporting electrolyte (b). All LSVs were collected at 10 mV s^{-1}.

concentration increases. The observation of a plateau in the photocurrent density reveals that indirect $PhCH_2OH$ oxidation does not regenerate NO_3^-.Instead, NO_3• reacts irreversibly (i. e. stoichiometrically) through an EC_i mechanism. The expected regeneration of NO_3^- through a catalytic EC′ mechanism does not occur. The photocurrent dependence on the scan rate in Figure 2.5 also supports an EC_i mechanism; the peak current density depends on the square root of scan rate ($j_p \alpha \nu^{0.5}$), as predicted by the Randles-Sevcik equation.[25] The anodic peaks observed for fast scan rates ($\nu \geq 50$ mV s^{-1}) correspond to depletion of NO_3^- at the photoanode surface that would not occur under catalytic regeneration.[26] The shifting peak potential with increasing scan rate is also characteristic of irreversible NO_3^- oxidation.

Along with a stoichiometric consumption of NO_3^-, we observe a shift in the onset potential for NO_3^- oxidation when $PhCH_2OH$ is present. The facilitation of NO_3^- oxidation by $PhCH_2OH$

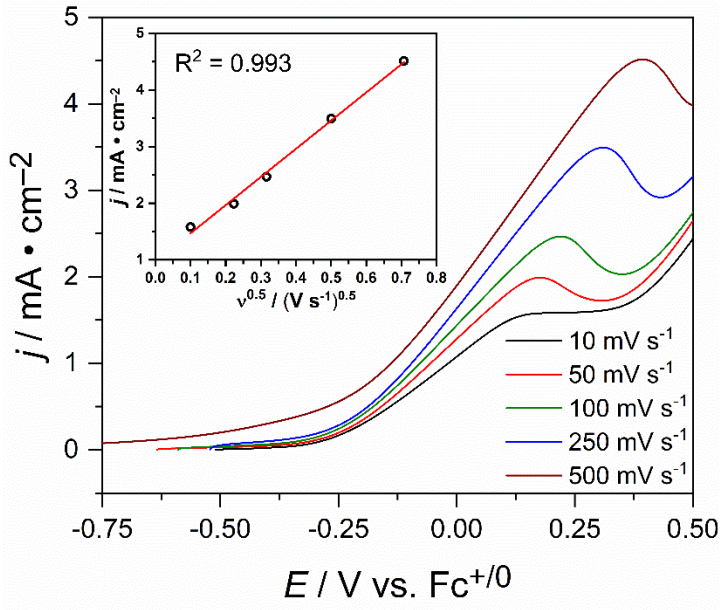

Figure 2.5. Scan-rate-dependent LSV traces on $BiVO_4$ in MeCN solution containing 10 mM Bu_4NNO_3 and 250 mM $PhCH_2OH$ with Bu_4NPF_6 supporting electrolyte. The inset shows the linear fit for peak photocurrent density as a function of the square root of scan rate.

in the LSV traces is linked to faster rates of $PhCH_2OH$ oxidation (forming PhCHO) confirmed by CPC experiments. The plot in Figure 2.6 shows a slope of ~200 mV per order of magnitude

increase in $PhCH_2OH$ concentration. For a reversible redox couple, the Nernst equation predicts a 59.1 mV shift per order of magnitude increase in substrate concentration.[25] The quasi-reversible

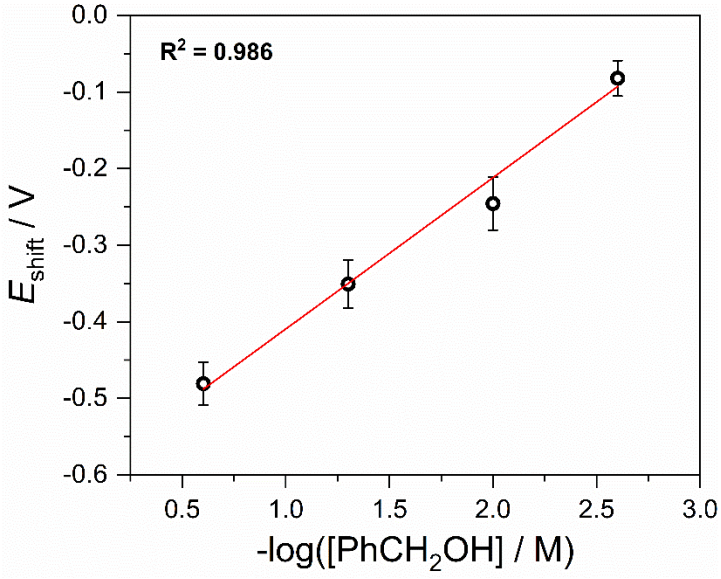

Figure 2.6. Shift in potential corresponding to the center of the plateau for NO_3^- oxidation (j = 1.6 mA cm^{-2} − 1.7 mA cm^{-2}) as a function of −log[$PhCH_2OH$] in 10 mM Bu_4NNO_3 solution.

nature of the NO_3^-/NO_3• couple results in a much larger equilibrium potential shift due to a substrate-driven consumption pathway for NO_3•. Reduced photocorrosion on $BiVO_4$ and irreversible NO_3^- oxidation (Figure 2.4b) point toward a reaction between NO_3• and $PhCH_2OH$ proceeding through HAT to yield HNO_3. Consequently, the concentration of NO_3• at the $BiVO_4$ photoelectrode surface decreases and this perturbation of equilibrium concentrations for NO_3^- and NO_3• creates a driving force to reestablish equilibrium (Le Chatelier's principle); this driving force is measured as the shift in Figure 2.6.

To investigate irreversible nitrate consumption coupled to alcohol oxidation further, isotopic rate studies were performed. Figure 2.7 shows nearly identical LSV responses when using (α,α-d_2) deuterated $PhCD_2OH$ under the same conditions, revealing no 1° kinetic isotope effect (KIE).

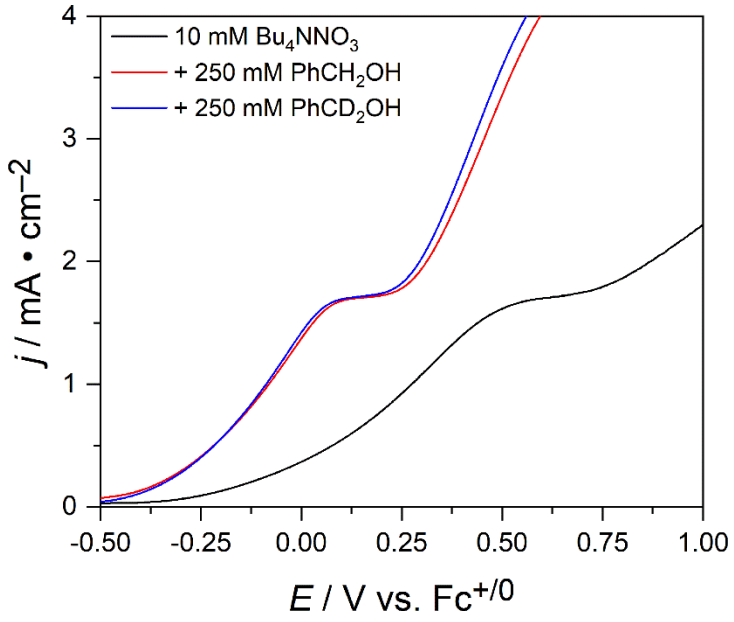

Figure 2.7. Illuminated LSV traces comparing 250 mM $PhCH_2OH$ oxidation (red) and 250 mM $PhCD_2OH$ oxidation (blue) with 10 mM Bu_4NNO_3 in MeCN containing 100 mM Bu_4NPF_6 supporting electrolyte. The scan rate is 10 mV s^{-1}.

This result indicates that the α-hydrogen does not react in the rate-determining step. However, this observation does not rule out a stepwise process involving rate-determining NO_3^- oxidation followed by a fast HAT step consuming NO_3• and yielding HNO_3. In acetonitrile, the weak electrolyte HNO_3 is inert toward indirect $PhCH_2OH$ oxidation on $BiVO_4$ photoelectrodes (Figure A.6 and Figure A.7).

To further probe the reaction between NO_3• and alcohol substrate in solution, we compared the LSV traces within the series of α-methylated benzyl alcohol derivatives. The green trace of Figure 2.8 shows that the secondary alcohol, 1-phenylethanol results in a diminished shift for the NO_3^-/NO_3• couple.

Steric hindrance about the benzylic carbon appears to slow down reactivity between NO_3• and alcohol substrate. Continuing with the series, one would expect that NO_3• reacting through HAT would indeed require an α-hydrogen. Not surprisingly, when the tertiary alcohol, 2-phenyl-2-propanol is introduced, a reversion to substrate-free nitrate behavior is observed (Figure 2.8, blue

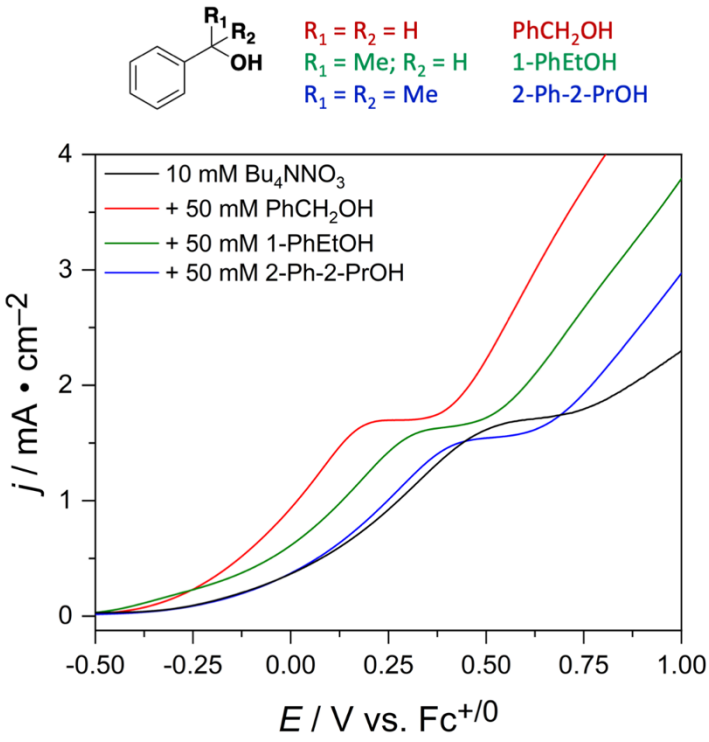

Figure 2.8. LSV traces comparing benzyl alcohol and its derivatives. Solutions contain 50 mM alcohol, 10 mM Bu_4NNO_3 and 100 mM Bu_4NPF_6 supporting electrolyte in MeCN. The scan rate is 10 mV s^{-1}.

trace). The potential at which the photocurrent begins to plateau progressively shifts approximately 100 mV to more positive values as the benzylic carbon becomes increasingly methylated: ~0.20 V, 0.30 V, 0.40 V vs. $Fc^{+/0}$ for BnOH, 1-PhEtOH, and 2-Ph-2-PrOH respectively. This shift highlights the role of the α-hydrogen in this EC_i mechanism.[15–17,19]

2.4. Discussion

Figure 2.9 presents the mechanistic picture that unfolds from the experimental observations. Herein, we demonstrate the native activity for direct $PhCH_2OH$ oxidation on $BiVO_4$ and show the substantial rate improvement afforded by coupling to NO_3^- oxidation. Optimized conditions (Figure A.8) show high faradaic efficiency—99 ± 9%—for benzaldehyde product through indirect electron transfer. Importantly, photoelectrochemically oxidizing NO_3^- on $BiVO_4$ in the first mechanistic step enables indirect alcohol oxidation at potentials where direct alcohol oxidation does not occur. NO_3^- oxidation shows quasi-reversible kinetics, evidenced by a shifting peak current density (Figure 2.5) and a non-Nernstian 200 mV shift in the $NO_3^-/NO_3\bullet$ equilibrium potential per order of magnitude increase in $PhCH_2OH$ concentration (Figure 2.6). An irreversible chemical step perturbs the equilibrium concentration of $NO_3^-/NO_3\bullet$ due to a consumption pathway for $NO_3\bullet$ that affords the desired PhCHO product.

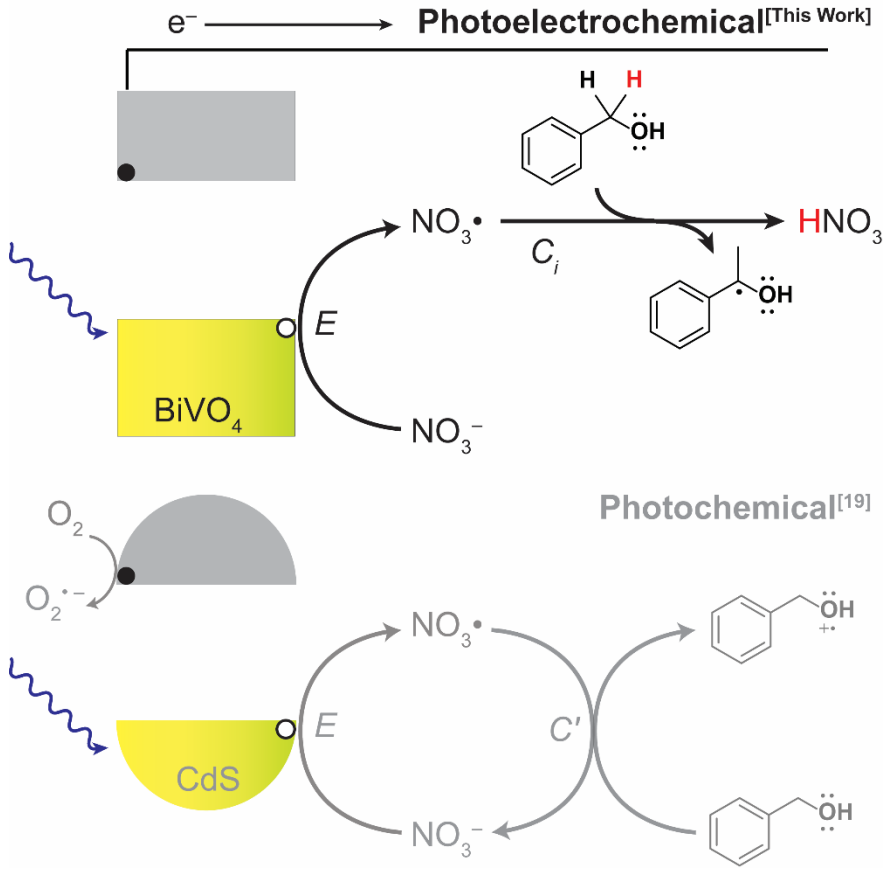

Figure 2.9. Observed EC_i mechanism for indirect $PhCH_2OH$ oxidation through $NO_3\bullet$ on $BiVO_4$ photoelectrodes (top). Alternate EC′ mechanism observed on CdS nanowires (bottom).

Previous work in our lab demonstrates that NO_3^- acts as a redox mediator (i. e. it is regenerated) in photocatalytic $PhCH_2OH$ oxidation on CdS nanowires. Photoelectrochemically, NO_3^- is not regenerated, representing an EC_i mechanism. The difference in NO_3^- behavior in the two acetonitrile systems is rationalized in the context of the full light-driven redox cycle. On CdS nanowires, electrons are photoexcited to the conduction band, where they carry out the oxygen reduction reaction. If that reaction is carried out under inert N_2 atmosphere, $PhCH_2OH$ oxidation is slow, and NO_3^- is consumed (likely by its reduction). Reduced oxygen species, such as superoxide (O_2^-), that are co-located with either HNO_3 or a carbon-centered radical intermediate can deprotonate HNO_3 after HAT or avoid HNO_3 formation altogether, rendering NO_3^- catalytic. In photoelectrochemistry, these reactions occur in separate compartments such that NO_3^- oxidation on a $BiVO_4$ working electrode is separated – by several centimeters – from the reduction reactions on the platinum auxiliary electrode. Accordingly, carrying out the photoelectrochemical reaction on $BiVO_4$ anaerobically (under N_2) shows no discernable difference in the voltammetric response (Figure A.9), demonstrating that reduced oxygen species such as O_2^- do not act as a base is under these conditions. Rather, nitrate in the working compartment is the only local base.

Neither CdS nanowire photocatalysis nor $BiVO_4$ photoelectrochemistry show a 1° KIE for $PhCH_2OH/PhCD_2OH$ oxidation. On $BiVO_4$, NO_3^- consumption and lack of KIE point to rate-determining NO_3^- oxidation with a fast HAT step. The voltammetric response of a series the para-substituted benzyl alcohol derivatives, 4-chlorobenzyl alcohol and 4-tert-butylbenzyl alcohol was measured (Figure A.10), and the zero slope in the data reveal no buildup of charge in the transition state. While electronic factors have a negligible influence on the rate of indirect alcohol oxidation using photoelectrochemically generated NO_3•, the functionality about the benzylic position

(Figure 2.8) has substantial impact. Density functional theory also helps distinguish between HAT and single-electron transfer (SET) mechanisms. Figure 2.9 shows the frontier orbitals energies and projections of the HOMO of $PhCH_2OH$ and the derivatives described throughout the manuscript. Of note, the HOMO of benzyl alcohol has aromatic π* and oxygen 2p lone-pair character with an energy −6.6 eV. As the number of methyl groups increases, the HOMO adds slight C−C σ bonding character and the energy *increases slightly* or is unchanged: −6.5 eV for 1-PhEtOH and −6.6 eV

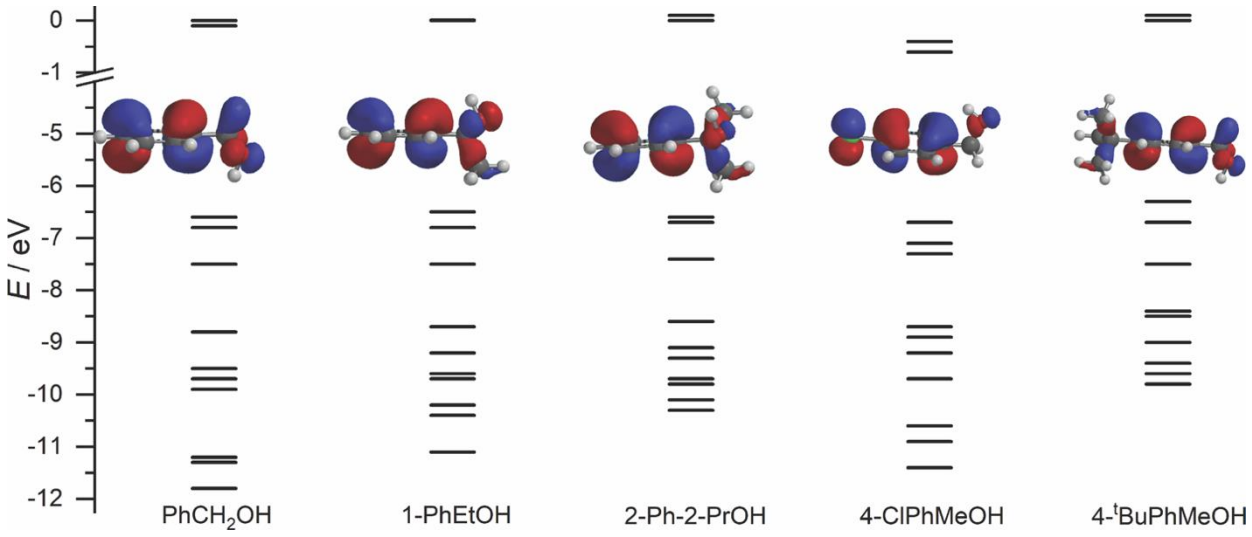

Figure 2.10. DFT calculations (B3LYP functionals, 6–31G* basis set) of the frontier orbitals of benzyl alcohol and its derivatives; the projection of the HOMO illustrated.

for 2-Ph-2-PrOH. Taking the HOMO energy as an approximation for ionization energy by Koopman's theorem[27] and adding the dielectric continuum to account for solvation energies, we would predict that if SET were the operative mechanism, then the potential at which the anodic current plateaus would be nearly constant (if not show a slight shift to more *negative* values). The observed shift to more positive potentials suggests a HAT mechanism that forms a carbon-centered radical opposed to SET that forms an oxygen-centered radical. Moreover, the HOMO energies for the para-substituted derivatives remain similar, −6.7 eV for 4-chlorobenzyl alcohol and −6.3 eV for 4-*tert*-butylphenyl methanol.

For reversible redox couples, the Nernst equation predicts a 59.1 mV equilibrium potential shift per order of magnitude increase in substrate concentration. This theoretical treatment was demonstrated empirically in a recent report describing a $TEMPO^+$–N_3^- system.[28] TEMPO radical oxidation was facilitated in the presence of N_3^- by forming a stable charge-transfer complex, which showed a 62 mV shift per order of magnitude increase in [N_3^-]. In our work, NO_3^- is not

regenerable on $BiVO_4$ and the 200-mV potential shift slope (Figure 2.6) is non-Nernstian due to the quasi-reversibility of the $NO_3^-/NO_3\bullet$ couple as well as an irreversible chemical step (EC_i) where nitrate radical is consumed; introducing a benzyl alcohol-based consumption pathway vastly improves the electrochemical kinetics for NO_3^- oxidation.

Another key difference between the two acetonitrile systems is the importance of nitrate's counterion in the salt. We find Bu_4NNO_3 to be a viable source of nitrate for indirect alcohol oxidation on $BiVO_4$. However, Bu_4NNO_3 does not mediate photocatalytic $PhCH_2OH$ oxidation on CdS nanowires. There, a hard metal cation such as Li^+, Ca^{2+}, or Mn^{2+} is required, and metal-cation coordination with nitrate is observed by both UV-Vis and FTIR spectroscopy. Absorption features for NO_3^- ($n \rightarrow \pi^*$) show a blue shift in acetonitrile with metal cations present; this perturbation in electronic structure suggests an altered redox potential for the $NO_3^-/NO_3\bullet$ couple. Therefore, the lack of general activity in acetonitrile using Bu_4NNO_3 supports misalignment between the redox potential $E(NO_3^-/NO_3\bullet)$ and the valence band edge (E_{VB}) of CdS. A similar thermodynamic mismatch was discovered recently between TEMPO and $BiVO_4$ photoanodes in water.[29] There, TEMPO was shown to act as a recombination center, hindering electron transfer from $BiVO_4$ to solution; tuning the surface-mediator interaction with an interfacial cobalt phosphate layer enabled TEMPO mediation. In that example, a heterogeneous treatment was used to overcome redox potential-band edge misalignment, and we postulate that metal cations in solution address the issue on CdS.

Recently, a report detailing indirect $PhCH_2OH$ oxidation in aqueous electrolyte showed selective generation of PhCHO on $BiVO_4$ photoanodes decorated with a layered double hydroxide (LDH) surface electrocatalyst.[30] In that system, indirect alcohol oxidation was achieved through a surface-bound hydroxyl radical intermediate generated from water oxidation on the cobalt-based LDH. Comparison of this system with our work reveals key similarities, namely the formation of a carbon-centered benzyl alcohol radical and stoichiometric consumption of a radical intermediate ($\bullet OH/NO_3\bullet$). While both systems function through an EC_i mechanism, the consumption of $NO_3\bullet$ through HAT is responsible for forming the benzyl alcohol radical, while the LDH@$BiVO_4$ system forms the benzyl alcohol radical through an activation step *before* •OH reacts. Nevertheless, both systems show accelerated rates for $PhCH_2OH$ oxidation upon introducing indirect pathways characterized as "radical relays." Exploring the scope of radical relays and their role in catalyzing alcohol oxidation reactions is the subject of ongoing investigation in our lab.

2.5. Conclusions

We show that nitrate anion effects indirect photoelectrochemical benzyl alcohol oxidation on bismuth(III) vanadate in acetonitrile solvent. The applied potential required to generate benzaldehyde was reduced by ∼500 mV, while retaining > 90 % high faradaic efficiency. The coupled chemical step of benzyl alcohol substrate oxidation leads to faster electrochemical nitrate anion oxidation; the shift is 200 mV per order of magnitude increase in alcohol substrate concentration. The chemical step is likely rapid nitrate radical consumption through hydrogen-atom transfer with benzyl alcohol to yield nitric acid. Deuterating the alpha positions (benzyl alcohol α,α-d_2) shows no change in reaction rate, supporting that nitrate anion oxidation is rate-determining and distinct. Lower applied potentials to generate benzaldehyde product and diminished bismuth vanadate photocorrosion are significant benefits granted with nitrate anion reactant.

References

[1] Li, H.; Qin, F.; Yang, Z.; Cui, X.; Wang, J.; Zhang, L. New Reaction Pathway Induced by Plasmon for Selective Benzyl Alcohol Oxidation on BiOCl Possessing Oxygen Vacancies. *J. Am. Chem. Soc.* **2017**, *139*, 3513– 3521.

[2] Sayama, K. Production of High-Value-Added Chemicals on Oxide Semiconductor Photoanodes under Visible Light for Solar Chemical-Conversion Processes. *ACS Energy Lett*. **2018**, *3*, 1093–1101.

[3] Dao, R.; Zhao, C.; Yao, J.; Li, H. Distinguishing ionic and radical mechanisms of hydroxylamine mediated electrocatalytic alcohol oxidation using NO–H bond dissociation energies. *Phys. Chem. Chem. Phys.* **2018**, *20*, 28249–28256.

[4] Peng, H.-J.; Zhang, G.; Chen, X.; Zhang, Z.-W.; Xu, W.-T.; Huang, J.-Q.; Zhang, Q. Enhanced Electrochemical Kinetics on Conductive Polar Mediators for Lithium–Sulfer Batteries. *Angew. Chem. Int. Ed.* **2016**, *55*, 12990–12995.

[5] Chen, Y.; Freunberger, S. A.; Peng, Z.; Fontaine, O.; Bruce, P. G. Charging a Li–O_2 battery using a redox mediator. *Nat. Chem*. **2013**, *5*, 489–494.

[6] Luo, Z.; Geletii, Y. V.; Hillesheim, D. A.; Wang, Y.; Hill, C. L. Mechanistic Studies of O_2-Based Sulfoxidations Catalyzed by NO_x/Br Systems. *ACS Catal*. **2011**, *1*, 1364–1370.

[7] Badalyan, A.; Stahl, S. S. Cooperative electrocatalytic alcohol oxidation with electron-proton-transfer mediators. *Nature* **2016**, *535*, 406–410.

[8] Cha, H. G.; Choi, K.-S. Combined biomass valorization and hydrogen production in a photoelectrochemical cell. *Nat. Chem*. **2015**, *7*, 328–333.

[9] Li, T.; Kasahara, T.; He, J.; Dettelbach, K. E.; Sammis, G. M.; Berlinguette, C. P. Photoelectrochemical oxidation of organic substrates in organic media. *Nat. Commun.* **2017**, *8*, 390.

[10] Rahimi, A.; Azaripa, A.; Kim, H.; Ralph, J.; Stahl, S. S. Chemoselective Metal-Free Aerobic Alcohol Oxidation in Lignin. *K. Am. Chem. Soc*. **2013**, *135*, 6415–6418.

[11] de Nooy, A. J.; Besemer, A. C.; van Bekkem, H. Highly selective nitroxyl radical-mediated oxidation of primary alcohol groups in water-soluble glucans. *Carbohydr. Res.* **1995**, *269*, 89–98.

[12] Lauber, M. B.; Stahl, S. S. Efficient Aerobic Oxidation of Secondary Alcohols at Ambient Temperature with an ABNO/NO_x Catalyst System. *ACS Catal*. **2013**, *3*, 2612–2616.

[13] de Nooy, A. J.; Besemer, A. C.; van Bekkem, H. Selective oxidation of primary alcohols mediated by nitroxyl radical in aqueous solution. Kinetics and mechanism. *Tetrahedron* **1995**, *51*, 8023–8032.

[14] Taitt, B. J.; Bender, M. T.; Choi, K.-S. Impacts of the Regeneration Pathways of the Oxoammonium Cation on Electrochemical Nitroxyl Radical-Mediated Alcohol Oxidation. *ACS Catal*. **2020**, *10*, 265–275.

[15] Leonard, J. E.; Scholl, P. C.; Steckel, T. P.; Lentsch, S. E.; Van De Mark, M. R. Electrochemical oxidation of alcohols: part II preparative anodic oxidation of secondary alkanols employing lithium nitrate. *Tetrahedron Lett.* **1980**, *21*, 4695–4698.

[16] Christopher, C.; Lawrence, S.; Kulandainathan, M. A.; Kulangiappar, K.; Raja, M. E.; Xavier, N.; Raja, S. Electrochemical selective oxidation of aromatic alcohols with sodium nitrate mediator in biphasic medium at ambient temperature. *Tetrahedron Lett.* **2012**, *53*, 2802–2804.

[17] Christopher, C.; Lawrence, S.; Bosco, A. J.; Xavier, N.; Raja, S. Selective oxidation of benzyl alcohol by two phase electrolysis using nitrate as a mediator. *Catal. Sci. Technol.* **2012**, *2*, 824–827.

[18] Hering, T.; Slanina, T.; Hancock, A.; Wille, U.; König, B. Visible light photooxidation of nitrate: the dawn of a nocturnal radical. *Chem. Commun.* **2015**, *51*, 6568–6571.

[19] DiMeglio, J. L.; Breuhaus-Alvarez, A. G.; Li, S.; Bartlett, B. M. Nitrate-Mediated Alcohol Oxidation on Cadmium Sulfide Photocatalysts. *ACS Catal*. **2019**, *9*, 5732–5741.

[20] Sivula, K.; van de Krol, R. Semiconducting materials for photoelectrochemical energy conversion. *Nat. Rev. Mater.* **2016**, *1*, 15010.

[21] Shao, Y.; Molnar, L. F.; Jung, Y.; Kussmann, J.; Ochsenfeld, C.; Brown, S. T.; Gilbert, A. T. B.; Slipchenko, L. V.; Levchenko, S. V.; O'Neill, D. P.; DiStasio Jr, R. A.; Lochan, R. C.; Wang, T.; Beran, G. J. O.; Besley, N. A.; Herbert, J. M.; Lin, C. Y.; Voorhis, T. V.; Chien, S. H.; Sodt, A.; Steele, R. P.; Rassolov, V. A.; Maslen, P. E.; Korambath, P. P.; Adamson, R. D.; Austin, B.; Baker, J.; Byrd, E. F. C.; Dachsel, H.; Doerksen, R. J.; Dreuw, A.; Dunietz, B. D.; Dutoi, A. D.; Furlani, T. R.; Gwaltney, S. R.; Heyden, A.; Hirata, S.; Hsu, C.-P.; Kedziora, G.; Khalliulin, R. Z.; Klunzinger, P.; Lee, A. M.; Lee, M. S.; Liang, W.; Lotan, I.; Nair, N.; Peters, B.; Proynov, E. I.; Pieniazek, P. A.; Rhee, Y. M.; Ritchie, J.; Rosta, E.; Sherrill, C. D.; Simmonett, A. C.; Subotnik, J. E.; Woodcock III, H. L.; Zhang, W.; Bell, A. T.; Chakraborty, A. K.; Chipman, D. M.; Keil, F. J.; Warshel, A.; Hehre, W. J.; Shaefer III, H. F.; Kong, J.; Krylov, A. I.; Gill, P. M. W.; Head-Gordon, M. Advances in methods and algorithms in a modern quantum chemistry program package. *Phys. Chem. Chem. Phys.* **2006**, *8*, 3172.

[22] Kim, T. W.; Choi, K.-S. Nanoporous $BiVO_4$ Photoanodes with Dual-Layer Oxygen Evolution Catalysts for Solar Water Splitting. *Science*, **2014**, *343*, 990–994.

[23] Han, L.; Tang, P.; Reyes-Carmona, Á.; Rodríguez-García, B.; Torréns, M.; Morante, J. R.; Arbiol, J.; Galan-Mascaros, J. R. Enhanced Activity and Acid pH Stability of Prussian Blue-type Oxygen Evolution Electrocatalysts Processed by Chemical Etching. *J. Am. Chem. Soc*. **2016**, *138*, 16037–16045.

[24] Eckert, F.; Leito, I.; Kaljurand, I.; Kütt, A.; Klamt, A.; Diedenhofen, M. Prediction of acidity in acetonitrile solution with COSMO-RS. *J. Comput. Chem.* **2009**, *30*, 799–810.

[25] Elgrishi, N.; Rountree, K. J.; McCarthy, B. D.; Rountree, E. S.; Eisenhart, T. T.; Dempsey, J. L. A Practical Beginner's Guide to Cyclic Voltammetry. *J. Chem. Educ.* **2018**, *95*, 197–206.

[26] Wang, V. C.-C.; Johnson, B. A. Interpreting the Electrocatalytic Voltammetry of Homogenous Catalysts by the Foot of the Wave Analysis and Its Wider Implications. *ACS Catal*. **2019**, *9*, 7109–7123.

[27] Koopmans, T. *Physica* **1934**, *1*, 104–113.

[28] Siu, J. C.; Sauer, G. S.; Saha, A.; Macey, R. L.; Fu, N.; Chauviré, T.; Lancaster, K. M.; Lin, S. Electrochemical Azidooxygenation of Alkenes Mediated by a TEMPO–N_3 Charge-Transfer Complex. *J. Am. Chem. Soc.* **2018**, *140*, 12511–12520.

[29] Chadderdon, D. J.; Wu, L.-P.; McGraw, Z. A.; Panthani, M.; Li, W. Heterostructured Bismuth Vanadate/Cobalt Phosphate Photoelectrodes Promote TEMPO-Mediated Oxidation of 5-Hydroxymethfurfural. *ChemElectroChem* **2019**, *6*, 3387–3392.

[30] Luo, L.; Wang, Z.-j.; Xiang, X.; Yan, D.; Ye, J. Selective Activation of Benzyl Alcohol Coupled with Photoelectrochemical Water Oxidation via a Radical Relay Strategy. *ACS Catal.* **2020**, *10*, 4906–4913.

Chapter 3

Base-Assisted Nitrate Mediation as the Mechanism of Electrochemical Benzyl Alcohol Oxidation

Portions of this chapter have been published:

DiMeglio, J. L.; Terry, B. D.; Breuhaus-Alvarez, A. G.; Bartlett, B. M. *J. Phys. Chem. C* **2021**, *125*, 8148–8154.

3.1. Introduction

Redox mediators are valuable tools used to facilitate electron-transfer reactions, thus improving reaction rates and product selectivity in a variety of catalytic transformations. This indirect process has been implemented under electrochemical control to drive aliphatic C–H functionalization,[1,2] aziridination of alkenes,[3] alcohol oxidation, and more.[4] Nitrate radical (NO_3•) serves as a homogenous oxidant in photochemical and photoelectrochemical systems for benzyl alcohol oxidation on CdS powder and $BiVO_4$ films, respectively.[5,6] From Chapter 2, unique system-dependent behavior was observed for nitrate-facilitated indirect alcohol oxidation, including tetrabutylammonium nitrate (Bu_4NNO_3) serving as a viable nitrate source on $BiVO_4$ and the behavior of the nitrate radical in solution. On $BiVO_4$ photoanodes, a unique—and unexpected—stoichiometric consumption of NO_3• was observed in its reaction with benzyl alcohol. However, indirect photochemical benzyl alcohol oxidation on CdS revealed a catalytic nitrate function in a puzzling system-dependent behavior.[7] The electrochemical work in this chapter resolves this discrepancy and provides a general framework for NO_3^-/NO_3• behavior in acetonitrile solutions.

3.2. Experimental

3.2.1. Materials and Methods

Lithium nitrate ($LiNO_3$), lithium hexafluorophosphate ($LiPF_6$), benzyl alcohol-α,α-d_2, and nitric acid (HNO_3) were purchased from Sigma Aldrich; hydrochloric acid (HCl) and acetonitrile (MeCN) were purchased from Fisher Scientific; benzyl alcohol ($PhCH_2OH$), chlorobenzene, and 2,6-lutidine were purchased from Acros Organics. All were used without further purification.

Tetrabutylammonium hexafluorophosphate (Bu_4NPF_6) was purchased from TCI and purified through hot ethanol recrystallization. To achieve 50 mM $LiNO_3$, mixtures of $LiNO_3$, MeCN, and $PhCH_2OH$ were prepared and then sonicated under heat (~50 °C) for 20 min to give a clear, colorless solution.

3.2.2. Electrochemistry

Cyclic voltammetry (CV) was conducted using either a CH Instruments Electrochemical Workstation 660C, 760E, or 1000A with a CHI Pt (area = 0.0314 cm^2) working electrode. Working electrodes were polished using a slurry of 0.05 μm alumina powder in deionized water on a MicroCloth pad. A silver wire was used as the reference electrode and inserted into a sealed glass tube with a Vycor tip and filled with the electrolyte solution. The counter electrode was either a graphite rod or a Pt wire (~0.33 cm^2), of which the latter was cleaned between experiments by dipping into aqua regia for 15 s. Unless otherwise stated, voltammetry experiments were conducted at a scan rate of 25 mV s^{-1}.

Constant potential chronoamperometry (CPC) experiments were conducted using a custom-built two-compartment glass cell separated by either an ultrafine glass frit or a Sterlitech polypropylene filter paper with a pore size of 0.1 μm (Figure B.10). The working compartment contained 12 mL of solution, and the counter compartment had 8 mL of solution. CPC utilized a Pt wire working electrode (area: ~0.35 cm^2), with a silver wire reference electrode and graphite counter as used in the voltammetry experiments. Over the course of the CPC experiment, the working compartment solution was agitated using a stir bar.

Rotating ring-disk electrode (RRDE) experiments were conducted at 30 Hz with a Pt ring and disk on a RRDE-3A version 1.2 apparatus from CH Instruments. The ring and disk were polished using a 0.05 μm Alpha Alumina slurry on a MicroCloth pad. After polishing, the ring and disk were sonicated in deionized water for 10 min. The ring and disk were then inserted into the fixture and dipped in aqua regia for 15 s, then rinsed with Millipore water. Finally, the RRDE assembly was spun at 30 Hz in acetonitrile for 5 min. The now cleaned RRDE assembly was placed into 35 mL of the analyte solution using a graphite rod counter and silver wire reference electrodes.

3.2.3. Product Analysis

Substrate and product concentrations were measured using gas chromatography-flame ionization detection (GC-FID) by periodically removing an aliquot (10 μL) from the reaction mixture and combining with a chlorobenzene standard (50 μL of a 21.6 mM standard) and

acetonitrile (940 µL). The samples were analyzed on either a Shimadzu QP-2010 GC/MS or Thermo Fisher Trace 13-10 gas chromatograph equipped with a capillary column and FID detector. During analysis, the column oven was warmed from 40 to 290 °C at a 10 °C min^{-1} ramp rate. Quantification was enabled by the integration ratio of the analyte and chlorobenzene signals in relation to an obtained calibration curve. For the FE vs time plot, ^{1}H NMR spectroscopy (d_3-acetonitrile) was used to track the formation of benzaldehyde product at 20 min time points using a known concentration of nitromethane internal standard.

3.3. Results

To demonstrate the ability of electrochemically generated NO_3• to facilitate indirect $PhCH_2OH$ oxidation, cyclic voltammograms were collected on platinum electrodes in MeCN

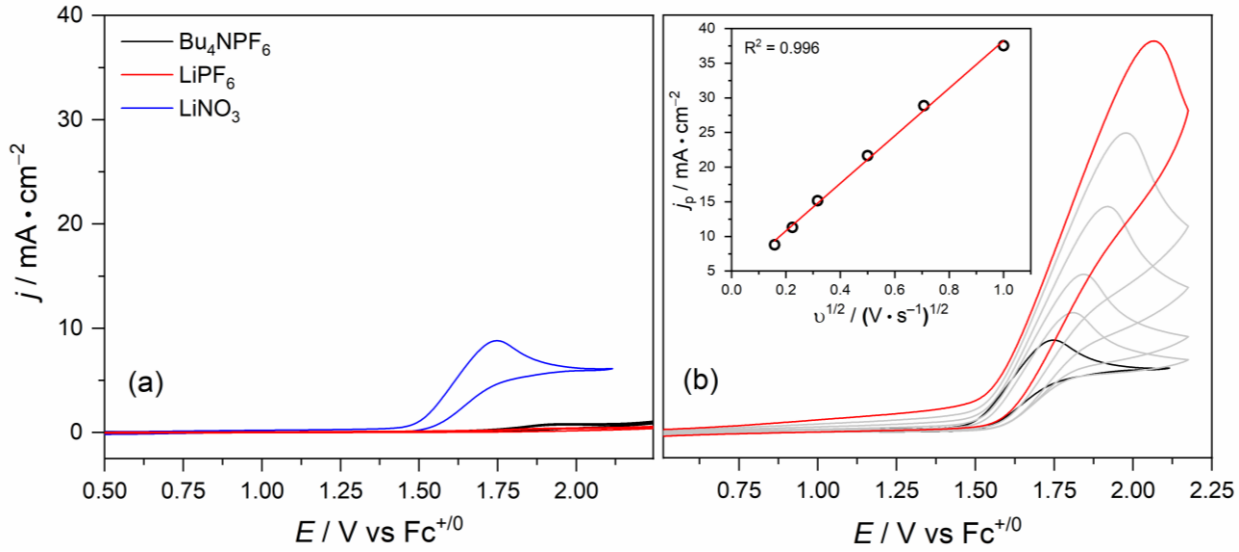

Figure 3.1. CV on Pt electrodes in MeCN solutions of 100 mM lithium hexafluorophosphate ($LiPF_6$), 100 mM Bu_4NPF_6 electrolyte, or 50 mM $LiNO_3$ at 25 mV s^{-1} (a). Scan rate-dependent CV traces on Pt in MeCN solutions containing 100 mM Bu_4NPF_6 supporting electrolyte and 50 mM $LiNO_3$ at 25, 50, 100, 250, 500, and 1000 mV s^{-1} from bottom (black) to top (red) (b).

solutions containing 50 mM lithium nitrate ($LiNO_3$) and 100 mM tetrabutylammonium hexafluorophosphate (Bu_4NPF_6) electrolyte. The cyclic voltammetry (CV) traces in Figure 3.1a highlight the anodic current achieved only when nitrate is in solution, corresponding to the one-electron oxidation of NO_3^- to NO_3•. This nitrate redox couple is irreversible, as evidenced by the lack of detectable cathodic current on reverse scans even at scan rates up to 1000 mV s^{-1} (Figure 3.1b). The peak current for NO_3^- oxidation shifts to more positive potentials with increasing scan rate due to quasireversibility and remains diffusion-controlled, noted by the linear dependence on

the square root of scan rate (inset, Figure 3.1b). The inability to detect any oxidized intermediates during the reverse scan is likely due to a solvent-based chemical reaction given the known high reactivity of NO_3• in atmospheric chemistry and the reported ability of oxidized electrolyte anions to react similarly with MeCN.[7,8]

Linear sweep voltammetry (LSV) traces were collected in the presence of $PhCH_2OH$ to explore the reactivity of electrochemically generated NO_3• in acetonitrile solutions. Surprisingly, the presence of alcohol substrate does not influence the NO_3^-/NO_3• voltammetric response (Figure 3.2a, green trace vs blue trace) suggesting that either NO_3• is incapable of oxidizing $PhCH_2OH$ or

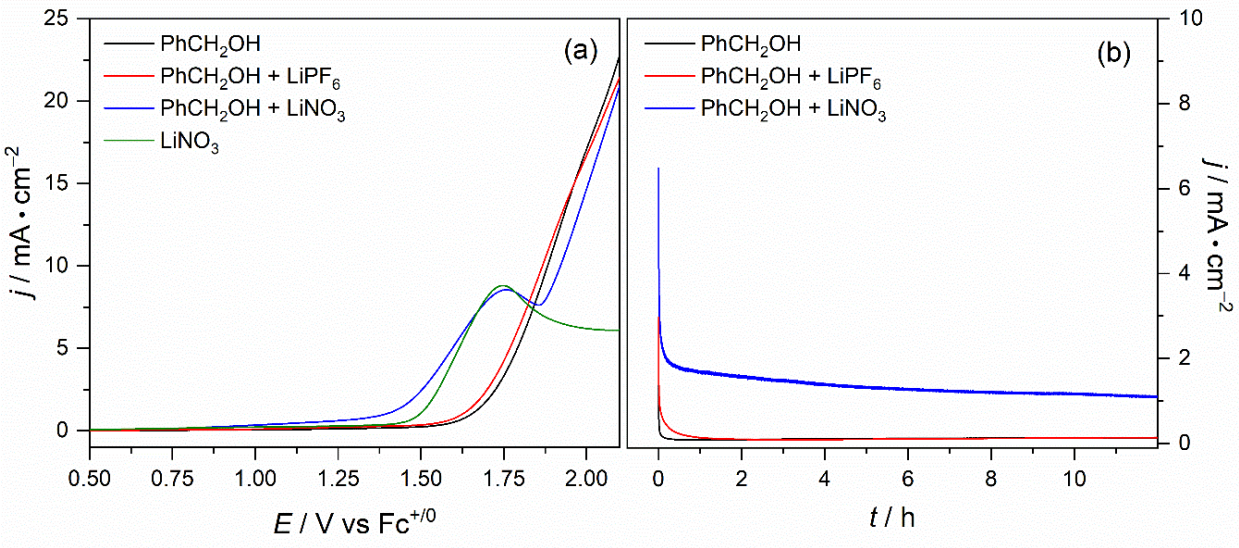

Figure 3.2. LSV recorded at 25 mV s^{-1} scan rate on Pt in MeCN solutions containing 100 mM Bu_4NPF_6 under the listed conditions, where $[PhCH_2OH]$ = 250 mM and $[LiNO_3]$ = $[LiPF_6]$ = 50 mM (a); CPC performed at 1.68 V vs $Fc^{+/0}$ under the listed conditions using a Pt wire electrode (b).

the reaction between NO_3• and $PhCH_2OH$ does not regenerate NO_3^- (noted by the preservation in peak current). To identify NO_3• reactivity toward $PhCH_2OH$ oxidation, constant potential chronoamperometry (CPC) was performed at the most positive potential before $PhCH_2OH$-only solutions show anodic current on Pt electrodes (1.68 V vs $Fc^{+/0}$). Figure 3.2b displays the current density that results from CPC in $PhCH_2OH$ solutions containing varying electrolytes while stirring to exclude mass transport limitations in the measured current. Without a nitrate salt, current densities < 0.3 mA cm^{-2} are observed, as predicted by LSV traces in Figure 3.2a. With a nitrate salt ($LiNO_3$), current densities of ~1.5 mA cm^{-2} result (additional trials are provided in Figure B.1. Product analysis by gas chromatography-flame ionization detection (GC-FID) shows benzaldehyde (PhCHO) production with 80 ± 16% FE. This result supports that the electrochemically generated NO_3• can facilitate $PhCH_2OH$ oxidation.

The irreversible NO_3^- oxidation involved in indirect $PhCH_2OH$ oxidation mirrors the photoelectrochemical example on $BiVO_4$ films but differs from the mediation behavior observed photochemically on CdS nanowires. The presence of lithium cations was shown not to influence the voltammetry (Figure 3.2a, red), confirming that the improvements afforded by $LiNO_3$ are due to nitrate anion.

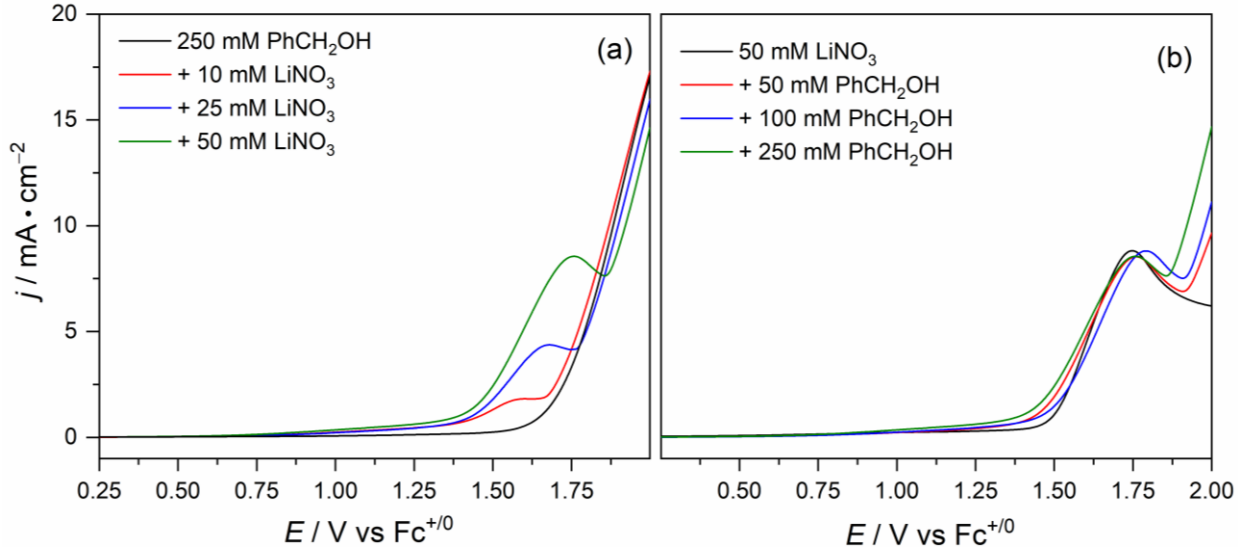

Figure 3.3. LSV on a Pt electrode in MeCN solutions (100 mM Bu_4NPF_6) measuring current dependence on [$LiNO_3$] (a); measuring current dependence on [$PhCH_2OH$]. The scan rate is 25 mV s^{-1} (b).

To glean mechanistic insight regarding NO_3^- oxidation coupled to a solution-based chemical step with $PhCH_2OH$, we collected concentration-dependent LSV traces. Figure 3.3a shows the current dependence on [$LiNO_3$] while maintaining a constant 250 mM $PhCH_2OH$ concentration; as the [NO_3^-] increases, the peak current increases in a linear fashion, revealing a first-order dependence on NO_3^- (Figure B.2). In a parallel experiment, increasing the [$PhCH_2OH$] in solution while keeping the [NO_3^-] constant at 50 mM (Figure 3.3b) reveals a peak current that does not change with the concentration (or presence) of alcohol, i.e., the electrochemical step is zero-order in $PhCH_2OH$ (Figure B.3). Electrochemical NO_3^- oxidation is the rate-determining step and remains distinct from the ensuing chemical steps in which $PhCH_2OH$ is oxidized to PhCHO.

Given the insensitivity to [$PhCH_2OH$] during the electrochemical step, the consumption of benzyl alcohol (and formation of benzaldehyde) was tracked over time during a CPC experiment targeting high conversion. To effect a large conversion, we performed a CPC reaction at 1.68 V vs $Fc^{+/0}$ in acetonitrile containing 20 mM $PhCH_2OH$, 100 mM Bu_4NPF_6, and 50 mM $LiNO_3$ using

a small two-compartment cell. Figure 3.4 displays the result of CPC where the concentrations of benzyl alcohol and benzaldehyde were tracked at 20 min time points by ^{1}H NMR spectroscopy.

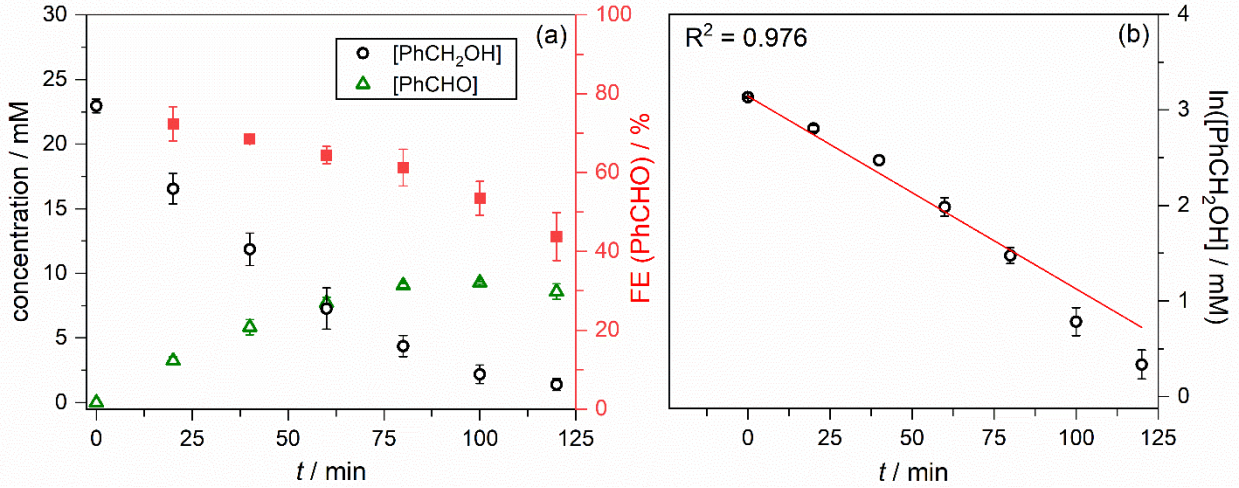

Figure 3.4. Concentration of benzyl alcohol reactant (black) and benzaldehyde product (green) measured at 20 min intervals during CPC at 1.68 V vs $Fc^{+/0}$ in acetonitrile solutions starting from 20 mM $PhCH_2OH$, 50 mM $LiNO_3$, and 100 mM Bu_4NPF_6 (a). Corresponding first-order kinetics plot of ln[$PhCH_2OH$] vs time (b).

At high conversion (> 50%), we note a static concentration of benzaldehyde product (Figure 3.4a), indicating a competitive pathway for nitrate radical that occurs when the alcohol concentration in solution is on the order of the aldehyde concentration. The further oxidation of benzaldehyde has been reported, with volatile CO and benzene as products.[9] The experiment starting with 20 mM benzyl alcohol concludes with a FE ~ 45%, much lower than the previous CPC starting with 250 mM yielding ~80% FE; both loadings produced around 10 mM benzaldehyde, demonstrating that a high loading of benzyl alcohol acts to suppress reactions with aldehyde product. From Figure 3.4b, we observe first-order kinetics for the consumption of benzyl alcohol in the chemical step, distinct from the zero-order dependence revealed by cyclic voltammetry (Figure 3.3b).

So far, the system-dependent stoichiometric behavior of NO_3• remains unexplained. If NO_3• reacts with $PhCH_2OH$ by single-electron transfer to yield an oxygen-centered radical, then one would expect to see NO_3^- regenerated, i.e., mediator behavior in the voltammetry where the peak current increases. Since NO_3^- oxidation remains irreversible in all solution conditions, another mechanism must be at play. The electrochemical system detailed here closely matches our recent findings of nitrate-assisted (but not mediated) reactivity on $BiVO_4$ photoelectrodes. In that report, the irreversibility of the NO_3^-/NO_3• couple is thought to result from stoichiometric nitric acid formation; HNO_3 is a weak electrolyte in acetonitrile ($pK_{a,\,MeCN} \sim 9$).[10] To identify the presence of HNO_3 as an off-cycle species, we carried out CPC in alcohol-free acetonitrile solutions with 50 mM $LiNO_3$ at 1.68 V vs $Fc^{+/0}$ for 16 h before investigating the nitrate speciation using UV–vis spectroscopy (Figure 3.5). Before CPC, only the NO_3^- n → π* transition at 300 nm in acetonitrile is observed; after CPC, this peak is still present in addition to a new peak at ~270 nm. Externally added HNO_3(aq) displays a single peak in acetonitrile at 268 nm, supporting its

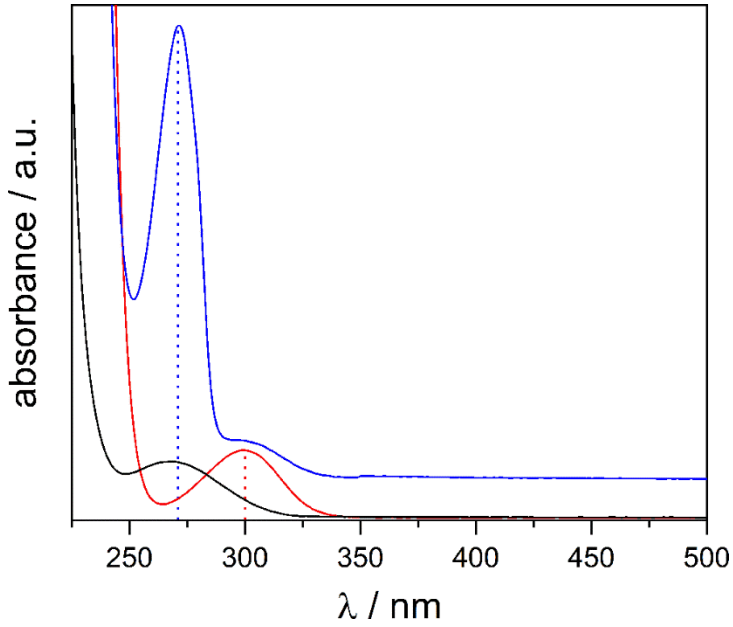

Figure 3.5. UV–vis spectra of acetonitrile solutions before CPC (red) and after CPC (blue) containing 50 mM $LiNO_3$. The black trace is from an acetonitrile solution with HNO_3(aq) added externally.

formation as a direct result of electrochemical NO_3^- oxidation in acetonitrile. A similar system detailing UV-light-driven cyanation reports the $n \rightarrow \pi^*$ transition for $AgNO_3$ at 311 nm and 273 nm for CH_3ONO_2, closely aligning with neutral ($HONO_2$) and anionic nitrate (Bu_4NNO_3) assignments in Figure 3.5.[11] Following the identification of nitric acid in this system, its

electrochemical activity was probed by cyclic voltammetry. HNO_3 displays an oxidation potential > 1.75 V vs $Fc^{+/0}$—more positive than the CPC operating potential of 1.68 V vs $Fc^{+/0}$ (Figure B.4)—representing a dead end for nitrate, rendering the system stoichiometric. The formation of nitric acid from alcohol-free nitrate oxidation demonstrates the HAT mode of reactivity for nitrate radical toward acetonitrile. GC-MS analysis reveals solvent-based oligomer formation occurred both with and without $PhCH_2OH$ in solution as a result of nitrate radical's reactivity (Figure B.5 and Figure B.6), mirroring a report detailing acetonitrile polymerization coupled to perchlorate anion oxidation.[8] This result explains the benzyl alcohol loading-dependent FE due to competition for electrochemically generated nitrate radicals.

To liberate trapped off-cycle nitric acid in solution, a suitable stoichiometric Brønsted base is required. Previous catalysis involving *N*-oxyl mediators and primary alcohols has shown that 2,6-lutidine does not interfere with Pt-based electrocatalysis, and its conjugate acid—2,6-lutidinium—has a $pK_{a,MeCN}$ of 14.1, which should be sufficiently basic to deprotonate nitric acid in acetonitrile.[12] Therefore, we predict the balanced half-reaction for nitrate-catalyzed benzyl alcohol oxidation at the anode to be:

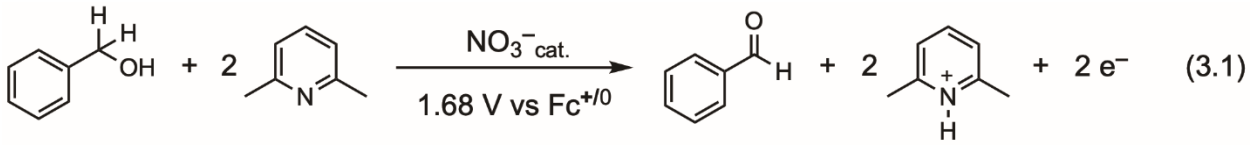

(3.1)

The red traces of Figure 3.6a demonstrate that adding 2,6-lutidine removes the previously observed NO_3^- oxidation peak (black trace), indicating that the surface concentration of NO_3^- is no longer diffusion-limited due to rapid deprotonation of HNO_3. Voltammograms of dilute nitrate solutions also display current enhancements with added 2,6-lutidine (Figure B.7) like the concentrated

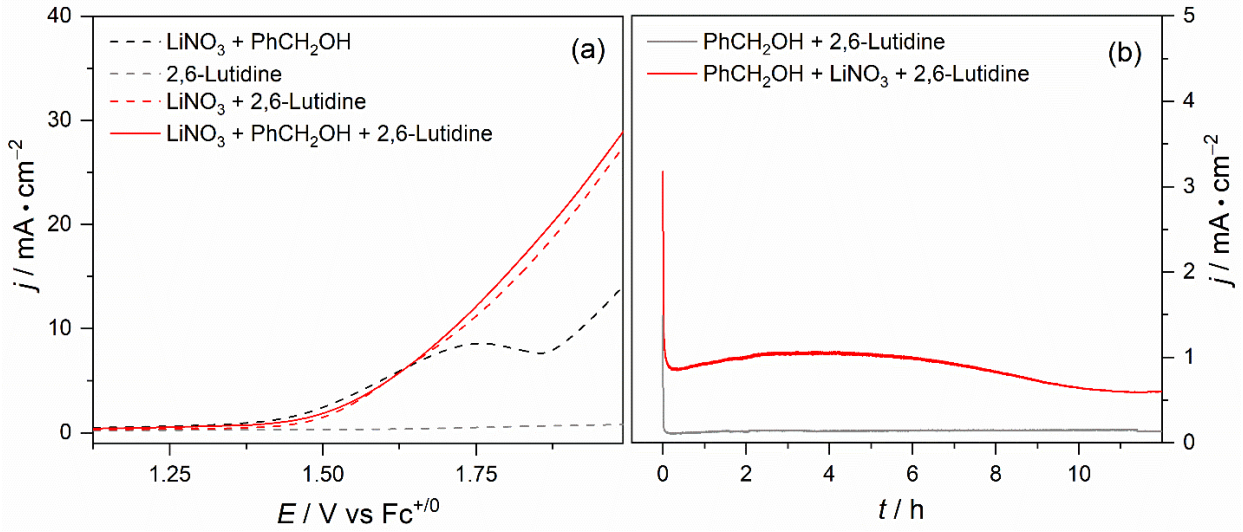

Figure 3.6. LSV on Pt electrodes recorded at 25 mV s^{-1} scan rate in acetonitrile solutions containing [$LiNO_3$] = 50 mM, [$PhCH_2OH$] = 250 mM, and [2,6-Lutidine] = 25 mM as designated (a). CPC at 1.68 V vs $Fc^{+/0}$ on Pt in acetonitrile solutions with 0.5 mM $LiNO_3$, 250 mM $PhCH_2OH$, and 25 mM 2,6-lutidine as noted (b).

solutions shown in Figure 3.6a. Corresponding dilute nitrate CPC experiments (0.5 mM) confirm that the FE for PhCHO, 83 ± 5%, is retained with 2,6-lutidine in solution (Figure 3.6b, red trace); importantly, the measured [PhCHO] is ~5 mM, nearly an order of magnitude higher than the [NO_3^-], signifying catalytic nitrate behavior. Control experiments in Figure 3.6 (dashed traces) confirm that increases in rate observed with 2,6-lutidine require NO_3^-. The results here confirm that the crucial factor for high FE is the substrate loading or ratio of substrate to acetonitrile/benzaldehyde.

With this depiction of base-assisted nitrate mediation, we then questioned how seemingly base-free mediation on CdS nanowires was observed photochemically. We applied rotating ring-disk electrochemistry (RRDE) on Pt to track the species present (or formed) near the electrode surface because of electrochemical NO_3^- oxidation. In the RRDE experiments, we held the disk electrode either at the open-circuit potential or at the same potential we conducted the CPC experiments at (1.68 V vs $Fc^{+/0}$). We then recorded LSV traces at the ring during rotation, affording the data shown in Figure 3.7.

Without NO_3^-, we observed no ring current, demonstrating the high electrochemical stability of Bu_4NPF_6 electrolyte in MeCN. However, when NO_3^- is introduced to the solution (solid lines), a cathodic ring current is measured that increases sharply when the disk is poised at 1.68 V vs $Fc^{+/0}$ (solid red line). This cathodic current cannot be the one-electron reduction of NO_3• back to NO_3^- since the potential onset (−0.7 V vs $Fc^{+/0}$) is far too negative from the nitrate oxidation potential (+1.5 V vs $Fc^{+/0}$), shown in Figure 3.1a. Instead, we considered the oxygen reduction reaction (ORR) since it is known to occur acetonitrile solutions on negatively polarized electrodes.[13] Subsequent LSVs in MeCN with added HNO_3 on Pt show a reduction that is sensitive

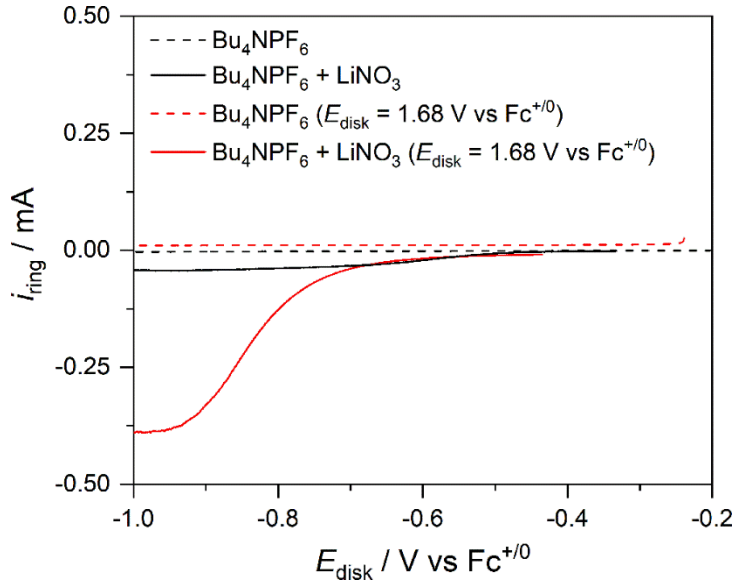

Figure 3.7. LSV traces displaying ring current from rotating ring-disk experiments using a 30 Hz rotation rate in the listed MeCN solutions, where [Bu_4NPF_6] = 100 mM and [$LiNO_3$] = 50 mM. The disk potential is either at the open-circuit potential (OCP) or 1.68 V vs $Fc^{+/0}$ as indicated.

to the presence of protons and cathodic current that is lost upon degassing and purging with argon gas (Figure B.8). These results suggest that the ring current observed only during NO_3^- oxidation is not re-reduction of oxidized nitrate species but instead the proton-coupled oxygen reduction reaction (ORR) in acetonitrile. Oxygen reduction facilitated by the acidification provided during, and collocal to, HNO_3 formation generates reduced oxygen species (ROS) that provide the requisite base needed to render nitrate catalytic.

3.4. Discussion

NO_3^- oxidation in MeCN produces an oxidized intermediate that is capable of subsequently oxidizing $PhCH_2OH$ to PhCHO with ~80% FE under stoichiometric (base-free) or catalytic (2,6-lutidine present) conditions. On Pt, electrochemical NO_3^- oxidation is natively irreversible, where

nitrate terminates as HNO_3 in the absence of an external base; $BiVO_4$ photoanodes showed the same irreversible nitrate consumption. Interestingly, under photochemical control, NO_3^- behaves catalytically on CdS nanowires toward $PhCH_2OH$ oxidation without an added base. Revisiting this result sparked new questions regarding the system-dependent behavior of nitrate. Here, we confirmed that off-cycle nitric acid could be reintroduced by deprotonation with a suitable external base, 2,6-lutidine (Figure 3.6).

Nitrate mediation on Pt electrodes enabled by an external base suggests that a latent proton acceptor present during photocatalysis on CdS is responsible for the unique base-free nitrate mediation observed in that reaction. Revisiting the fundamental differences between these three modes of $PhCH_2OH$ oxidation (photochemical, photoelectrochemical, and electrochemical), we consider the role of the collocal reduction reaction on CdS, where an oxygen atmosphere is required for catalysis to proceed through ORR as the redox counterpart to NO_3^- oxidation. By RRDE on Pt, we identified that acidification of acetonitrile solutions, due to HNO_3 formation, facilitates proton-coupled ORR. By LSV, we measure the reduction potential of the ORR at −1.6 V vs $Fc^{+/0}$ (Figure B.8) in the absence of acid, compared to −0.7 V vs $Fc^{+/0}$ at the ring in RRDE when NO_3^- oxidation occurs at the disk electrode. Our data support that the ORR collocal to NO_3^- oxidation on CdS particles is responsible for more than the completion of the light-driven redox cycle, namely, that in situ generated reduced oxygen species (ROS) serve as the requisite base that renders nitrate catalytic. In photoelectrochemical and electrochemical reactions, the reduction reaction is removed from the working electrode and occurs at a separate counter electrode ∼5 cm away. This distance precludes any ROS existing at the working electrode and thus requires an added Brønsted base to render nitrate catalytic (Figure 3.8).

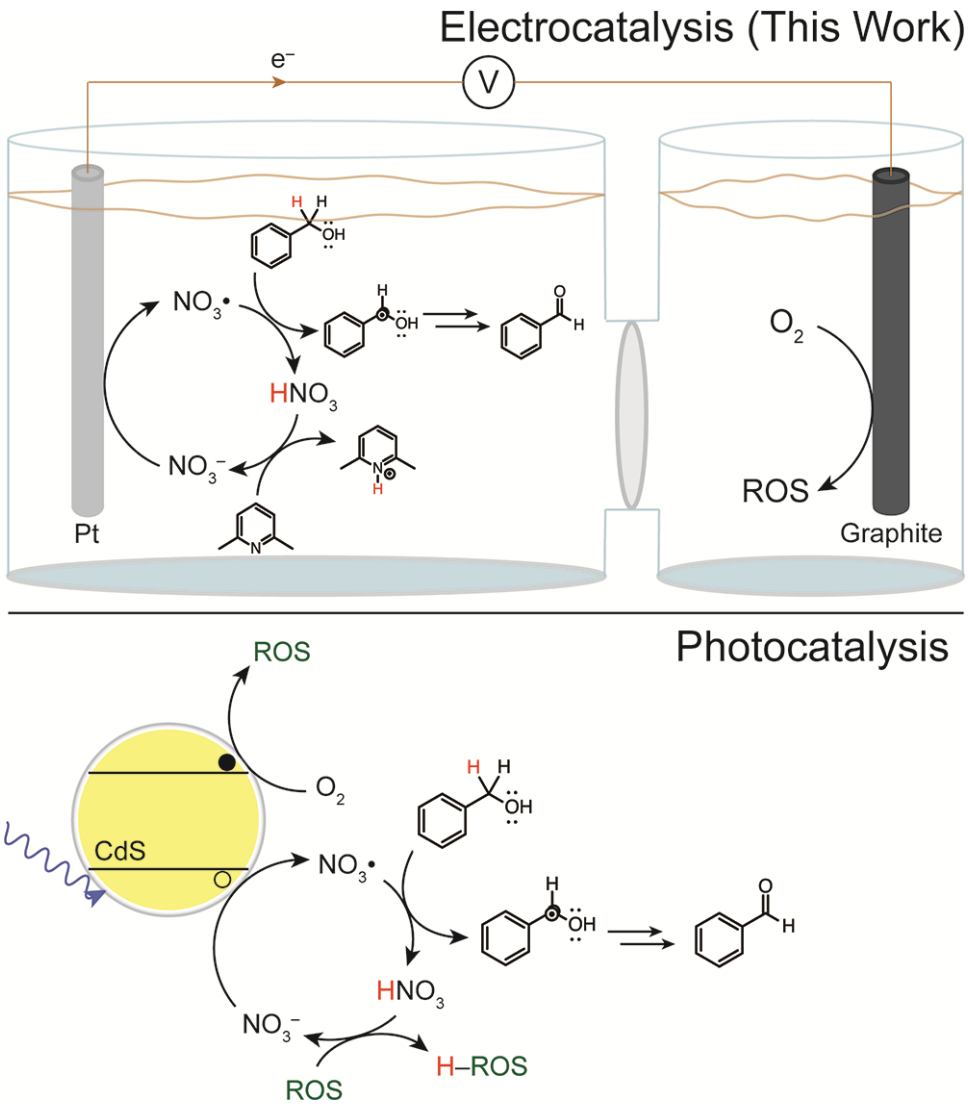

Figure 3.8. Electrochemical Nitrate-Mediated $PhCH_2OH$ Oxidation on Pt Electrodes (Top) Juxtaposed with the Photocatalytic Scheme Operative on CdS Nanowires to Describe General Nitrate Behavior in Acetonitrile Solutions (Bottom).

Previous computational work identified bond dissociation energy (BDE) of the resultant nitroxyl mediator-based O–H bond as a descriptor for the ability of *N*-oxyl mediators to proceed through the HAT mechanism.[14] The authors report that activity for indirect $PhCH_2OH$ oxidation by HAT occurs when BDEs were > 78 kcal mol^{-1} for *N*-oxyl NO–H bonds, and reactivity increases with larger BDE. We surmise that the resultant BDE of nitric acid (O_2NO–H) governs the reactivity of NO_3• here. HNO_3 forms as a byproduct of CPC experiments both with and without alcohol substrate present due to a high BDE for O_2NO–H of 101 kcal mol^{-1},[15] making it at least 15 kcal mol^{-1} stronger than the highest BDE reported for the *N*-oxyl class of mediators (THICA).[14] Competitive H-atom abstraction with solvent represents a fundamental limitation

when housing the electrochemical process in acetonitrile. To slow down solvent-based side reactions, electrochemical NO_3^- oxidation in d_3-acetonitrile was attempted, but we still do not observe a reverse wave feature at 1 V s^{-1}, signifying nitrate radical consumption (Figure B.9). Using aprotic solvents, hexafluorobenzene and trichloroacetonitrile proved unsuccessful due to the limited solubility of the nitrate salts. Future work involves exploring reactions in neat alcohol (solvent-free conditions), where there are no ancillary C–H bonds and the product concentration remains significantly less than the alcohol concentration to ensure that the desired aldehyde product is not consumed.

3.5. Conclusions

Nitrate anion is electrochemically oxidized in acetonitrile solutions to form a highly reactive nitrate radical intermediate. This reactive intermediate is active toward indirect benzyl alcohol oxidation when present. The FE for benzaldehyde product is ~80% with and without a base in 250 mM benzyl alcohol, depending on the loading of alcohol substrate and not the amount of nitrate. Acetonitrile-derived oligomers detected through GC-MS analysis are observed as a side product due to a solvent-based hydrogen-atom transfer (HAT) reaction with nitrate radical, demonstrating the need for high substrate loading to suppress this competitive pathway. Electrochemical nitrate anion oxidation is rate-limiting (first order) zero-order in alcohol substrate; however, the subsequent chemical step shows first-order kinetics in benzyl alcohol consumption. Nitric acid formation occurs under all solution conditions due to a large O_2NO–H bond dissociation energy, making HAT the general mode of reactivity for NO_3• in MeCN. Improving the system design, namely removing ancillary C–H bonds, remains an ongoing effort to promote selective nitrate-mediated alcohol oxidation.

References

[1] Rafiee, M.; Wang, F.; Hruszkewycz, D. P.; Stahl, S. S. *N*-Hydroxyphthalimide-Mediated Electrochemical Iodination of Methylarenes and Comparison of Electron-Transfer-Initiated C–H Functionalization. *J. Am. Chem. Soc.* **2018**, *140*, 22–25

[2] Li, W.-C.; Zeng, C.-C.; Hu, L.-M.; Tian, H.-Y.; Little, R. D. Efficient Indirect Electrochemical Synthesis of 2-Substituted Benzoxazoles Using Sodium Iodide as Mediator. *Adv. Synth. Catal.* **2013**, *355*, 2884–2890.

[3] Chen, J.; Yan, W.-Q.; Lam, C. M.; Zeng, C.-C.; Hu, L.-M.; Little, D. R. Electrocatalytic Aziridination of Alkenes Mediated by *n*-Bu_4NI: A Radical Pathway. *Org. Lett.* **2015**, *17*, 986–989.

[4] Yan, M.; Kawamata, Y.; Baran, P. S. Synthetic Organic Electrochemical Methods Since 2000: On the Verge of a Renaissance. *Chem. Rev.* **2017**, *117*, 13230–13319

[5] Terry, B. D.; DiMeglio, J. L.; Cousineau, J. P.; Bartlett, B. M. Nitrate Radical Facilitates Indirect Benzyl Alcohol Oxidation on Bismuth(III) Vanadate Photoelectrodes. *ChemElectroChem* **2020**, *7*, 3776–3782.

[6] DiMeglio, J. L.; Breuhaus-Alvarez, A. G.; Li, S.; Bartlett, B. M. Nitrate Mediated Alcohol Oxidation on Cadmium Sulfide Photocatalysts. *ACS Catal.* **2019**, *9*, 5732– 5741.

[7] Hering, T.; Slanina, T.; Hancock, A.; Wille, U.; König, B. Visible light photooxidation of nitrate: the dawn of a nocturnal radical. *Chem. Commun.* **2015**, *51*, 6568–6571.

[8] Tourillon, G.; Lacaze, P-C.; Dubois, J-E. Electrochemical formation of thin polyacetonitrile films on a Pt surface: P.m.t., i.r., x.p.s. and s.i.m.s. analyses and study of formation mechanism. *J. Electroanal. Chem. Interfacial Electrochem.* **1979**, *100*, 247–262.

[9] Iyo, O.; Akiho, S.; Iino, M. Kinetics for Reactions of the Nitrate Radical (NO3•) with Aldehydes in Acetonitrile. *J. Phys. Chem. C* **1989**, *93*, 4079–4083.

[10] Eckert, F.; Leito, I.; Kaljurand, I.; Kütt, A.; Klamt, A.; Diedenhofen, M. Prediction of Acidity in Acetonitrile Solution with COSMO-RS. *J. Comput. Chem.* **2009**, *30*, 799–810.

[11] Zou, S.; Li, R.; Kobayashi, H.; Liu, J.; Fan, J. Photo-assisted cyanation of transition metal nitrates coupled with room temperature C–C bond cleavage of acetonitrile. *Chem. Commun.* **2013**, *49*, 1906–1908.

[12] Kaljurand, I.; Kütt, A.; Sooväli, L.; Rodima, T.; Mäemets, V.; Leito, I.; Koppel, I. A. Extension of the self-consistent spectrophotometric basicity scale in acetonitrile to a full span of 28 pKa units: unification of different basicity scales. *J. Org. Chem.* **2005**, *70*, 1019–1028.

[13] Maricle, D. L.; Hodgeson, W. G. Reduction of Oxygen to Superoxide Anion in Aprotic Solvents. *Anal. Chem.* **1965**, *37*, 1562–1565.

[14] Dao, R.; Zhao, C.; Yao, J.; Li, H. Distinguishing Ionic and Radical Mechanisms of the Hydroxylamines Mediated Electrocatalytic Alcohol Oxidation using the NO-H Bond Dissociation Energy. *Phys. Chem. Chem. Phys.* **2018**, *20*, 28249–28256.

[15] Benson, S. W. III – Bond Energies. *J. Chem. Educ.* **1965**, *42*, 502.

Chapter 4

Manganese Oxide Films for Selective Alcohol Oxidation in Neutral Brine

4.1. Introduction

Water splitting in brine is a key strategy in producing renewable hydrogen fuel (H_2) without exploiting precious freshwater resources.[1,2] Seawater constitutes 97% of available water reserves on the planet with a native ~600 mM chloride anion concentration.[3] In brine, chloride anion oxidation tends to kinetically outcompete water oxidation, overcoming thermodynamic disadvantages and a lower concentration, making active chlorine species the commonly observed (anodic) product (Equations 4.1–4.4).[4]

$$2Cl^- \xrightarrow{-2e^-} Cl_2 \qquad E° = +1.36 \text{ V vs NHE} \qquad (4.1)$$

$$Cl^- + H_2O \xrightarrow{-2e^-} HClO + H^+ \qquad E° = +1.48 \text{ V vs NHE} \qquad (4.2)$$

$$Cl^- + H_2O \xrightarrow{-2e^-} ClO^- + 2H^+ \qquad E° = +1.72 \text{ V vs NHE} \qquad (4.3)$$

$$H_2O \xrightarrow{-4e^-} O_2 + 4H^+ \qquad E° = +1.23 \text{ V vs NHE} \qquad (4.4)$$

Despite the industrial intrigue of chlorine produced via brine electrolysis (chlor-alkali process),[5] overproduction of chlorine gas (or other active chlorine species) at the scale required for a global H_2 economy is problematic. Therefore, the design and realization of material surfaces inactive for chloride oxidation but active for desired alternative anodic transformations in crucial. So far, examples of CER-disfavored electrolysis in brine are limited to the oxygen evolution reaction (OER),[6] which offers oxygen as a low value product with the potential to form explosive mixtures upon introduction to gaseous H_2 coproduct. Among alternatives, alcohol oxidation is promising as it provides protons for hydrogen evolution and replaces O_2 production with carbonyl formation, alleviating safety concerns of product gas mixing. Carbonyl compounds are common industrial precursors for fine and commodity chemical syntheses, and when prepared from biorenewable inputs, abate reliance on petrochemicals.[7] 5-hydroxymethylfurfural (5-HMF) is a furanic platform molecule obtained from cellulosic biomass that can be oxidized to form

furandicarboxylic acid (FDCA), a structural analogue to polyethylene terephthalate commonly used in packaging applications.[8] Converting cellulosic biomass "waste" to valuable industrial precursors requires suitable platforms to deliver the intended products with sustained activity.[9]

Electrochemical conversion of 5-HMF to FDCA has been achieved on first row transition metal oxides but is generally limited to alkalized (chloride-free) aqueous media or homogenous redox mediators for desired selectivity;[10,11] for direct electrochemical alcohol oxidation, we elected to explore materials with preferential OER activity in neutral brine. Sodium intercalated A_xMnO_2 films undergo a surprising change in reactive preference from commonly observed chloride oxidation in brine on electrodeposited Na_xMnO_2 to preferential OER activity in neutral brine enabled by thermal formation of oxygen vacancies during annealing.[6] To date, the competitive rates of chloride anion oxidation and primary alcohol oxidation in neutral brine conditions have not been compared. To encourage selective electrochemical carbonyl generation in brine, we introduced oxygen vacancies as strategic defects to study the influence these reactive sites have on the relative reaction rates under atmospheric conditions.

4.2. Experimental

4.2.1. Chemicals and Materials

Water from a Millipore filtration system (18.2 MΩ • cm^{-1}) was used to prepare all aqueous electrolytes. Hydrochloric acid (Certified ACS Plus, 36.5%–38.0%), sodium chloride, and 5-hydroxymethylfurfural were purchased from Fisher Scientific. Manganese(II) sulfate monohydrate was purchased from Alfa Aesar. Sodium perchlorate was purchased from Sigma. All purchased chemicals were used without further purification. Fluorine-doped tin oxide glass substrate (NSG TEC 15) was purchased from Pilkington North America and Nafion^{TM} membranes (NRE-212) were purchased from Fuel Cell Earth.

4.2.2. MnO_x and Na_xMnO_2 Film Preparation

Manganese oxide films were electrodeposited on clean FTO (Chapter 2.2.2) adapted from reported methods.[12] An FTO (taped to expose 2.54 cm x 2.54 cm) working electrode was suspended in ~40 mL of electrolyte along with a Pt coil counter electrode and a Ag/AgCl (saturated KCl) reference electrode (RE) in a 50 mL beaker. Na_xMnO_2 films were prepared in 2 mM $MnSO_4 • H_2O$ electrolyte containing 50 mM $NaClO_4$ by applying 1.0 V vs RE to pass 903 mC (140 mC cm^{-2}); deposited films were rinsed with MQ water and dried under a gentle N_2 stream, yielding contiguous light brown films with a purple hue. Similarly, MnO_x films were prepared in 20 mM

$MnSO_4 \bullet H_2O$ with 50 mM HCl by applying 1.1 V vs RE to pass 140 mC cm^{-2} before rinsing and drying to give brown films. Oxygen vacancies were thermally introduced by annealing under atmosphere films at 400 °C for 2 hours (10 °C min^{-1} ramp) based on a previous report.[6]

4.2.3. Material Characterization

Surface morphologies of H_xMnO_2 and Na_xMnO_2 electrodes were imaged with field-emission scanning electron microscopy (SEM) on an EMAL JEOL JSM-7800FLV; an accelerating voltage of 10 kV was applied at a working distance of 10 mm. Powder X-ray diffraction (XRD) data were collected for these films before and after annealing on a Panalytical Empyrean diffractometer using a Cu Kα radiation source (λ = 0.15418 nm) at 1.8 kW (40 mA, 45 kV). X-ray photoelectron spectroscopy was performed on a Kratos Axis Ultra X-ray photoelectron spectrometer using Monochromatized Al Kα X-rays (1486.7 eV) under a pressure of 1×10^{-9} Torr. High resolution manganese 3s, oxygen 1s and carbon 1s spectra were collected using a step size of 0.1 eV and pass energy of 20. Spectra were shifted to align with adventitious carbon (248.8 eV) for each sample.

4.2.4. Electrochemistry

A custom 2-compartment glass compression cell was used for all electrolytic experiments where subsequent product analysis was required. Viton O-rings (CG-305-112) with a 20 mm inner diameter and 24 mm outer diameter were used to compress the deposited films to the face of the cell (exposing 3.153 cm^2 of film to electrolyte). Voltammetry was collected in a 50 mL beaker using a three-electrode support. All electrochemical measurements were made using platinum counter electrodes, Ag/AgCl (saturated KCl) reference electrodes and manganese oxide films on FTO working electrodes. Solution mixing (900 rpm) during electrolysis in the working compartment was ensured with a Teflon stir bar. A CH Instruments Electrochemical Workstation 660C was used for all electrochemical measurements and for manganese oxide film generation.

4.3. Results

Manganese oxide films electrodeposited from manganese sulfate solutions with different supporting cations were characterized with XRD to resolve electrodeposition and annealing influences on film crystallinity and phase (Figure 4.1). Films deposited from sodium-containing

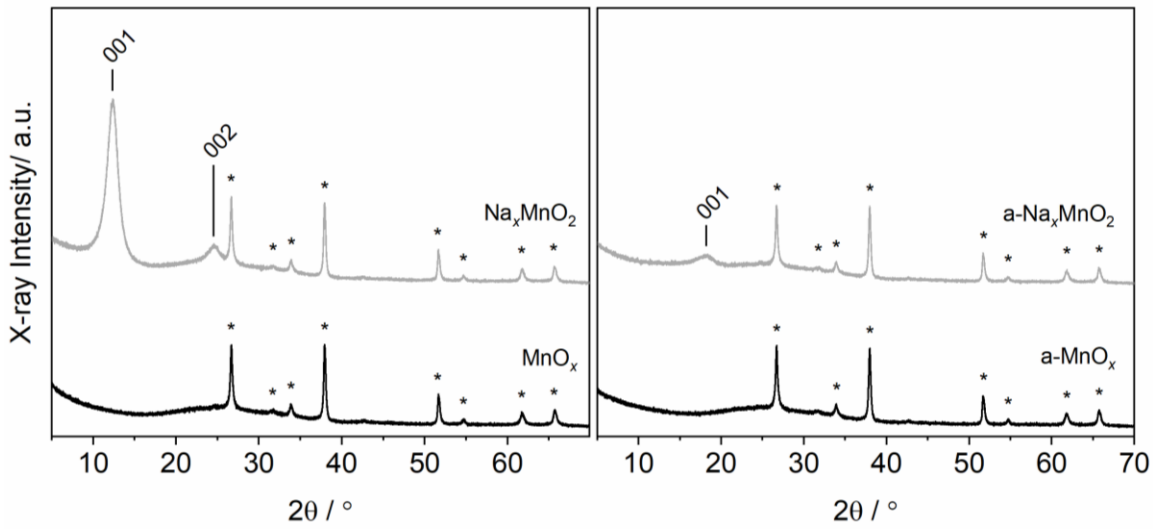

Figure 4.1. X-ray diffractograms of manganese oxide films grown on fluorine-doped tin oxide (FTO) substrate. Reflections from FTO are designated with an asterisk.

electrolyte show the (001) and (002) planes for layered crystalline birnessite, located at 12.3° and 24.6°, respectively. The 002 plane is lost upon annealing (a-Na_xMnO_2), along with a 001-plane shift from 12.3° to 18.2°, matching expectations from recent literature.[6] The presence of sodium was confirmed in the XPS survey scan before and after annealing (Figure C.1). MnO_x films obtained from a similar electrodeposition procedure in a metal cation-free electrolyte showed no crystalline features by XRD (Figure 4.1) and no intercalated sodium cations by XPS after electrodeposition and annealing (Figure C.1). Top-down scanning electron micrographs show electrodeposition-dependent surface morphologies for Na_xMnO_2 and MnO_x that are preserved after annealing (Figure C.2).

As-made Na_xMnO_2 films yield an average surface manganese oxidation state (AOS) of 3.7 that drops to 3.4 after annealing (Figure C.3), given by equation 4.5, derived for lanthanum manganite species.[13]

$$\mathrm{AOS} = 9.67 - 1.27\Delta\mathrm{E}(\mathrm{Mn\ 3}s) \,/\, \mathrm{eV} \qquad (4.5)$$

This change in manganese AOS has previously been attributed to oxygen vacancy formation;[6] here, we observe the expected increase in signal intensity at ~531 eV as such (Figure 4.2). In contrast to Na_xMnO_2, annealing MnO_x films produces no observable change in manganese oxidation state (AOS = 3.5) (Figure C.3) despite an increase in the 531 eV feature of the O 1s XPS spectrum (Figure 4.2).

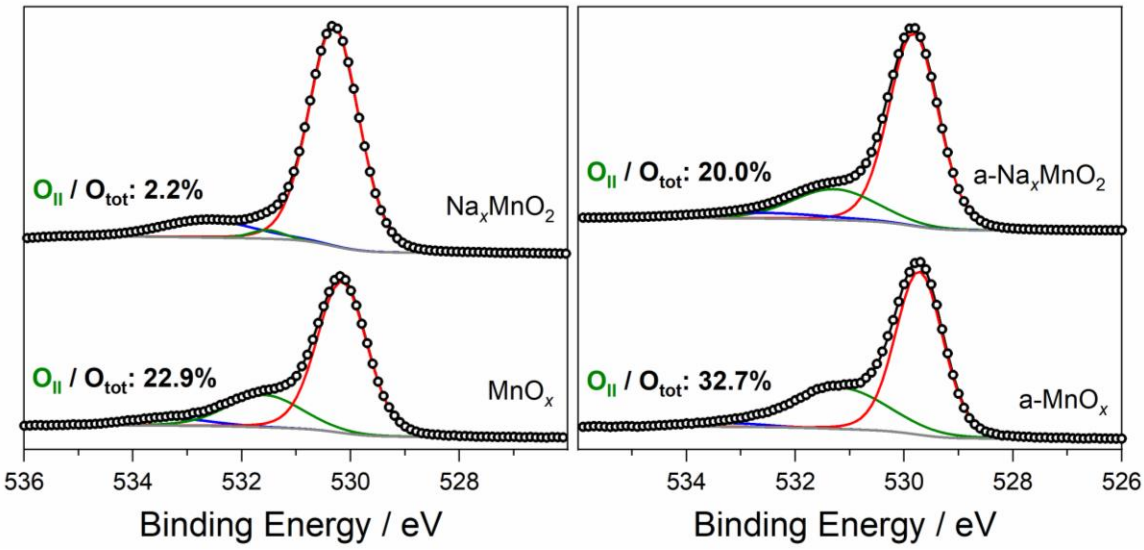

Figure 4.2. Deconvoluted O 1s signals from XPS for manganese oxide films as electrodeposited and after annealing. Red traces correspond to metal-oxo environments (529 eV – 530 eV), green traces to hydroxyl groups/oxygen vacancies (531 eV – 531.6 eV), and blue traces to water (533 eV).

Annealing influences on Mn oxidation state were confirmed by a bulk titration method comparing pre-annealed and post-annealed films;[14] currently, the average loading of manganese after electrodeposition is not known, but annealing is not expected change the manganese loading for like-deposited films, enabling a qualitative assessment on the influence of annealing on bulk Mn AOS for each film type (Figure C.4). From titration, the preservation in Mn AOS for MnO_x is observed, along with the reduction of AOS for Na_xMnO_2 films post annealing, consistent with surface measurements by XPS.

For thorough compositional analysis of MnO_x, quantitative assessment of bulk Mn AOS should be determined by obtaining Mn film loading through inductively coupled plasma mass spectrometry (ICP-MS) (as well as Na_xMnO_2 films). Raman analysis can distinguish between Mn and O stoichiometry for different Mn oxides, as well as different MnO_x phases to provide information not captured by XRD in Figure 5.1.[15,16] Energy dispersive X-ray (EDX) analysis of electrodeposited films could support the Mn:O stoichiometry results from Raman, along with cross section SEM/EDX to determine film thickness for MnO_x and Na_xMnO_2 films (before and after annealing). To corroborate the oxygen vacancy determination by XPS, chemical titration should be performed using a published procedure to distinguish between Bronsted acid sites (OH) and Lewis acid sites (oxygen vacancies) on the manganese oxide films surfaces.[17]

Linear sweep voltammograms (LSVs) were collected on manganese oxide films to observe influences imparted by 5-HMF in brine. Successive scans were performed on a single film from open circuit potential (OCP) to 1.55 V vs Ag/AgCl—adjusted to RHE using measured solution pH

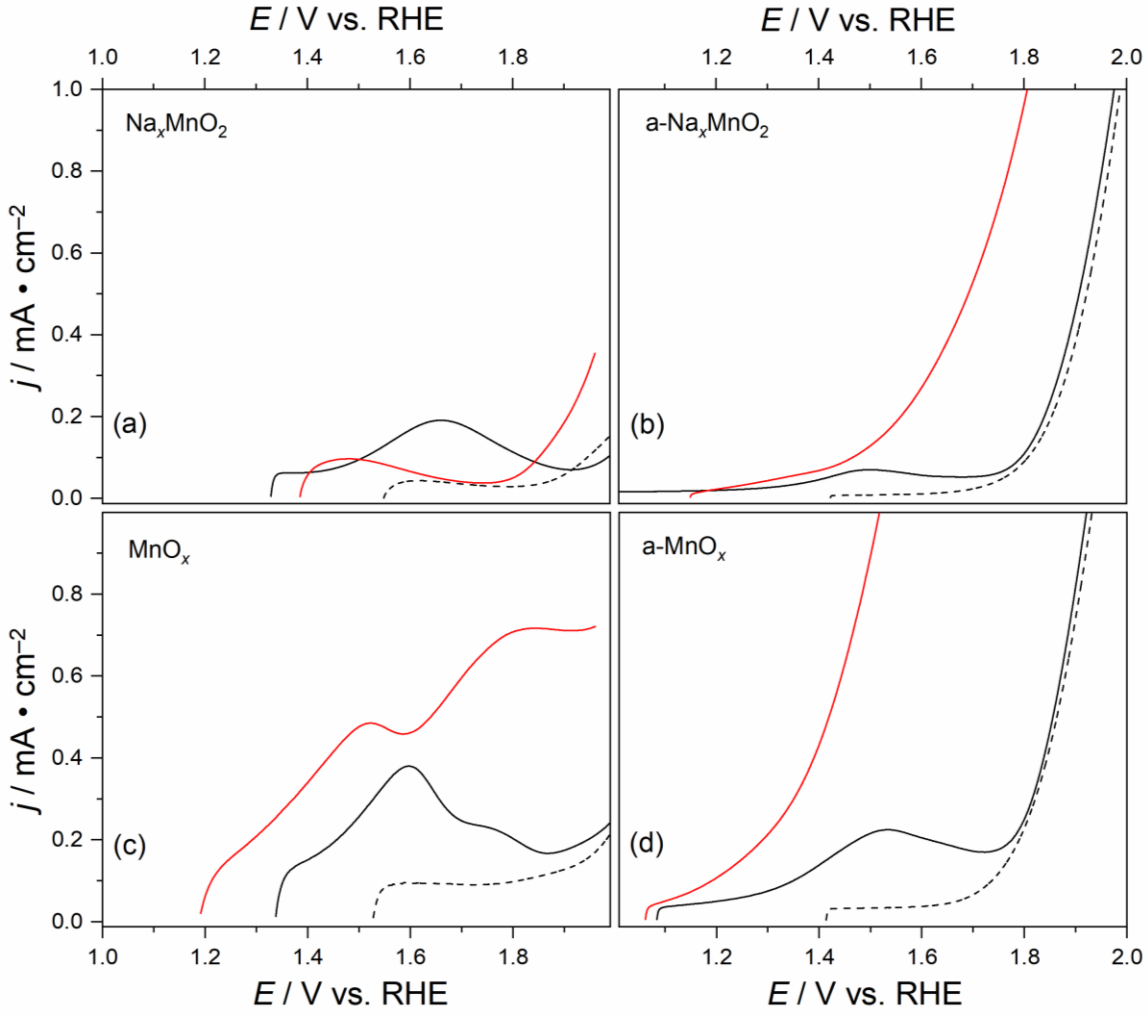

Figure 4.3. Sequential LSVs at 10 mV s-1 in 600 mM NaCl(aq) without (black traces) and with (red traces) 100 mM 5-HMF. Solid black traces are the first scan in alcohol-free brine; dashed traces are the second scan on the same film in brine. The 3rd LSV on a single film is performed in brine containing 5-HMF.

—at 10 mV s^{-1} with 5 minutes of stirring in the electrolyte between scans. Figure 4.3 shows the voltammetry for Na_xMnO_2 films, where a peak is observed at ~1.6 V vs RHE before a current takeoff (E > 1.85 V vs RHE); this small feature is not present during a second scan on the same film in alcohol-free brine electrolyte. The addition of 5-HMF into the electrolyte led to a negative shift in onset potential and a small recovery in the peak current before an earlier current takeoff (E > 1.75 V vs RHE). Annealed Na_xMnO_2 films show a diminished peak relative to unannealed Na_xMnO_2 that occurs at a more negative potential (~1.5 V vs RHE) with a much sharper current

increase following the peak. The peak feature is not observed on the follow-up scan in the same electrolyte, matching unannealed Na_xMnO_2. Adding 5-HMF to the electrolyte showed stark a voltametric influence on annealed sodium-intercalated films, where the current on the 3rd scan surpasses that of the 2nd in alcohol-free brine at all potentials scanned. Similar analyses on MnO_x reveal notable differences between films electrodeposited from different conditions. For unannealed MnO_x, two features are observed (1.6 V & 1.7 V vs. RHE) that are not observed in a follow-up alcohol-free scan in brine, matching the deactivation observed for Na_xMnO_2. The third scan in brine with 5-HMF showed a reemergence of the two features observed in the first scan, albeit with different relative current densities. Annealing the MnO_x influenced the voltammetry in a way consistent with previous Na_xMnO_2 films; MnO_x films after annealing show the sharpest raw current density increase induced by 5-HMF of all film types tested. A similar series of scans was performed in 600 mM $NaNO_3$ to resolve the role of chloride in the electrolyte. In nitrate, the voltammetry closely follows that of chloride (Figure C.5).

The electrochemical reversibility of the features observed in brine electrolytes for as made and annealed MnO_x was probed with cyclic voltammetry (Figure C.6). In 5-HMF-free brine electrolyte, the Mn oxidation event at ~1.6 V vs RHE shows a corresponding reduction feature near 1.5 V vs RHE with a ratio of cathodic peak current to anodic peak current ~0.45, demonstrating quasi-reversibility. For each consecutive scan, the peak currents become smaller. Performing an analogous CV in 5-HMF-containing brine gives the opposite trend, where anodic and cathodic peak currents *increase* over time, most pronounced in the annealed films. The nature of 5-HMF-induced activation was explored in greater depth by comparing the influence of time under bias—electrochemical activation—to effects observed from pre-LSV 5-HMF brine exposure time—chemical activation. Figure C.7a displays the response for multiple rapid successive scans on MnO_x when starting in 5-HMF solution, with minimal delay between scans. For each successive scan, the current density recorded decreased until collapsing to a consistent response observed by scan 5. This result was then compared to scans performed with varying exposure (soak) times in brine with 5-HMF; for Figure C.7b, the MnO_x films were held at 1.65 V vs RHE in alcohol-free brine electrolyte until the current became flat before exposure to 5-HMF brine solution for varying soak times pre-LSV. These results show a current increase based on the exposure time in 5-HMF-containing brine at open circuit potential, contrasting with the current decrease observed for multiple rapid scans in the same electrolyte. Corresponding results on

annealed MnO_x show a similar trend (Figure C.8) but to a lesser extent, requiring the soak time LSVs to be performed in 5-HMF-free brine (current with 5-HMF was too large to resolve a difference) .

Long term influences of 5-HMF and applied potential exposure (CPC) were probed by stirring annealed MnO_x in brine electrolyte with 5-HMF at OCP for 4 hours and comparing to a film experiencing a constant 1.65 V vs RHE during that time (Figure 4.4); the response in 5-HMF-free brine is included for comparison.

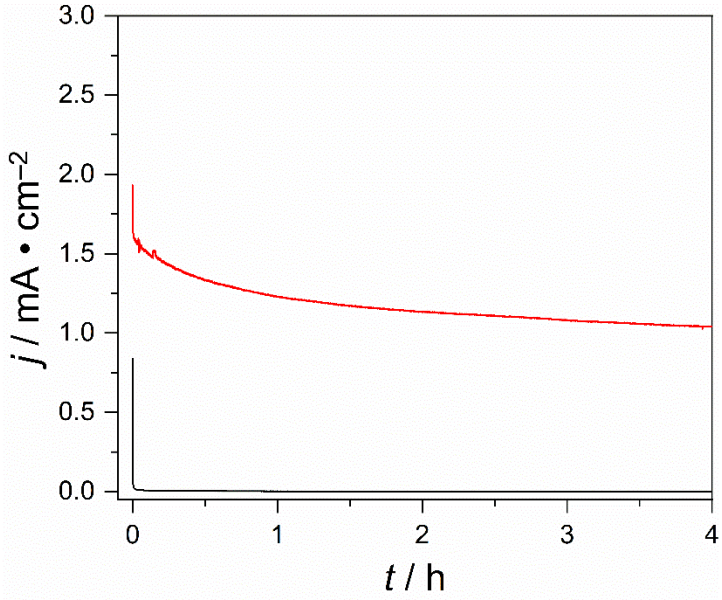

Figure 4.4. Constant potential coulometry traces on a-MnO_x films in 600 mM NaCl(aq) (black) and with 100 mM 5-HMF (red) while applying 1.65 V vs RHE.

As shown in Figure 4.4, 5-HMF is required to observe current density at this applied potential over the 4-hour experiment. Films recovered after constant applied bias (in brine with and without 5-HMF) showed a strong retention in color compared to the bias-free film stirred in 5-HMF-containing brine that became a much fainter yellow after exposure (Figure C.9). XPS analysis of these films show notable changes in the Mn AOS, as well as relative contribution of 531 eV signal intensity in O 1s lines (Table 4.1).

Table 4.1. Mn 3s and O 1s XPS.

	Mn AOS	O_{II} / O_{tot}
Na_xMnO_2	3.73	2.2%
a-Na_xMnO_2	3.31	20.0%
MnO_x	3.44	22.9%

a-MnO_x	3.45	32.7%
a-MnO_x | 5-HMF CPC	3.62	34.1%
a-MnO_x | 5-HMF stir	3.96	31.4%
a-MnO_x | CPC	3.47	22.7%

Exposure to 5-HMF without bias lead to a large increase in Mn AOS (3.45 to 3.96) with a relative retention in defect oxygen contribution to O 1s. With a bias applied in 5-HMF-containing brine, an increase in Mn AOS is also observed, albeit to a much lower degree; the more substantial Mn AOS change was accompanied by a drastic color change (Figure C.9). The annealed MnO_x film subjected to a 4-hour CPC at 1.65 V vs RHE in alcohol-free brine showed a preservation in original Mn AOS (~3.45) but a smaller O_{II} contribution from ~32% to ~23% with minimal color change; 5-HMF-free CPC produced films displaying Na 1s lines by XPS that were not observed in 5-HMF brine solutions, with and without applied bias. ICP-MS of solutions after 4 hours reveals a much larger dissolution of Mn following the 5-HMF stir than the CPC in brine with 5-HMF (Figure C.10); here, films with pronounced color changes are accompanied by the largest Mn AOS changes and increases dissolved Mn content in solution.

Product analysis is needed to confirm electrochemical 5-HMF oxidation on a-MnO_x films in brine electrolyte. Given the array of intermediates possible (dialdehyde, alcohol/carboxylic acid, aldehyde/carboxylic acid and dicarboxylic acid), chromatographic techniques are recommended. The relative buildup of intermediates for as made MnO_x and a-MnO_x will provide important information regarding the chemical and electrochemical processes involved in alcohol oxidation on manganese oxide electrodes.

4.4. Discussion

Crystalline Na_xMnO_2 prepared by electrodeposition show the expected planes of the birnessite phase that are lost upon annealing. After annealing, the Mn AOS drops from 3.73 to 3.31 (consistent with previous reports),[6] that is attributed to the formation of oxygen vaccines (Figure 4.2). In contrast, MnO_x show no change in Mn AOS after annealing despite the increase in the O_{II} feature of O 1s XPS spectra. To rationalize this result, we've considered the presence of a charge-balancing cation (H^+) that is present in as made MnO_x but quenched to some extent in a-MnO_x to maintain Mn AOS. In Na_xMnO_2 films, the Na^+ might not eliminate like the proton does

to preserve charge, requiring a decrease in Mn AOS; Equations 4.6, 4.7 provide possible explanations for this observation.

$$Na_xMnO_2(s) \longrightarrow Na_xMnO_{2-\mathbf{a}}(s) + 0.5\mathbf{a}O_2(g) \quad (4.6)$$

$$H_yMnO_2(s) \longrightarrow H_{y-2\mathbf{b}}MnO_{2-\mathbf{b}}(s) + \mathbf{b}H_2O(g) \quad (4.7)$$

Preliminary voltammetry on manganese oxide films reveals redox features in brine that are lost upon subsequent scans, signaling quenching of this redox event (chemically irreversible). Annealed films of both types show a diminished redox feature before a much larger (chloride or water oxidation) current takeoff on the first scan and a similar loss in redox feature in the second scan. Introducing 5-HMF to the brine electrolyte led to a resurgence of current on all films except the as made Na_xMnO_2, which was the only one to have an exceedingly low concentration of defect oxygen (~2%) by O 1 s XPS. Surprisingly, quenching this redox feature after CPC in 5-HMF-free brine (Figure 4.4, black trace) led to a diminution in defect oxygen concentration (Table 4.1, entry 7) on a-MnO_x films that was not observed by CPC in brine with 5-HMF or stirring at OCP. The survey scan for 5-HMF-free CPC reveal Na^+ ions present, suggesting the redox feature may be the quenching of oxygen vacancies with concerted intercalation of Na^+ ions from brine to charge balance. With 5-HMF in brine, no Na^+ is observed after reacting and the O_{II} contribution remains the same despite Mn AOS increases (Table 4.1, entries 5 and 6). This electrochemical quenching of O_{II} in alcohol-free brine is likely the reverse reaction discussed for thermally induced oxygen vacancies (equations 4.6 & 4.7), where cations are required to intercalate following the loss of oxygen vacancies; CPC with 5-HMF doesn't appear to quench oxygen vacancies in the same way. Current traces presented in Figure 4.2 show higher current with 5-HMF in solution on manganese oxide films with higher O_{II} amounts by XPS. Thus, oxygen vacancies may improve the electrochemical activity of manganese oxide films in brine, possibly by participating as a reactive site able to facilitate 5-HMF oxidation. For annealed films, the capacitive feature observed just positive of OCP is diminished, indicating that oxygen vacancies (or the electrons they supply) may render the manganese oxide films more conductive and thus better electrocatalyst materials.

To rationalize the increase in Mn AOS that accompanies exposure to 5-HMF, we considered the experiments probing electrochemical vs chemical activation of Mn films promoted by 5-HMF (Figure C.6–C.8). A chemical oxidation of 5-HMF by Mn^{4+} at the surface should result

in Mn^{4+} reduction and thus a drop in Mn AOS; the *increase* in Mn AOS required a mechanistic proposal in which 5-HMF oxidation could occur, along with Mn oxidation. Frost diagrams indicate instability of Mn^{3+} species relative to Mn^{2+} and Mn^{4+} suggesting Mn^{3+} formed during the reaction between Mn^{4+} and 5-HMF may disproportionate into soluble Mn^{2+} and insoluble Mn^{4+}.[18] If disproportionation were occurring, the solution Mn content would be expected to increase. ICP-MS of solutions recovered after MnO_x exposure to 5-HMF at open circuit shows a higher dissolved Mn content than solutions where CPC was performed. Less dissolution of Mn is accompanied by a smaller Mn AOS increase and a far less noticeable film color change/removal. Collecting these observations, Figure 4.5 portrays a preliminary description to detail the chemical and electrochemical interactions between 5-HMF substrate and a-MnO_x.

Given the smaller Mn AOS change and less Mn dissolution when a bias is applied, direct 5-HMF oxidation on a-MnO_x is likely the dominant process at play, since the current in 5-HMF-containing brine in rapid subsequent scans (Figure C.8a) drops by much less than the decrease

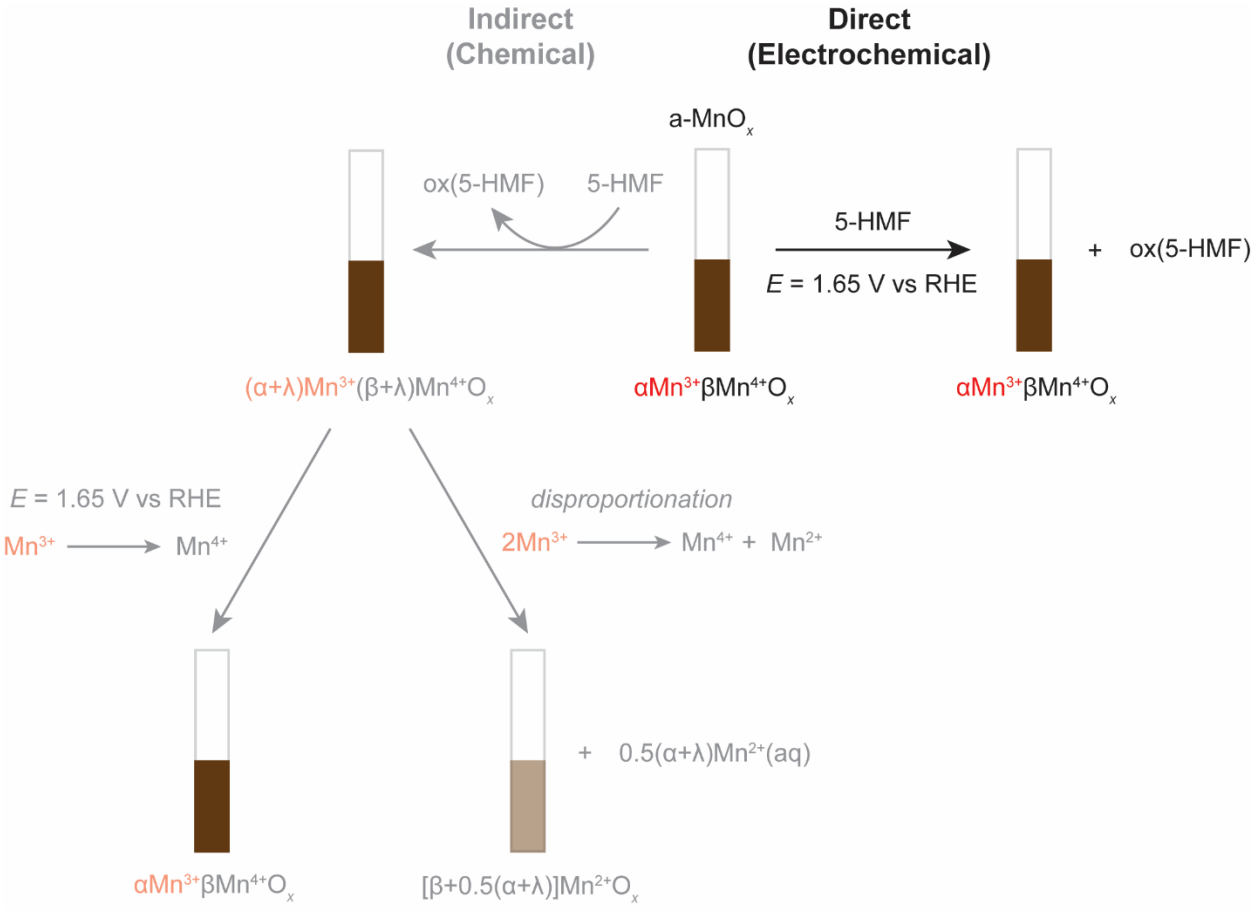

Figure 4.5. Proposed interactions between solution phase 5-HMF in brine and solid a-MnO_x electrodes.

observed on MnO_x (Figure C.7a). The recovery of current based on exposure time to brine with 5-HMF is also far lower on a-MnO_x than MnO_x, showing that the chemical (or spontaneous) process on MnO_x is faster relative to the electrochemical process when compared to a-MnO_x films. On a-MnO_x, the electrochemical process dominates the current response and seems to protect Mn consumption by 5-HMF. To support this proposal, product analysis is necessary to ensure that the proposed routes afford similar intermediate buildup so the differences in voltammetry between MnO_x and a-MnO_x can be accurately described. The role of chemical vs electrochemical 5-HMF oxidation rates on MnO_x and a-MnO_x films can be better understood by ensuring the surface acid site concentrations for both film types (Lewis acid vs Bronsted acid) is consistent with the O_{II} feature (Figure 4.2).[17] If the 531 eV O 1s feature for MnO_x is from surface hydroxyl species and not oxygen vacancies, the faster relative chemical reaction with 5-HMF could signal OH involvement in the process. Likewise, a conversion of surface hydroxyl to oxygen vacancy by annealing may promote electrochemical reactivity at newly formed oxygen vacancy sites.

4.5. Conclusions

Manganese oxide films can be grown reliably on fluorine-doped tin oxide by Mn^{2+} oxidation from manganese sulfate solutions. Crystalline birnessite Na_xMnO_2 films are recovered via electrodeposition in electrolyte with sodium cations present. When an acid electrolyte is used, amorphous MnO_x films are produced. Annealing Na_xMnO_2 films shows a reduction of Mn AOS that is not observed for MnO_x. For both films, the 531 eV signal in O 1s XPS increases, supporting a thermally-induced formation of oxygen vacancies. Voltammetry shows an increase in current with 5-HMF included to the brine electrolyte that is much greater for annealed Na_xMnO_2 and MnO_x. a-MnO_x can deliver > 1 mA cm^{-2} in brine electrolyte with 100 mM 5-HMF for 4 hours when encouraged with 1.65 V vs RHE applied potential. With no bias, a-MnO_x in brine with 5-HMF show film discoloration and increases in Mn AOS (3.45 to 3.96) that correspond to a higher dissolved manganese content. With bias applied, film discoloration is reduced, the Mn AOS increase occurs to a smaller extent and less dissolved Mn is observed. In brine electrolyte with 5-HMF, the applied bias acts to protect the film from spontaneous chemical processes that lead to undesired film destruction.

References

[1] Mohammed-Ibrahim, J.; Moussab, H. Recent advances on hydrogen production through seawater electrolysis. *Mater. Sci. Engergy Technol.* **2020**, *3*, 780–807.

[2] K. S.-C.; Chen, R.; Chen, G.-H.; Ma, X.-L. Mini Review on Electrocatalyst Design for Seawater Splitting: Recent Progress and Perspectives. *Energy Fuels* **2021**, *35*, 12948–12956.

[3] Dresp, S.; Dionigi, F.; Klingenhof, M.; Strasser, P. Direct Electrolytic Splitting of Seatwater: Opportunities and Challenges. *ACS Energy Lett*. **2019**, *4*, 933–942.

[4] Du, J.; Chen, Z.; Chen, C.; Meyer, T. J. A Half-Reaction Alternative to Water Oxidation: Chloride Oxidation to Chlorine Catalyzed by Silver Ion. *J. Am. Chem. Soc.* **2015**, *137*, 3139–3196.

[5] Moreno-Hernandez, I. A.; Brunschwig, B. S.; Lewis, N. S.; Crystalline nickel, cobalt, and manganese antimonates as electrocatalysts for the chlorine evolution reaction. *Energy Environ. Sci.* **2019**, *12*, 1241–1248.

[6] Abe, H.; Murakami, A.; Tsunekawa, S.; Okada, T.; Wakabayashi, T.; Yoshida, M.; Nakayama, M. Selective Catalyst for Oxygen Evolution in Neutral Brine Electrolysis: An Oxygen-Deficient Manganese Oxide Film. *ACS Catal.* **2021**, *11*, 6390–6397.

[7] Liang, S.; Xu, K.; Zeng, C.-C.; Tian, H.-Y.; Sun, B.-G. Recent Advances in the Electrochemical α-C–H Bond Functionalization of Carbonyl Compounds. *Adv. Synth. Catal.* **2018**, *360*, 4266–4292.

[8] Fan, W.; Verrier, C.; Queneau, Y.; Popowycz, F. 5-Hydroxymethylfurfural (HMF) in Organic Synthesis: A Review of its Recent Applications Towards Fine Chemicals. *Curr. Org. Synth.* **2019**, *16*, 583– 614.

[9] Tuck, C. O.; Perez, E.; Horvath, I. T.; Sheldon, R. A.; Poliakoff, M. Valorization of Biomass: Deriving More Value from Waste Science **2012**, 337, 695– 699.

[10] Taitt, B. J.; Nam, D.-H.; Choi, K.-S. A Comparative Study of Nickel, Cobalt, and Iron Oxyhydroxide Anodes for the Electrochemical Oxidation of 5-Hydroxymethylfurfural to 2,5-Furandicarboxylic Acid. *ACS Catal.* **2019**, *9*, 660–670.

[11] Khatun, S.; Hirani, H.; Roy, P. Seawater electrocatalysis: activity and selectivity. *J. Mater. Chem. A* **2021**, *9*, 74–86.

[12] Nakayama, M.; Kanaya, T.; Lee, J.-W.; Popov, B. N. Electrochemical synthesis of birnessite-type layered manganese oxides for rechargeable lithium batteries. *J. Power Sources* **2008**, *179*, 361–366.

[13] Beyreuther, E.; Grafström, S.; Eng, L. M.; Thiele, C.; Dörr, K. XPS Investigation of Mn Valence in Lanthanum Manganite Thin Films under Variation of Oxygen Content. Phys. Rev. B **2006**, 73, 155425.

[14] Hao, X.; Gourdon, O.; Liddle, B. J. Bartlett, B. M. Improved Electrode Kinetics in Lithium Manganospinel Nanoparticles Synthesized by Hydrothermal Methods: Identifying and Eliminating Oxygen Vacancies. *J. Mater. Chem.* **2012**, *22*, 1578–1591.

[15] Jiang, J.; Kucernak, A. Electrochemical supercapacitor material based on manganese oxide: preparation and characterization. *Electrochim. Acta* **2002**, *47*, 2381–2386.

[16] Scheitenberger, P.; Euchner, H.; Lindén, M. The hidden impact of structural water – how interlayer water largely controls the Raman spectroscopic response of birnessite-type manganese oxide. *J. Mater. Chem. A* **2021**, *9*, 18466–18476.

[17] Shen, M.; Ding, T.; Hartman, S. T.; Wang, F.; Krucylak, C.; Wang, Z.; Tan, C.; Yin, B.; Mishra, R.; Lew, M. D.; Sadtler, B. Nanoscale Colocalization of Fluorogenic Probes Reveals the Role of Oxygen Vacancies in the Photocatalytic Activity of Tungsten Oxide Nanowires. *ACS Catal*. **2020**, *10*, 2088–2099.

[18] Yu, X.; Song, Y.; Tang, A. Tailoring manganese coordination environment for a highly reversible zinc-manganese flow battery. *J. Power Sources* **2021**, *507*, 230295.

Chapter 5
Summary and Outlook

5.1. Summary of Presented Work

Several informative discoveries were made during the development of the chapters described in this thesis. While all sections were designed with selective (bio-derived) alcohol oxidation as the target, key processes and phenomena were revealed broadening the impact of these findings to more general themes in catalysis science. We expand the known compatibility of nitrate-mediated alcohol oxidation platforms, first with visible light absorbing bismuth vanadate ($BiVO_4$) photoelectrodes (Chapter 2) and then on platinum electrodes (Chapter 3) under strict electrochemical control to corroborate the findings in Chapter 2 and detail a general behavior of nitrate in acetonitrile. To our surprise, the overpotential for nitrate oxidation on $BiVO_4$ was sensitive to the presence and amount of benzyl alcohol substrate in solution, shifting by 200 mV for each 10-fold increase in alcohol concentration. This shift was sensitive to the steric environment about the alpha carbon present with a negligible influence due to electronic induction (Hammett studies). On Pt, no resolvable shift was observed for nitrate anion oxidation with alcohol present, pointing toward a unique interaction between the $BiVO_4$ surface and nitrate during nitrate anion oxidation. Nevertheless, nitrate oxidation in all cases increased the rate of benzaldehyde formation in solution.

Chapter 3 concludes with a holistic description of nitrate's behavior in acetonitrile—including a previously unknown side reaction with the solvent—offering new insight for catalyst design. With data supporting a noninnocence of reduced oxygen species responsible for regenerating nitrate anion (only when closely oriented during *photochemical* processes), a case is presented for a synergistic relationship between light-driven redox half reactions beyond thermodynamic activation. The scheme gives scientists a new consideration when developing photoredox catalysis—do the concerted processes influence each other, and if so, to what extent? Answering these questions increases the relevant descriptors when choosing desired redox half reactions.

In Chapter 4, we move to an aqueous system to encourage HER, since undesired ORR dominates in acetonitrile. There, we reconsider the impact of the supporting electrolyte, and develop a sustainability case for transitioning exploration into brine systems. By shifting to brine, we enable catalytic alcohol oxidation to occur in tandem with fuel-forming hydrogen evolution. Manganese oxide films were explored for their alcohol oxidation reactivity based on a previous report detailing glycerol oxidation in chloride-free (acidic) aqueous environments.[1] Based on a separate study detailing the deactivation of electrochemical chloride oxidation on Na_xMnO_2 promoted by thermally induced oxygen vacancy formation,[2] we sought to explore how surface oxygen vacancies influence alcohol oxidation rates on manganese oxide films in brine electrolytes. Crystalline birnessite Na_xMnO_2 were prepared via electrodeposition from manganese sulfate solutions with sodium cations present, and amorphous MnO_x from acid solutions with no metal cations. Annealing Na_xMnO_2 films led to a decrease in Mn AOS (as expected) that was not observed for MnO_x films. For all electrodes except unannealed Na_xMnO_2, 5-HMF in solution leads to a much higher current response during linear sweep voltammetry relative to the alcohol-free brine electrolyte. At present, a feature linked to oxygen vacancy presence (531 eV) in the O 1 s XPS seems to be required to see films respond electrochemically to 5-HMF in brine. Annealed MnO_x (displaying the highest current in voltammetry) could sustain > 1 mA cm^{-2} at 1.65 V vs RHE only with 5-HMF in solution. Through a series of control reactions, we've uncovered a chemical interaction that occurs spontaneously between MnO_x films and solution phase 5-HMF. Surprisingly, the 1.65 V vs RHE applied during CPC acts to shut down the deleterious chemical process, mitigating Mn dissolution.

5.2. Recommended Future Directions

5.2.1. Understanding the Role of Catalyst Surface in Redox Mediated Processes

Despite the broad impacts offered by the general depiction of nitrate behavior in acetonitrile (Chapter 3), the surface-dependent nitrate onset potential shift—with alcohol present—remains unexplained. Rather than serve as an indistinguishable electron sink during electrolysis, the energetic landscape of a catalyst surface is known to depend on several factors, including crystalline phase,[3] available crystalline planes, amorphous character,[4] orbital/band symmetries,[5] and site-specific behavior—as discussed in Chapter 1.4.2.—that all contribute to reactivities during catalysis. The influence of benzyl alcohol on the bismuth vanadate surface is unknown but could facilitate nitrate anion oxidation in several ways; (1) adsorbed alcohol substrate could

influence the adsorption/desorption energies of nitrate anion/nitrate radical during nitrate oxidation;[6] (2). benzyl alcohol and nitrate form a (surface bound) charge transfer complex with a unique redox potential, captured as a shift in nitrate's redox potential. The second phenomenon has been observed recently with a $TEMPO^+/N_3^-$ system, where electrochemical TEMPO radical oxidation to $TEMPO^+$ became easier with azide (N_3^-) in solution;[7] in their system, the charge transfer was a long-lived solution species. *In-operando* spectroscopic methods could identify (transient) changes in nitrate's structure during catalysis that reveal important factors in this cooperative relationship.

5.2.2. Photoelectrode–Electrocatalyst Interfacing for Light Driven Biomass Valorization

Electrocatalyst development for commodity- and fuel-forming reactions is a necessary strategy to break dependence on fossil fuels. Using renewable electricity generated from solar energy conversion to power electrolysis cells represents the most market ready approach to begin the shift from petroleum reliance.[8,9] Eventually, the maturation from the 2-step integrated photovoltaic–electrocatalyst scheme to a single material performing light absorption and redox catalysis is predicted, yet to achieve this vision, complex considerations for all the requisite physical and chemical properties are necessary. Fixing electrocatalysts to light-absorbing semiconductor photoelectrodes has drastically improved rates of PEC water oxidation,[10] and has even been shown to ameliorate cocatalyst deactivation mechanism by introducing a facilitation layer.[11] Based on the emerging activity of MnO_2 in aqueous systems, the unknown cooperativity with photoelectrodes makes MnO_x a high interest target; interfacing bismuth vanadate with MnO_2 layers has potential to offset costs utilizing nonnoble metal oxide catalysts in both layers; importantly sustainability is addressed in a significant way by using biorenewable reactants for sustainable fuel/chemical commodity preparation in the world's most abundant electrolyte.

References

[1] Li, W.; Wei, X.; Han, S.; Chen, L.; Shi, J. MnO_2 Electrocatalyst Coordinating Alcohol Oxidation for Ultra-Durable Hydrogen and Chemical Productions in Acidic Solutions. *Angew. Chem., Int. Ed.* **2021**, *60*, 21464–21472.

[2] Abe, H.; Murakami, A.; Tsunekawa, S.; Okada, T.; Wakabayashi, T.; Yoshida, M.; Nakayama, M. Selective Catalyst for Oxygen Evolution in Neutral Brine Electrolysis: An Oxygen-Deficient Manganese Oxide Film. *ACS Catal.* **2021**, *11*, 6390–6397.

[3] Zhao, K.; Tang, H.; Qiao, B.; Li, L.; Wang, J. High Activity of Au/γ-Fe2O3 for CO Oxidation: Effect of Support Crystal Phase in Catalyst Design. *ACS Catal.* **2015**, *5*, 3528–3539.

[4] Taitt, B. J.; Nam, D.-H.; Choi, K.-S. A Comparative Study of Nickel, Cobalt, and Iron Oxyhydroxide Anodes for the Electrochemical Oxidation of 5-Hydroxymethylfurfural to 2,5-Furandicarboxylic Acid. *ACS Catal.* **2019**, *9*, 660–670.

[5] Zhao, Z.-J.; Liu, S.; Zha, S.; Cheng, D.; Studt, F.; Henkelman, G.; Gong, J. *Nat. Rev. Mater.* **2019**, *4*, 792–804.

[6] Chen, X.; Zhong, X.; Yuan, B.; Li, S.; Gu, Y.; Zhang, Q.; Zhuang, G.; Li, X.; Deng, S.; Wang, J.-g. defect engineering of nickel hydroxide nanosheets by Ostwald ripening for enhanced selective electrocatalytic alcohol oxidation. *Green Chem.* **2019**, *21*, 578–588.

[7] Siu, J. C.; Sauer, G. S.; Saha, A.; Macey, R. L.; Fu, N.; Chauviré, T.; Lancaster, K. M.; Lin, S. Electrochemical Azidooxygenation of Alkenes Mediated by a TEMPO–N_3 Charge-Transfer Complex. *J. Am. Chem. Soc*. **2018**, *140*, 12511–12520.

[8] Ardo, S.; Rivas, D. F.; Modestino, M. A.; Greiving, V. S.; Abdi, F. F.; Llado, E. A.; Artero, V.; Ayers, K.; Battaglia, C.; Becker, J. P.; Bederak, D.; Berger, A.; Buda, F.; Chinello, E.; Dam, B.; Di Palma, V.; Edvinsson, T.; Fujii, K.; Gardeniers, H.; Geerlings, H.; Hashemi, S. M. H.; Haussener, S.; Houle, F.; Huskens, J.; James, B. D.; Konrad, K.; Kudo, A.; Kunturu, P. P.; Lohse, D.; Mei, B.; Miller, E. L.; Moore, G. F.; Muller, J.; Orchard, K. L.; Rosser, T. E.; Saadi, F. H.; Schüttauf, J. W.; Seger, B.; Sheehan, S. W.; Smith, W. A.; Spurgeon, J.; Tang, M. H.; van de Krol, R.; Vesborg, P. C. K.; Westerik, P. Pathways to Electrochemical Solar-Hydrogen Technologies. *Energy Environ. Sci.* **2018**, *11*, 2768–2783.

[9] Gong, J.; English, N. J.; Pant, D.; Patzke, G. R.; Protti, S.; Zhang, T. Power-to-X: Lighting the Path to a Net-Zero-Emission Future. *ACS Sustainable Chem. Eng.* **2021**, *9*, 7179–7181.

[10] Seabold, J. A.; Choi, K.-S. Efficient and Stable Photo-Oxidation of Water by a Bismuth Vanadate Photoanode Coupled with an Iron Oxyhydroxide Oxygen Evolution Catalyst. *J. Am. Chem. Soc*. **2012**, *134*, 2186–2192.

[11] Chadderdon, D. J.; Wu, L.-P.; McGraw, Z. A.; Panthani, M. Heterostructured Bismuth Vanadate/Cobalt Phosphate Photoelectrodes Promote TEMPO-Mediated Oxidation of 5-Hydroxymethylfurfural. *ChemElectroChem* **2019**, *6*, 3387–3392.

Appendix A

Supporting Information for Chapter 2

F(R) is the absorption coefficient equivalent—derived by Kubelka-Munk—for optically opaque films. R_∞ is the absolute reflectance measured by the integration sphere of the Cary 5000 UVvis-NIR spectrophotometer; the transformation of absolute reflectance to absorption is given below:

$$F(R)_{\text{Kubelka-Munk}} = \frac{(1 - R_\infty)^2}{2R_\infty}$$

In the Tauc plot below (Figure A.1, right), the absorption coefficient ($\alpha \sim F(R)$) multiplied by the photon energy (hν) and raised to the appropriate exponent is standard for accessing material band gap. For indirect bandgaps with allowed transitions, the exponent is 0.5.

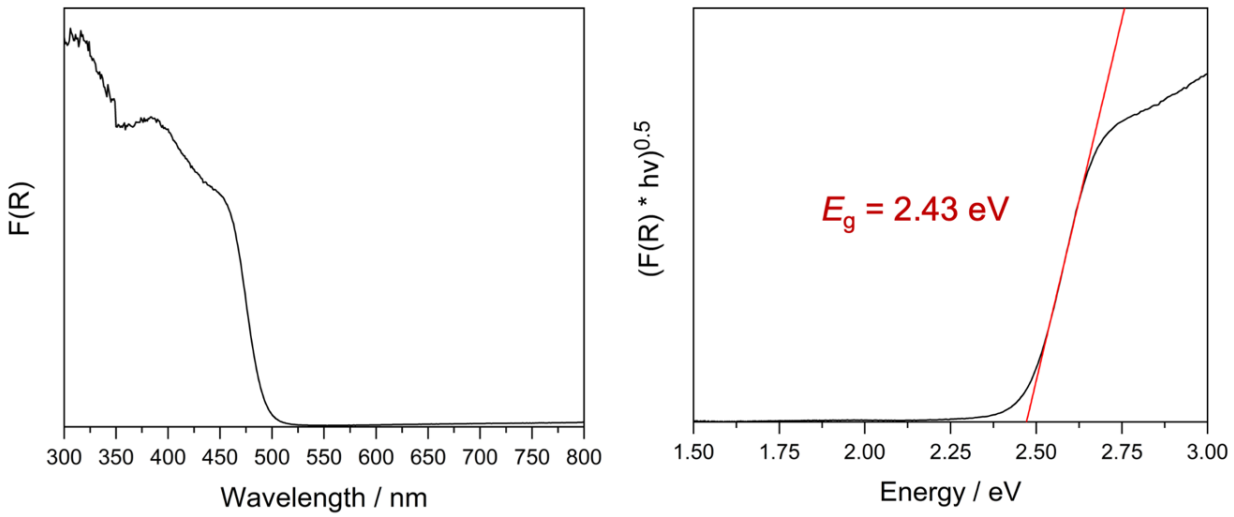

Figure A.1. F(R) transformation of diffuse reflectance measurements on as-made $BiVO_4$ films via Kubelka-Munk Theory given by the following equation (left). Tauc analysis treating $BiVO_4$ as an indirect band gap material (right).

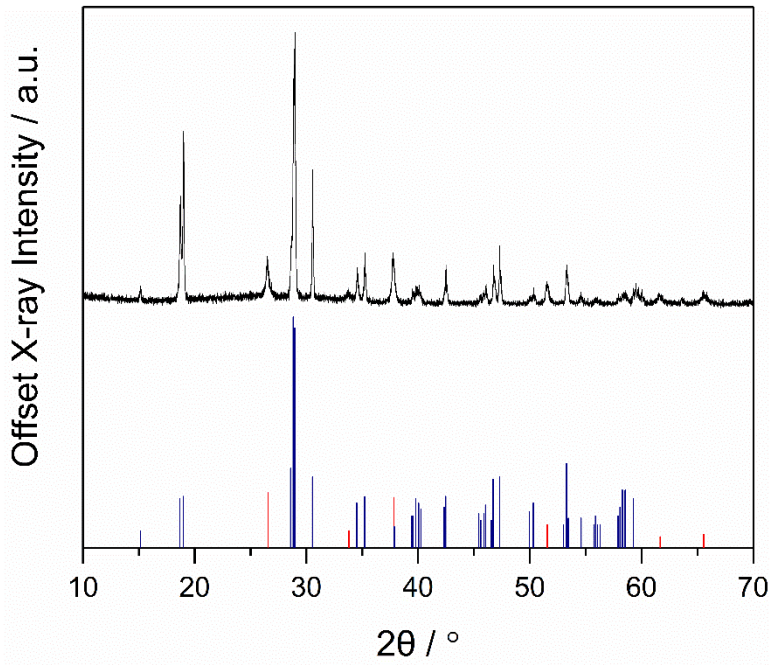

Figure A.2. X-ray diffractogram containing diffraction patterns for as-made $BiVO_4$ films (black pattern, top), fluorine-doped tin oxide glass substrate (red droplines) and Jade database reference pattern (PDF#14-0688) for monoclinic $BiVO_4$ (blue droplines).

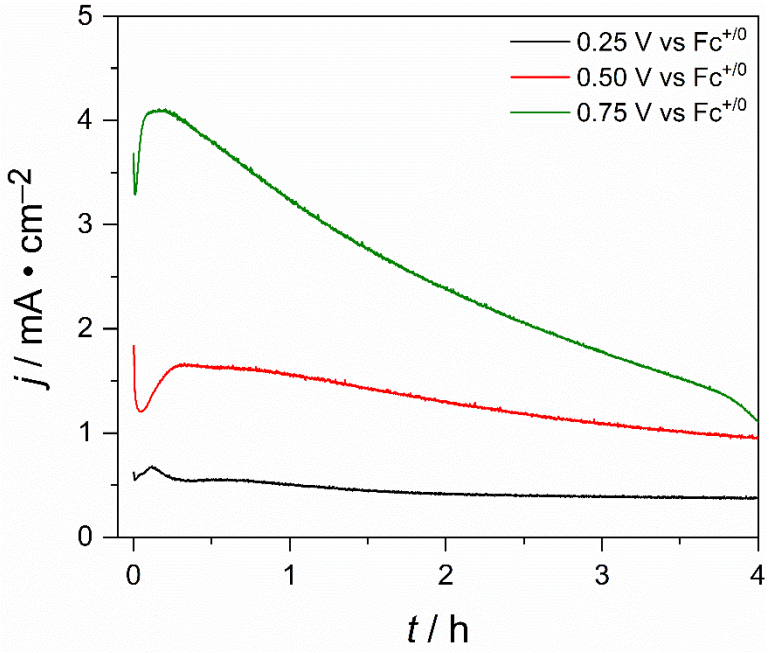

Figure A.3. Current vs time plot during CPC experiments with 250 mM $PhCH_2OH$ in 100 mM Bu_4NPF_6 (MeCN). A constant potential was held on the $BiVO_4$ working electrode while stirring the solution in the presence of 100 mW cm^{-2} Royal Blue LED (λ_{max} = 448 nm).

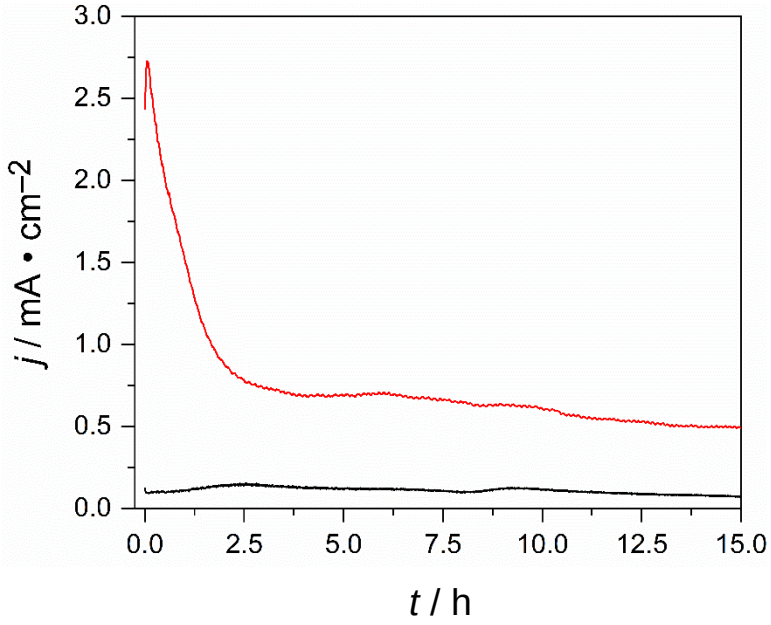

Figure A.4. Current vs time plot during CPC experiments for solution containing 250 mM $PhCH_2OH$ in 100 mM Bu_4NPF_6 (MeCN) with (red trace) and without (black trace) 100 mM Bu_4NNO_3. A constant potential of 0 V vs $Fc^{+/0}$ was held on the $BiVO_4$ working electrode while stirring the solution in the presence of 100 mW cm^{-2} Royal Blue LED (λ_{max} = 448 nm).

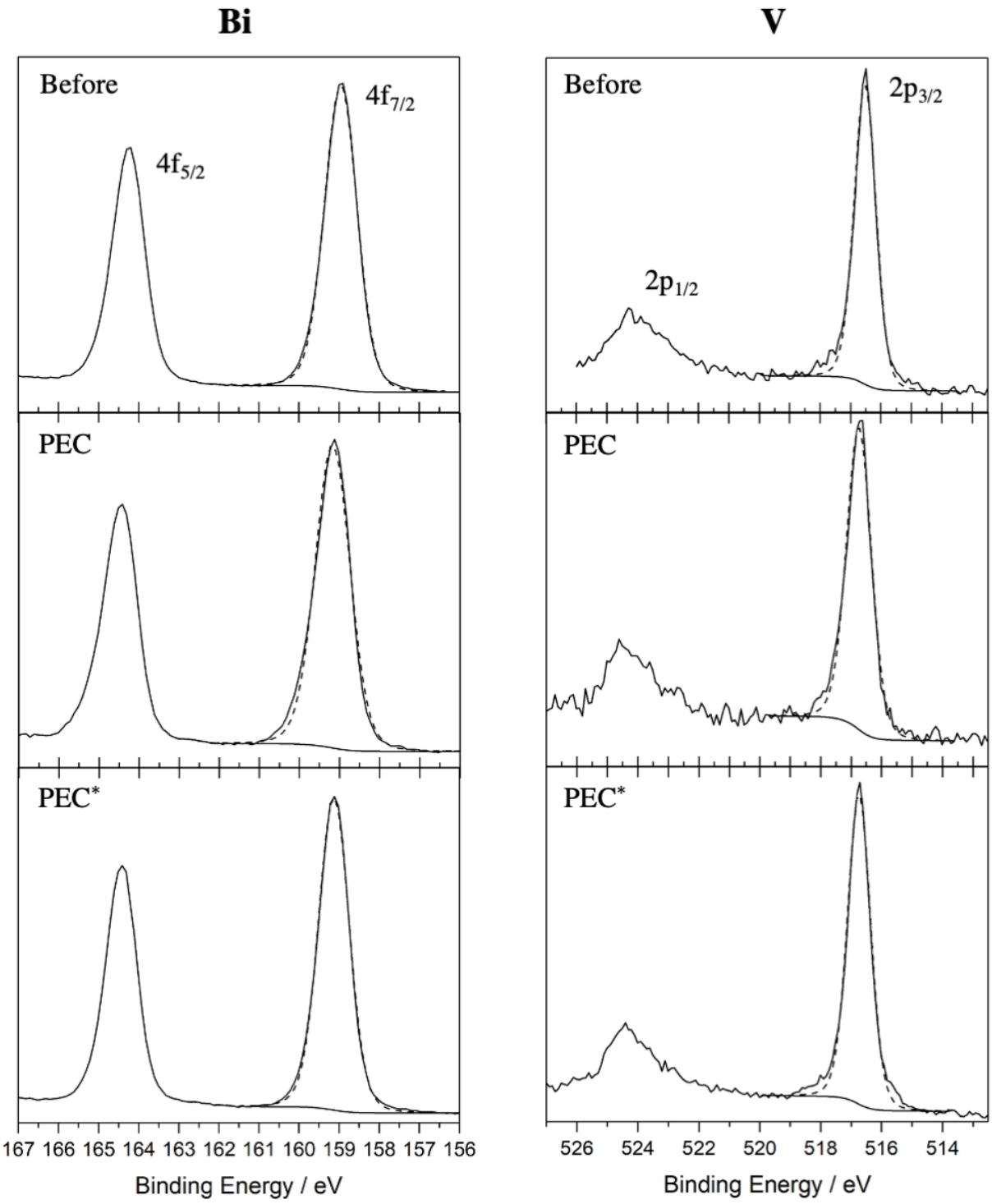

Figure A.5. XPS spectra of the bismuth 4f doublet (left) along with vanadium 2p doublet (right) using as-made $BiVO_4$ (top); after CPC under PEC—**Table 2.1**, entry 3—and PEC*—entry 4—conditions.

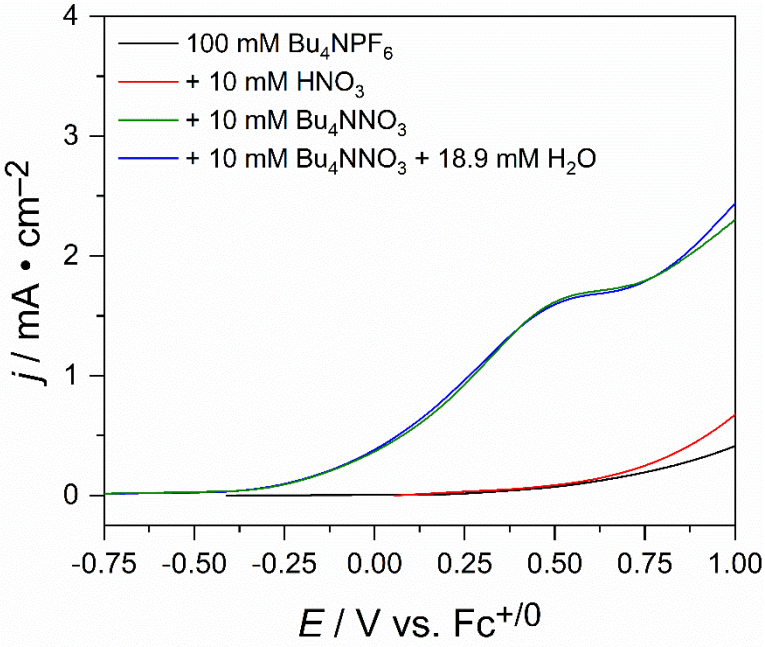

Figure A.6. LSVs in solutions containing 10 mM Bu_4NO_3 or 10 mM HNO_3 (Note: Millipore water was added to Bu_4NO_3 (red trace) to account for the water introduced by adding 65% HNO_3 solution in water). Scan rate: 10 mV s^{-1}, illumination: 100 mW cm^{-2} of 447.5 nm Royal Blue LED illumination in a single-compartment PEC cell with a Pt coil cathode and Ag wire reference electrode (protected by Vycor frit).

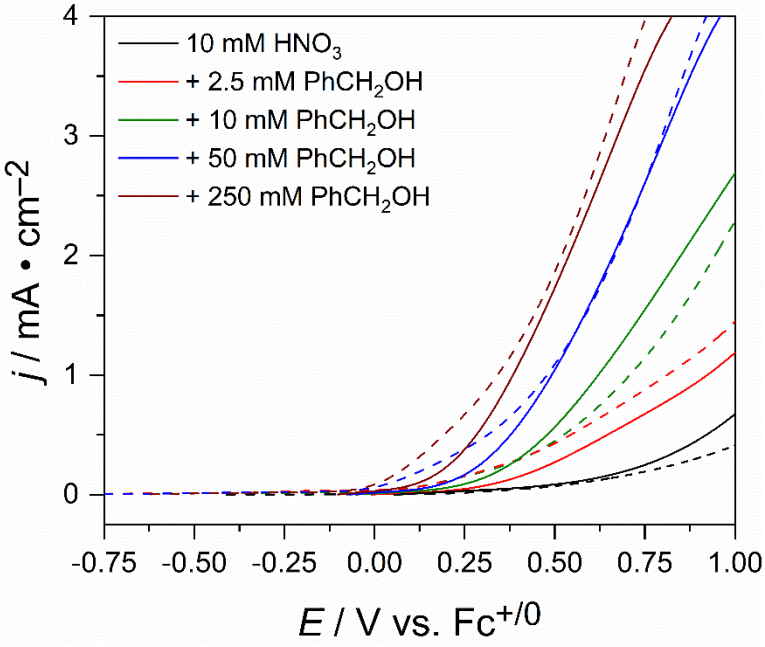

Figure A.7. Solid lines: varying concentrations of benzyl alcohol with 10 mM HNO_3 introduced. Dashed lines: Same concentration of benzyl alcohol without HNO_3 present (Presented in main text Figure 1). Scan rate: 10 mV s^{-1}, illumination: 100 mW cm^{-2} of 447.5 nm Royal Blue LED illumination in a single-compartment PEC cell with a Pt coil cathode and Ag pseudo reference to $Fc^{+/0}$ (protected by Vycor frit).

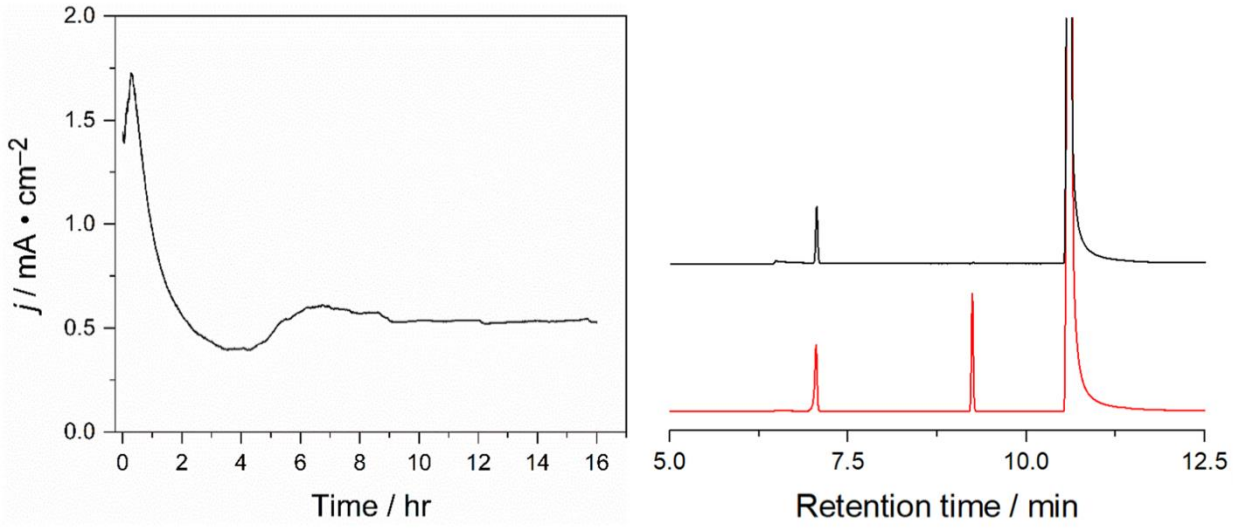

Figure A.8. 16-hour bulk electrolyses on $BiVO_4$ while stirring in 100 mW cm^{-2} 448 nm Royal Blue LED illumination. Solution consisted of 100 mM Bu_4NPF_6 supporting electrolyte with 50 mM Bu_4NNO_3 and 500 mM $PhCH_2OH$ in acetonitrile (left). Representative GC-FID traces used for product analysis and FE determination. The top trace is a before electrolysis and the bottom is after the same solution after CPC for 16 hours at 0 V vs $Fc^{+/0}$ (right).

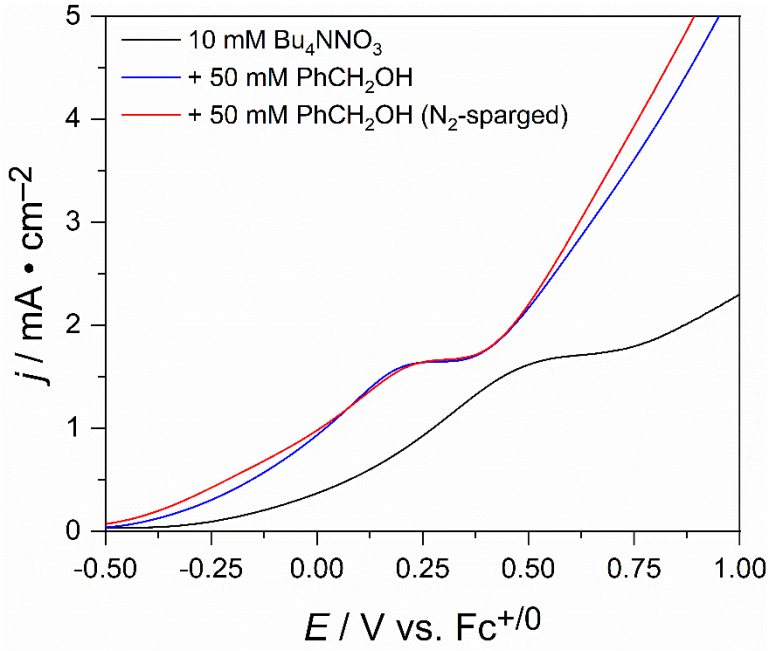

Figure A.9. LSVs on $BiVO_4$ in solutions containing 10 mM Bu_4NNO_3 and 50 mM $PhCH_2OH$. N_2 sparged into solution for 1 hour while sealed and stirring solution (volume ~15 mL) Scan rate: 10 mV s-1, illumination: 100 mW cm^{-2} of 447.5 nm Royal Blue LED illumination in a single compartment PEC cell with a Pt coil cathode and Ag wire reference electrode (protected by Vycor frit).

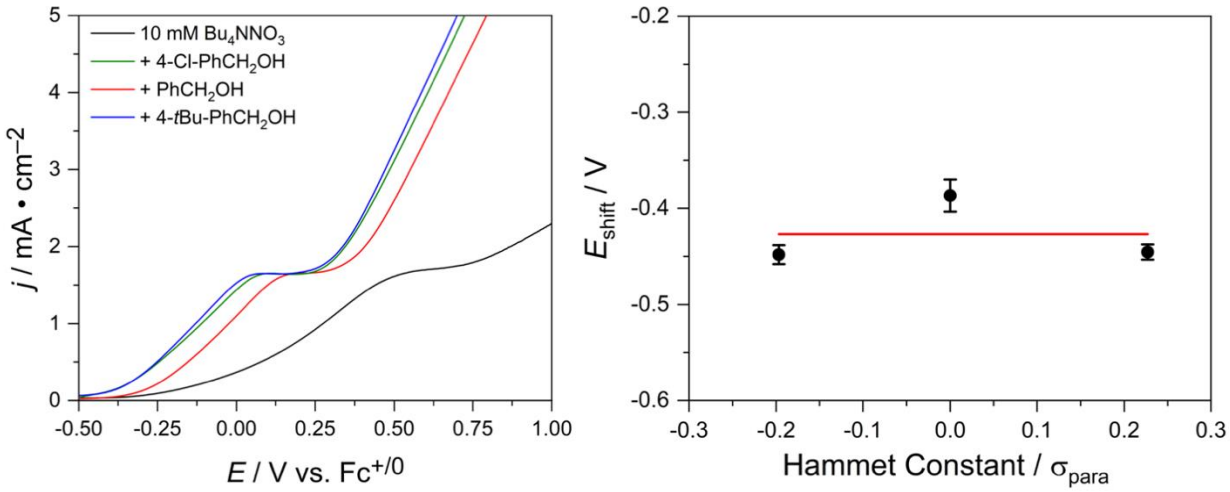

Figure A.10. LSVs on $BiVO_4$ in solutions containing 10 mM Bu_4NNO_3 and 50 mM of a benzyl alcohol derivative as labeled (left). Scan rate: 10 mV s^{-1}, illumination: 100 mW cm^{-2} of 447.5 nm Royal Blue LED illumination in a single-compartment PEC cell with a Pt coil cathode and Ag wire reference electrode (protected by Vycor frit). Average E_{shift}—potential at middle of plateau— plotted as a function of para-substituted sigma Hammett parameters for 4-tBu-benzyl alcohol (σ_{para} = –0.20), 4-Cl-benzyl alcohol (σ_{para} = +0.23) relative to benzyl alcohol (σ_{para} = 0) (right). Sigma values obtained from: McDaniel, D. H.; Brown, H. C. An Extended Table of Hammett Substituent Constants Based on the Ionization of Substituted Benzoic Acids. *J. Org. Chem*. **1958**, *23*, 420–427.

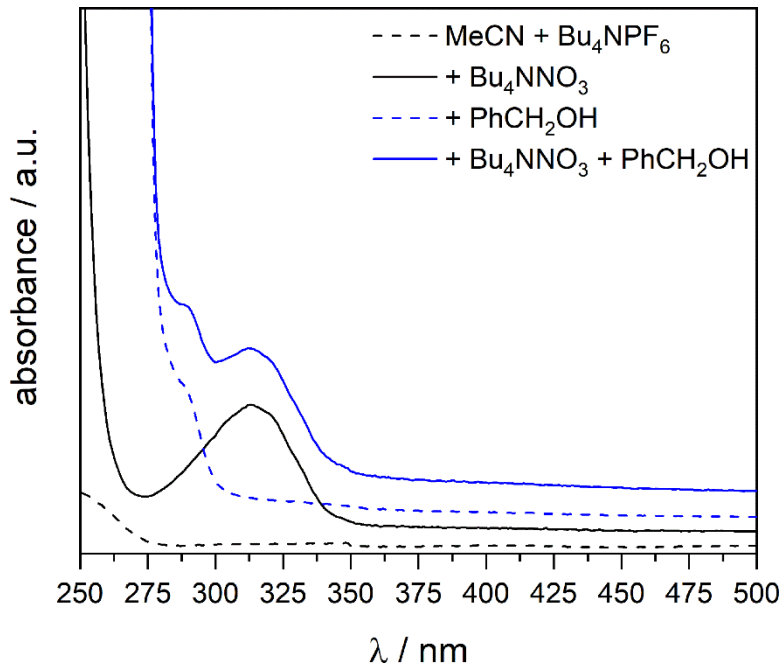

Figure A.11. UV-vis spectra of solutions corresponding to the LSVs displayed in **Figure 2.4b** (by color).

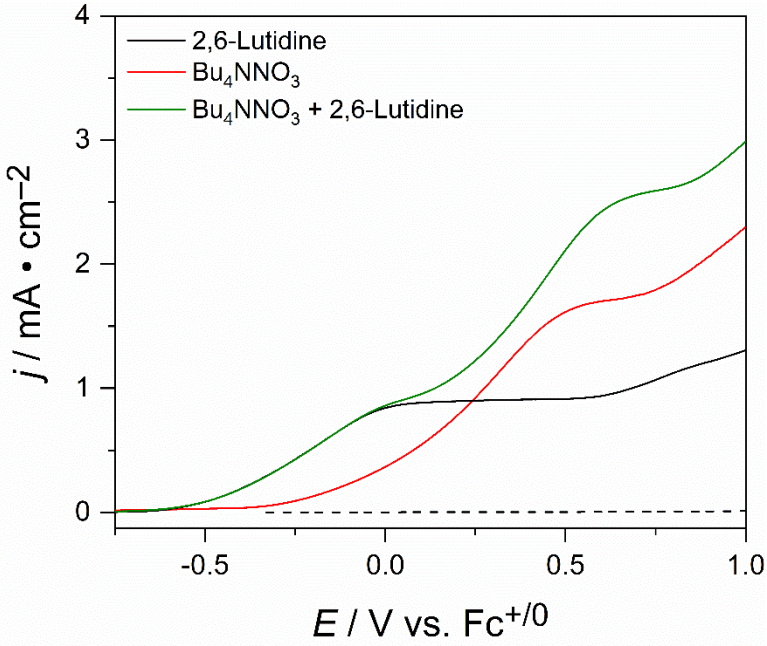

Figure A.12. LSVs of 10 mM Bu_4NNO_3 and 5 mM 2,6-Lutidine independently and together in solution. Dashed line indicates no light used during scan. Scan rate of 10 mV s^{-1} along with 100mWcm^{-2} 447.5 nm LED light (solid lines).

Appendix B

Supporting Information for Chapter 3

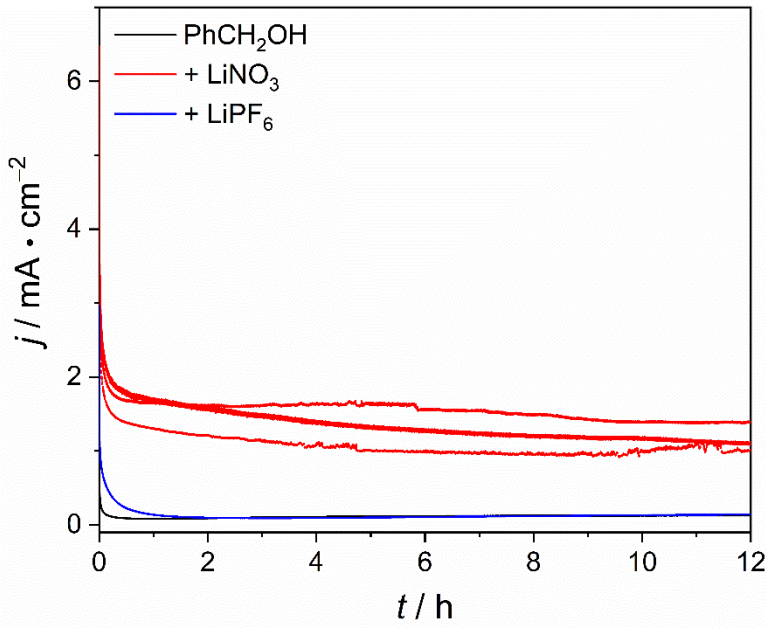

Figure B.1. Multiple CPC trials of indirect benzyl alcohol oxidation at E = 1.68 V vs $Fc^{+/0}$ with MeCN solutions containing 0.1 M Bu_4NPF_6 under the listed conditions, where [$PhCH_2OH$] = 250 mM and [$LiNO_3$] = [$LiPF_6$] = 50 mM.

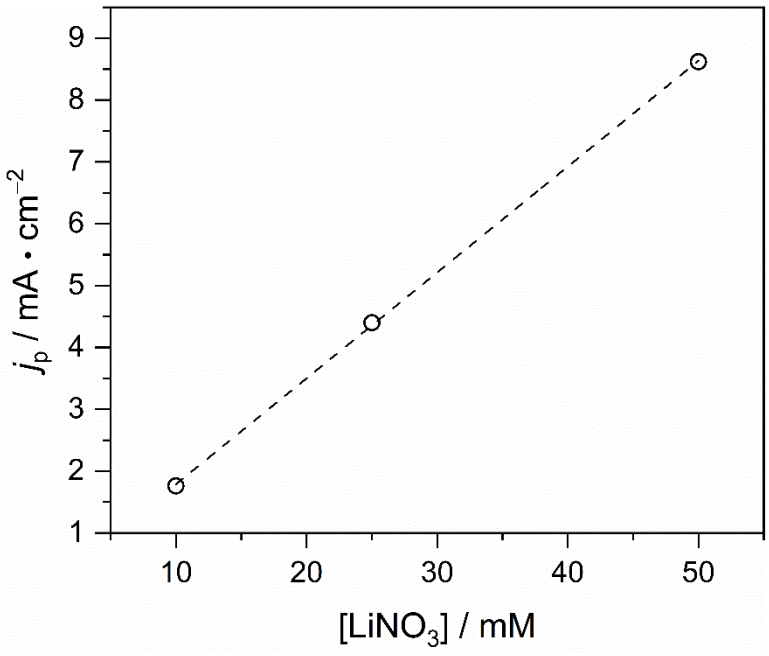

Figure B.2. Plot of peak current density (j_p) vs $LiNO_3$ solution concentration. The voltammetry was performed at 25 mV s^{-1} in an MeCN solution of 250 mM $PhCH_2OH$, 100 mM Bu_4NPF_6 with the listed $LiNO_3$ concentration.

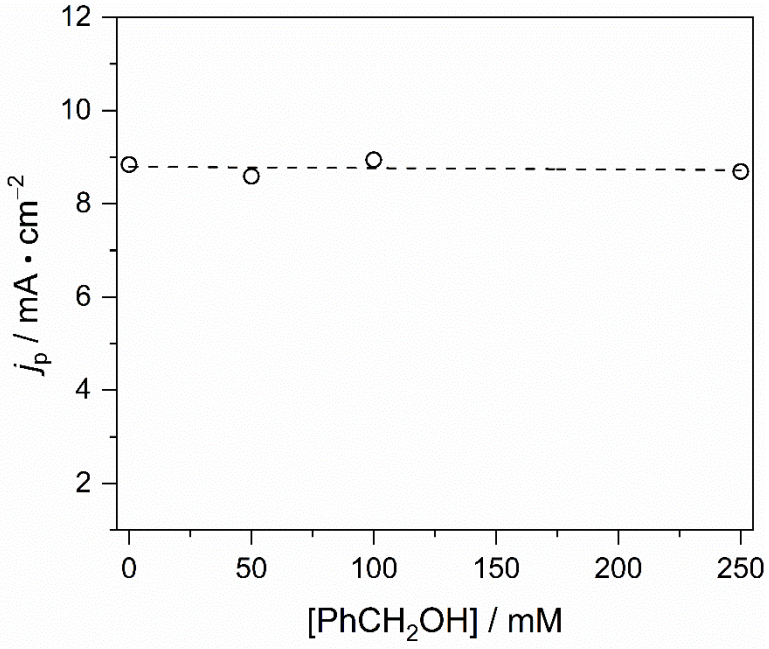

Figure B.3. Plot of peak current density vs $PhCH_2OH$ solution concentration. The voltammetry was performed 25 mV s^{-1} in an MeCN solution of 50 mM $LiNO_3$, 100 mM Bu_4NPF_6 with the listed $PhCH_2OH$ concentration.

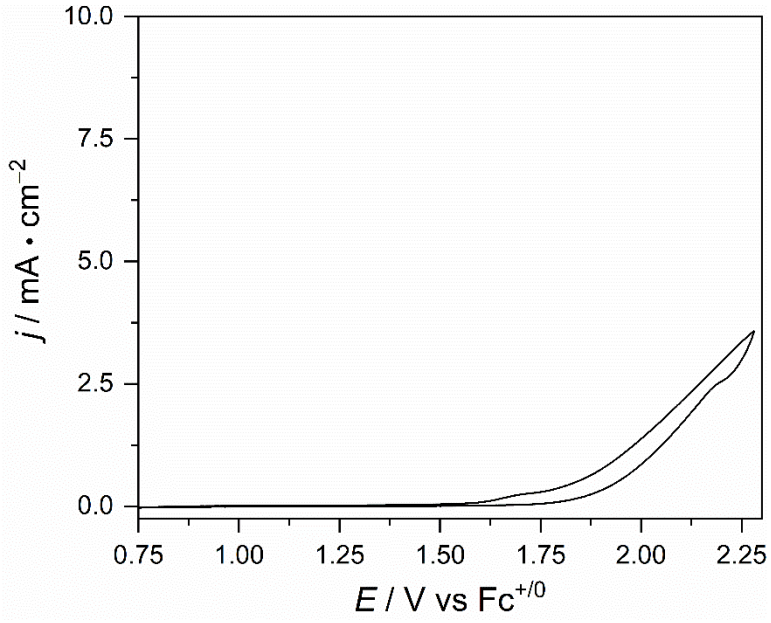

Figure B.4. Voltammograms at 25 mV s^{-1} in 50 mM HNO_3 (MeCN) with 100 mM Bu_4NPF_6.

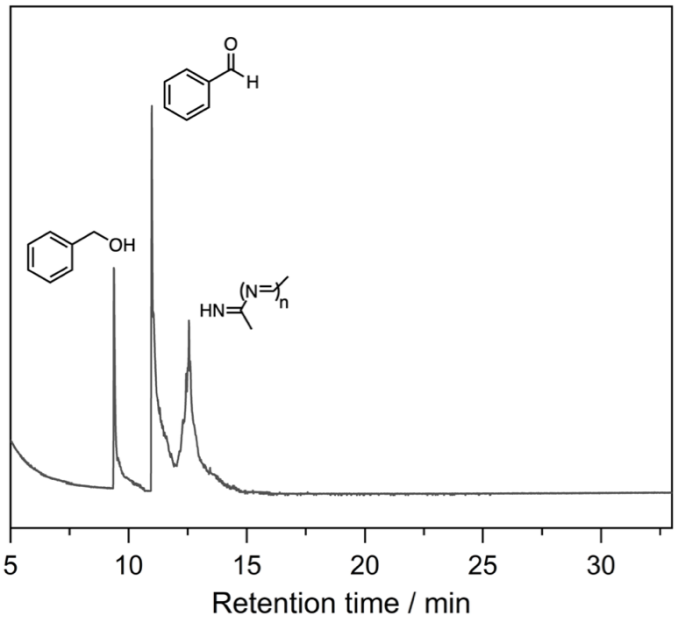

Figure B.5. Gas chromatograms after 1.68 V vs $Fc^{+/0}$ CPC in solutions containing 100 mM Bu_4NPF_6 in MeCN under the listed conditions. In all cases [$LiNO_3$] = [$LiPF_6$] = 50 mM and [$PhCH_2OH$] = 250 mM. The signals at 9.4, 11.0, and 12.6 minutes correspond to benzaldehyde, benzyl alcohol, and a solvent based by-product, respectively.

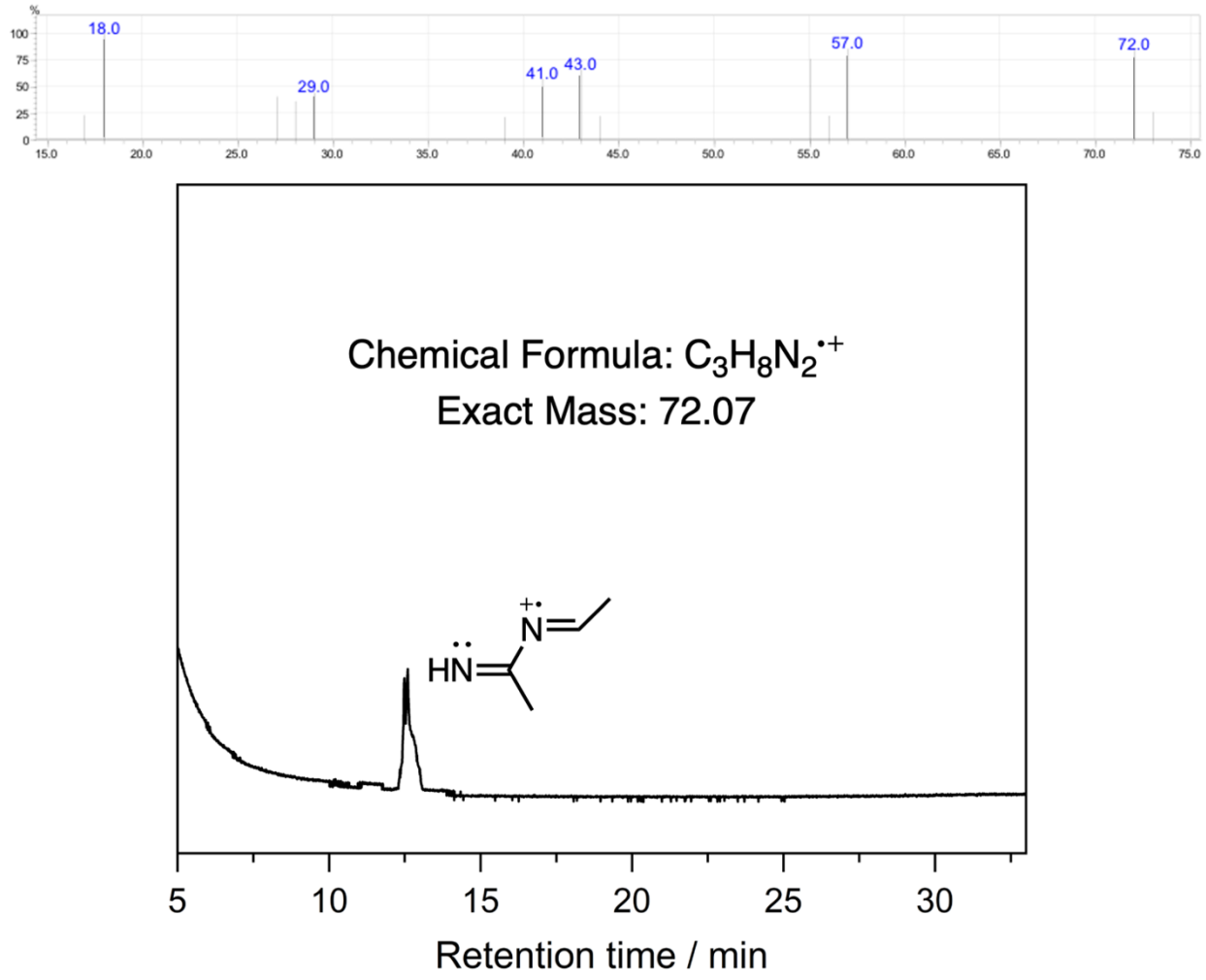

Figure B.6. Gas chromatogram after 1.68 V vs $Fc^{+/0}$ CPC in an MeCN solution of 50 mM $LiNO_3$ and 100 mM Bu_4NPF_6. The mass spectrum of the 12.6-minute peak is shown which is assigned to an acetonitrile product formed from a reaction between nitrate radical and solvent.

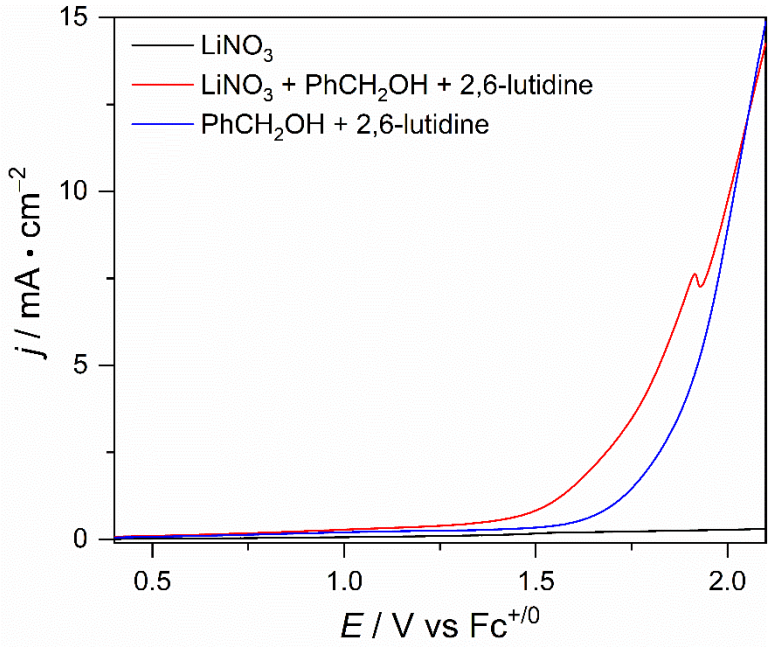

Figure B.7. Linear sweep voltammograms collected at 25 mV s^{-1} in MeCN solutions of 0.5 mM $LiNO_3$ solutions, with 250 mM $PhCH_2OH$ and/or 25 mM 2,6-lutidine as labeled.

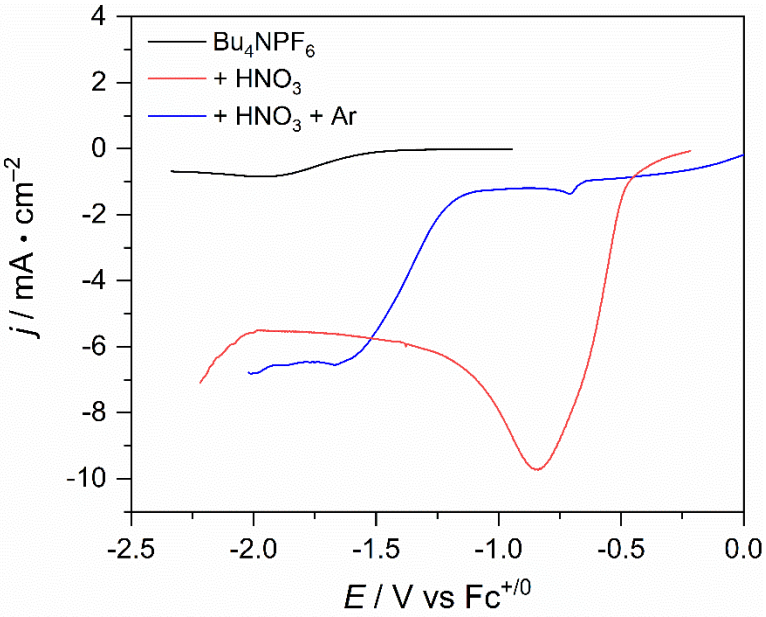

Figure B.8. Linear sweep voltammograms at 25 mV s^{-1} collected in the listed acetonitrile solutions, where [Bu_4NPF_6] = 100 mM, [HNO_3] = 50 mM. The argon experiment was performed using a solution de-gassed via freeze-pump-thaw and analyzed in an argon glovebox. The HNO_3 under argon experiment (blue) found the potential required for hydrogen evolution to be –1.2 V vs $Fc^{+/0}$. The black trace shows oxygen reduction in the absence of protons (i.e., to superoxide radical) that occurs at –1.6 V vs $Fc^{+/0}$, and proton-coupled electron transfer (red trace) reduction of oxygen to water occurs at –0.4 V vs $Fc^{+/0}$. The small feature at -0.7 V vs $Fc^{+/0}$ (blue trace) is residual O_2 remaining after freeze-pump-thaw.

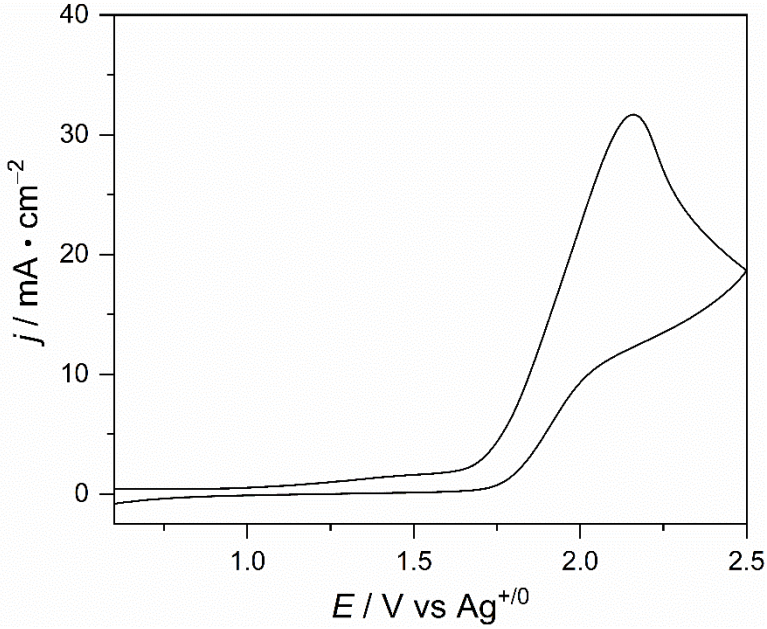

Figure B.9. Voltammetry of 50 mM $LiNO_3$ in CD_3CN solutions containing 100 mM $LiPF_6$ supporting electrolyte acquired on Pt electrodes at 1 V s^{-1}.

Figure B.10. Image of custom built two-compartment CPC cell constructed with an ultra-fine frit (left); a cell (right) utilizing a disposable polypropylene filter paper (shown) with 0.1-micron pore size to separate the working and counter compartments.

Appendix C

Supporting Information for Chapter 4

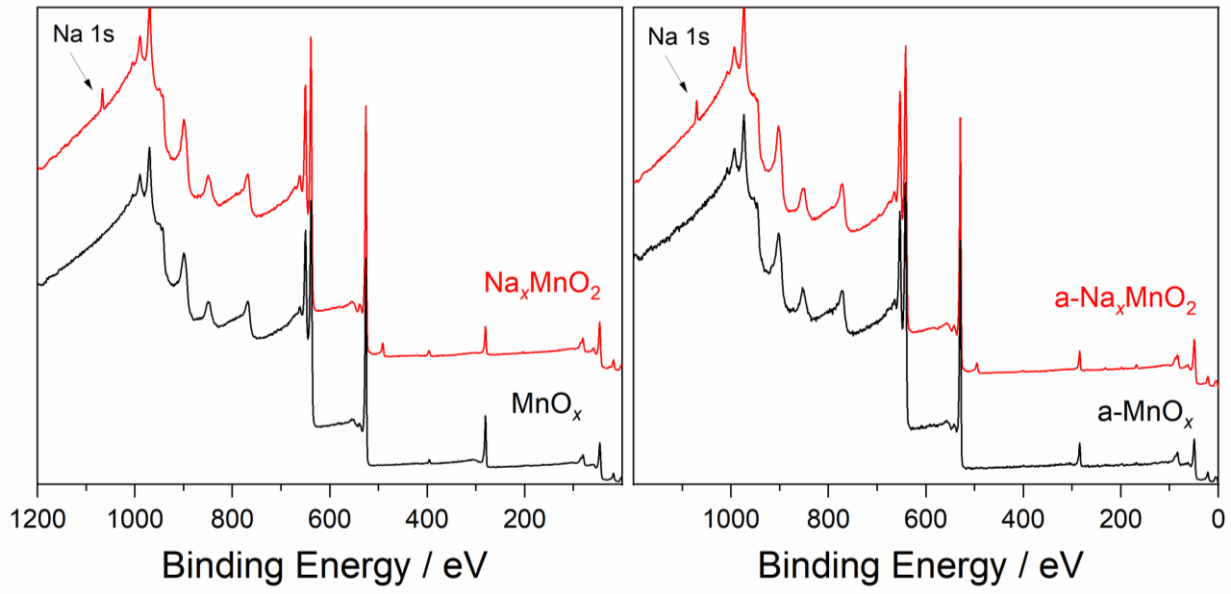

Figure C.1. XPS survey scans of manganese oxide films as electrodeposited and after annealing.

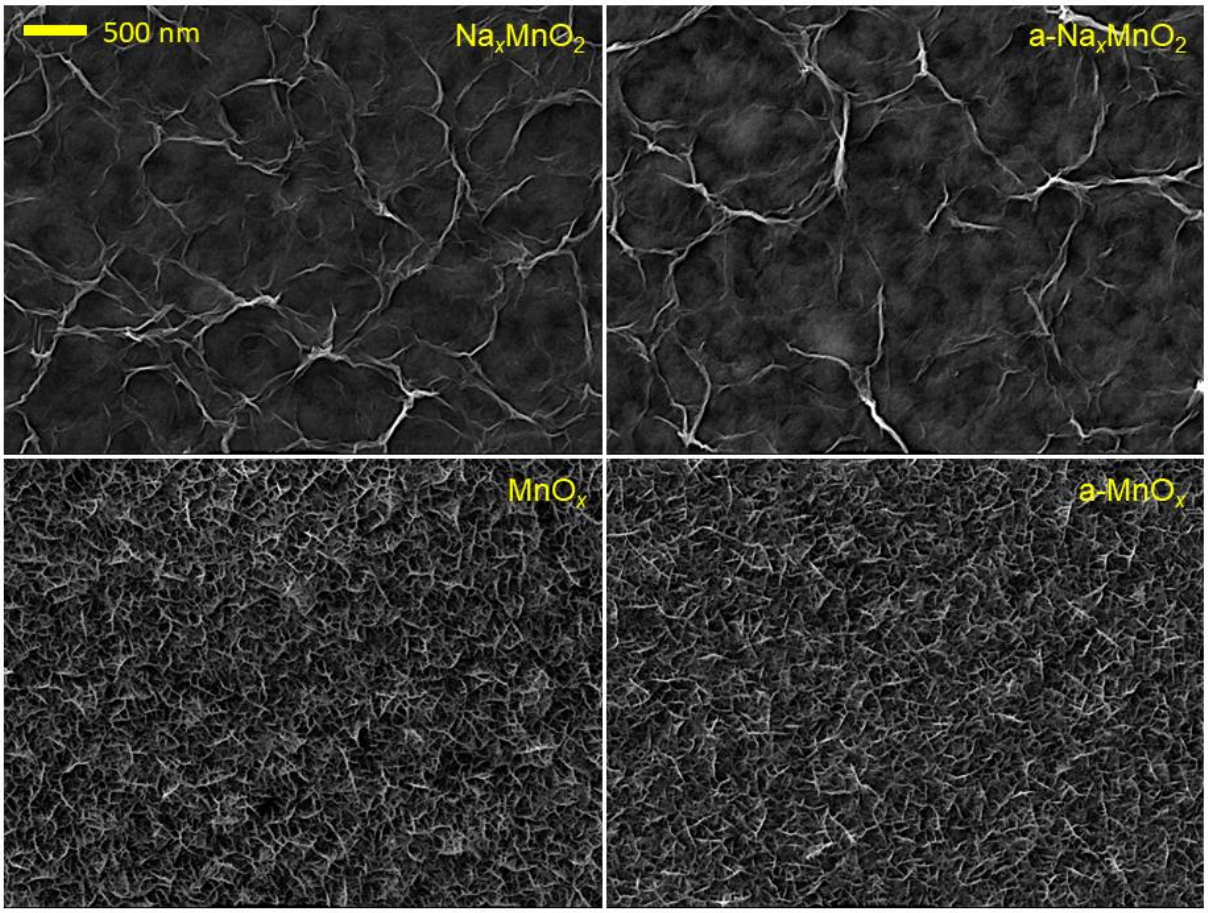

Figure C.2. Top-down scanning electron micrographs of manganese oxide films (as designated) with electrodeposited films on the left and post-annealed films on the right; all images are presented at the same magnification.

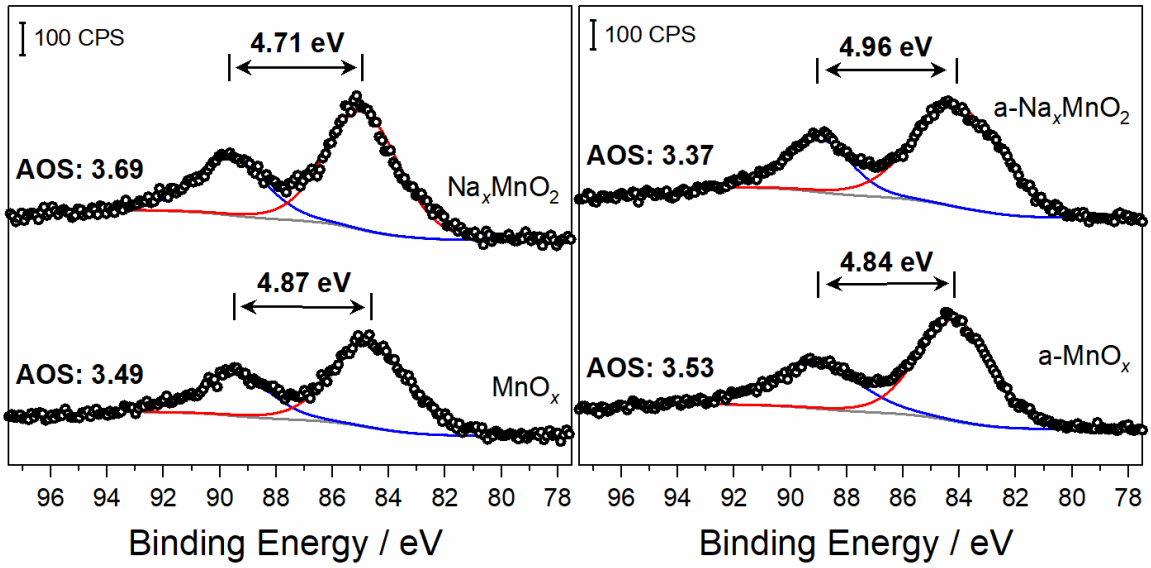

Figure C.3. Mn 3s XPS features for Na_xMnO_2 and MnO_x films as electrodeposited or after annealing.

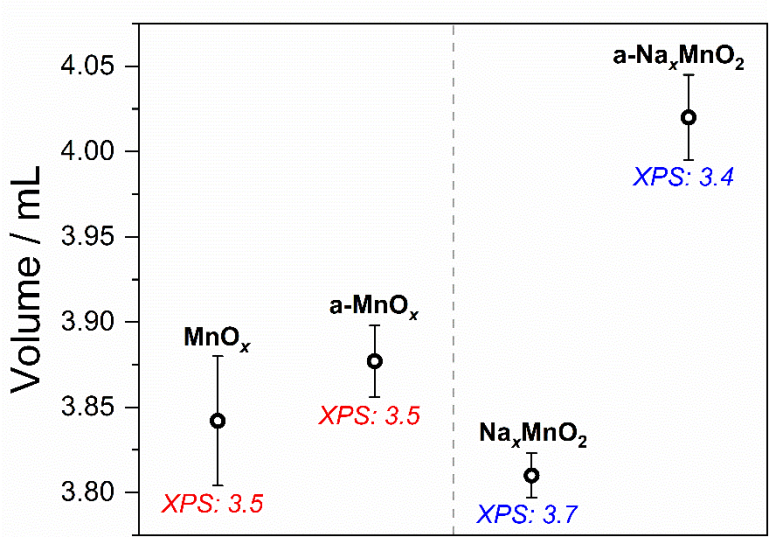

Figure C.4. Titration volume of 1.5 mM $KMnO_4$ required after Mn-film dissolution in 4 mL of 9 mM $FeCl_2$(aq).

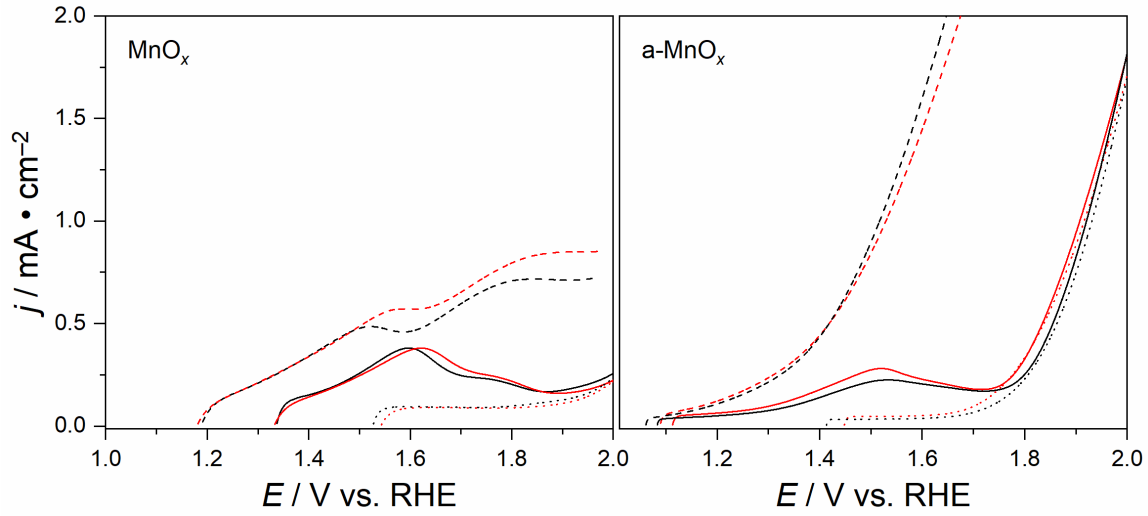

Figure C.5. Sequential linear sweep voltammograms on manganese oxide films from OCP to 1.55 V vs Ag/AgCl at 10 mV s^{-1}. Scans in 600 mM NaCl(aq) (black) were compared to 600 mM $NaNO_3$(aq) (red); solid traces depict the first 5-HMF free scan is base electrolyte, followed by a second scan (dotted) after 5 minutes of stirring in base electrolyte. With 100 mM 5-HMF, a third scan (dashed lines) is shown for both electrolytes.

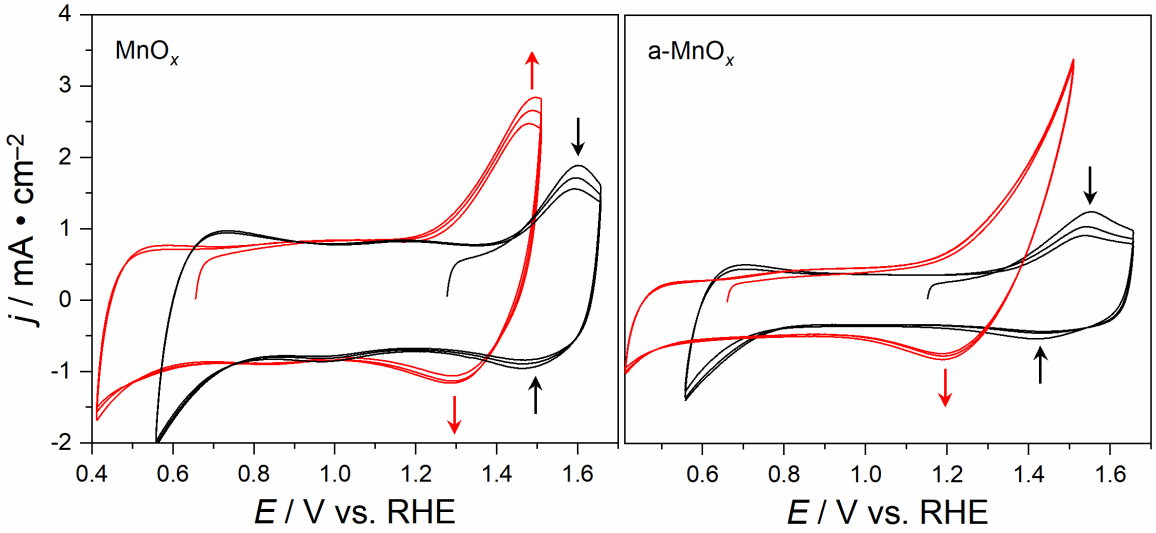

Figure C.6. Cyclic voltammograms on manganese oxide films performed sweeping from OCP to 1.1 V vs Ag/AgCl at 10 mV s^{-1}, then reversing direction to 0 V vs Ag/AgCl and sweeping positive from 0 V again.

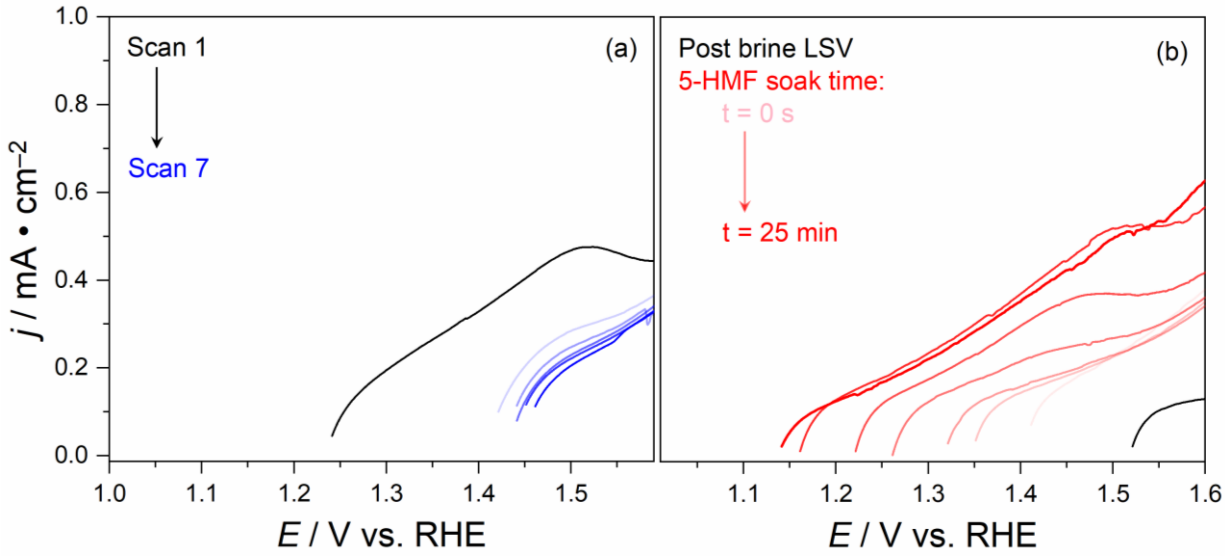

Figure C.7. Sequential LSVs on a single MnO_x film at 10 mV s^{-1} from OCP to 1.2 V vs Ag/AgCl in 600 mM NaCl(aq) and 100 mM 5-HMF(aq) with the first LSV (black) compared to following scans (increasingly darker blue) (a); a preconditioned MnO_x film in 600 mM NaCl(aq) (black) and in 600 mM NaCl(aq) with 100 mM 5-HMF(aq) with varying soak times in the 5-HMF containing brine solution (30 s, 1 min, 2.5 min, 5 min, 10 min, 25 min) (b).

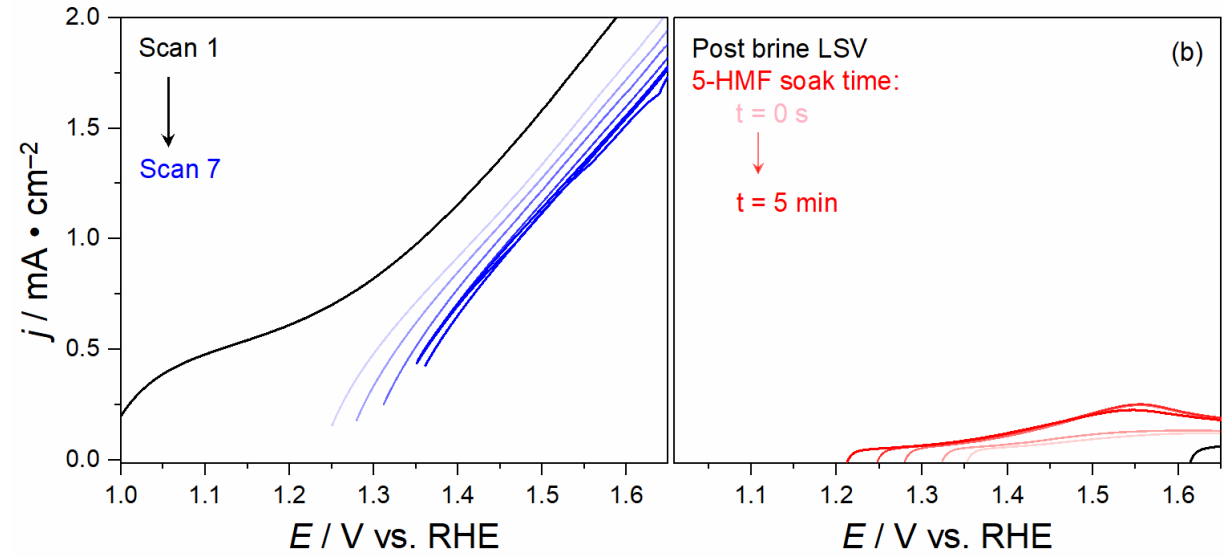

Figure C.8. Sequential LSVs on a single a-MnO_x film at 10 mV s^{-1} from OCP to 1.2 V vs Ag/AgCl in 600 mM NaCl(aq) and 100 mM 5-HMF(aq) with the first LSV (black) compared to following scans (increasingly darker blue) (a); a preconditioned a-MnO_x film in 600 mM NaCl(aq) (black) and in 600 mM NaCl(aq) with 5-HMF(aq) with varying soak times in the 5-HMF containing brine solution (3 s, 10s, 1 min, 2.5 min, 5 min); films were rinsed and LSVs performed in 5-HMF free brine due to high current in solutions with 5-HMF (b).

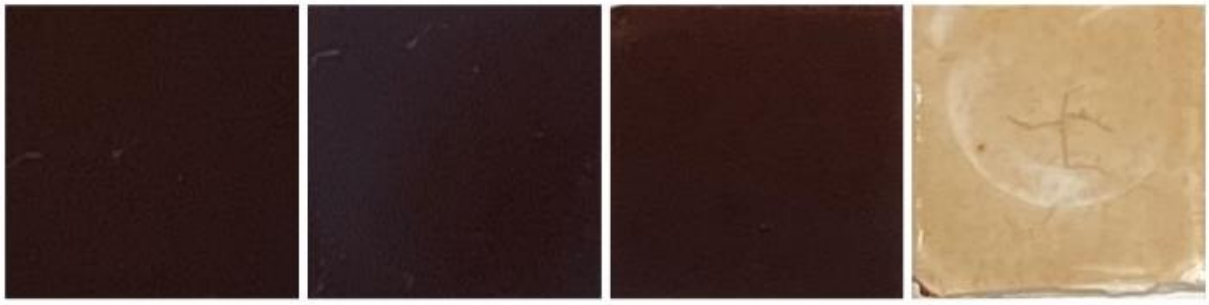

Figure C.9. Top-down optical images of a-MnO_x as made (left); post CPC at 1.65 V vs RHE in brine (middle left); post CPC at 1.65 V vs RHE in brine with 5-HMF (middle right); post bias-free brine with 5-HMF stir control (right).

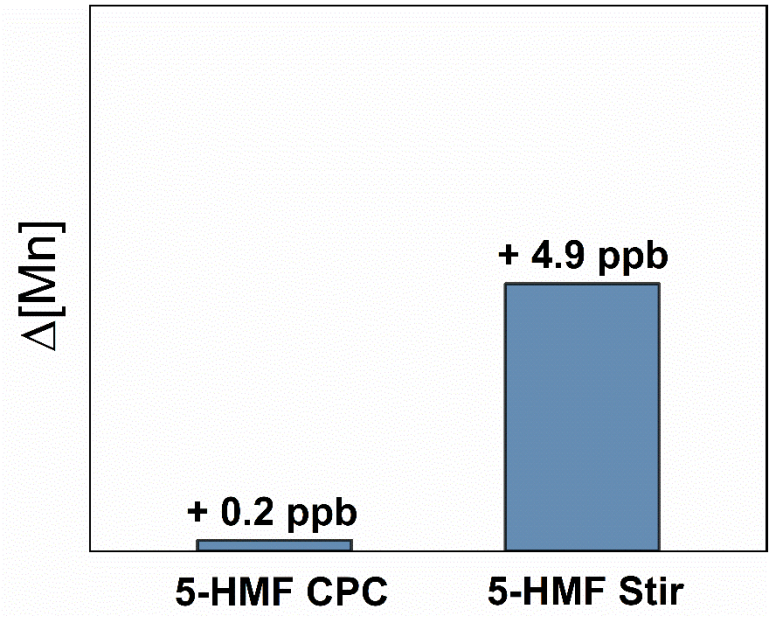

Figure C.10. dissolved manganese content in solution following a-MnO_x exposure to 5-HMF during 1.65 V vs RHE (CPC) or open circuit potential (stir) for 4 hours.